



FEUP FACULDADE DE ENGENHARIA
UNIVERSIDADE DO PORTO

Gastrointestinal Tract Chyme Propulsion in Patients with Gastrointestinal Limitations

**Integrated Master in Mechanical Engineering
Dissertation Thesis**

Author:

Mariana Rocha Carvalho

Supervisor:

Dr. João Pedro Sousa Ferreira

Cosupervisors:

Prof. Dr. Marco Paulo L. Parente

Prof. Dr. Renato Natal Jorge

June 28th, 2021

ABSTRACT

Regular intestinal motility is essential to guarantee complete digestive function. The coordinative action and integrity of the smooth muscle layers in the small intestine's wall are critical for mixing and propelling the luminal content. However, some patients present gastrointestinal limitations which may negatively influence the normal motility of the intestine, by changing the wall's mechanical properties, the muscle's contractile ability, or the motility patterns. As patients with gastrointestinal limitations may likely need medical intervention, establishing a comparison concerning the impaired propulsion can help to ease the evaluation and treatment of future complications.

In this thesis, the propulsive capability of the small intestine during a peristaltic wave was examined along the distal direction of the tract as the mechanical properties of the wall varied. Likewise, the impaired muscle contractile ability of systemic sclerosis patients was compared with the intestinal characteristics of normal patients. Furthermore, the influence of the sores resultant from ulcers was also analyzed.

To this matter, a coordinated activation signal, quantified in the Martins constitutive model (Martins et al. 1998), triggers the peristaltic contractions. The model decouples the strain energy function into an isotropic contribution of the ground-matrix and an active and passive contribution of the fiber-reinforcement. The passive constitutive model parameters were obtained from uniaxial tensile tests in the porcine small intestine along both longitudinal and circumferential directions. The contractile peristaltic wave was defined based on a space and time-dependent variable (activation) written in a USDFLD subroutine, which was linked to a user-defined UMAT for describing the Martins model.

A biomechanical simulation of the chyme's propulsion in the small intestine under a peristaltic contraction was defined in the software ABAQUS. Based on biologically inspired constitutive assumptions, the simulations show decreased force generated by the peristaltic contraction in systemic sclerosis and ulcer patients.

RESUMO

Uma motilidade intestinal regular é essencial para garantir a completa função digestiva. A ação coordenada e a integridade das camadas de músculo liso no intestino são fundamentais para misturar e impulsionar os conteúdos intraluminais. No entanto, alguns pacientes apresentam limitações no sistema gastrointestinal que podem influenciar negativamente a motilidade normal do intestino, através de uma mudança nas propriedades mecânicas da parede, na capacidade contráctil do músculo liso ou nos padrões de motilidade. Como pacientes com limitações gastrointestinais geralmente necessitam de intervenção médica, estabelecer uma comparação relativa à alteração na propulsão pode facilitar a avaliação e tratamento de futuras complicações.

Nesta dissertação, a capacidade de propulsão do intestino delgado durante uma onda peristáltica foi examinada ao longo da direção distal do intestino uma vez que as propriedades mecânicas da parede variam nesta direção. Do mesmo modo, a capacidade contráctil muscular reduzida em pacientes com esclerose múltipla foi comparada com a de intestino de um paciente normal. Além disso, a influência das feridas resultantes de úlceras foi analisada.

Para este efeito, um sinal de ativação, definido no modelo constitutivo Martins (Martins et al. 1998), desencadeia a contração peristáltica. Este modelo dissocia a energia de deformação numa contribuição isotrópica da matriz e na contribuição ativa e passiva do reforço por fibras. Os parâmetros constitutivos que descrevem o comportamento passivo foram obtidos de ensaios de tração no intestino delgado de um porco segundo a direção longitudinal e circunferencial. A onda peristáltica foi definida tendo por base uma variável dependente do espaço e do tempo (ativação) numa sub-rotina USDFLD ligada a uma sub-rotina UMAT que descreve o modelo Martins.

A simulação biomecânica da propulsão do quimo no intestino delgado durante uma contração peristáltica foi definida no software ABAQUS. Com base em pressupostos inspirados na biologia dos tecidos, as simulações demonstraram uma diminuição da força gerada pela contração peristáltica em pacientes com esclerose múltipla e úlceras.

AGRADECIMENTOS

Ao meu orientador, Doutor João Ferreira, agradeço a confiança depositada, o incentivo e, acima de tudo, o detalhe e cuidado com que apresentou críticas e sugestões, que contribuíram em grande nível para o trabalho desenvolvido. Obrigada, também, por toda a disponibilidade, entusiasmo e amizade demonstrada.

Ao Professor Doutor Marco Parente e ao Professor Doutor Renato Natal, agradeço a oportunidade que me concederam, a confiança e todas as sugestões apresentadas.

Um agradecimento especial para a Doutora Rita Rynkevic pela ajuda na preparação dos tecidos para os ensaios de tração e ao Professor Doutor Jorge Lino por ter cedido a máquina de ensaios para a realização dos mesmos.

Aos meus amigos que estiveram comigo durante estes 5 anos, certamente que o curso poderia ser feito sem vocês, mas não seria o mesmo. Um agradecimento especial a ti, Beatriz, por todo o apoio nos momentos mais difíceis e por teres dito que sim sem hesitar quando te pedi para leres este trabalho.

À minha família: aos meus tios e primos, obrigada pelo incentivo que me deram e por ficarem sempre felizes por mim; aos meus padrinhos, que são imprescindíveis, obrigada pelo especial apoio; e, aos meus queridos avós, obrigada pelo vosso exemplo de dedicação e resiliência.

Aos meus pais, obrigada por acreditarem em mim, por me terem passado os vossos valores e por todo o apoio incondicional que sempre me demonstraram, sem o qual não teria chegado aqui. À minha querida irmã, obrigada por seres a minha maior fã e maior crítica o que só me faz querer ser melhor.

A ti Rui, obrigada por toda a amizade, por acreditares em mim mesmo quando eu não acredito e por teres contribuído para que as imagens desta tese tivessem uma qualidade exímia.

CONTENTS

1. INTRODUCTION	1
1.1 Background and Motivation	1
1.2 Milestones	2
1.3 Thesis Organization.....	3
2. ANATOMY OF THE SMALL INTESTINE	5
2.1 Anatomy of the Small Intestine’s Wall	6
2.2 Smooth Muscle.....	8
2.3 Gastrointestinal Diseases.....	9
2.3.1 Systemic Sclerosis.....	9
2.3.2 Peptic Ulcer Disease.....	10
2.4 Anatomic Inspection and Treatment	11
3. MECHANICAL RESPONSE OF THE SMALL INTESTINE.....	13
3.1 Mechanical Characteristics of the Small Intestine’s Tissue	13
3.2 Motility Patterns	14
3.3 Discussion	17
4. COMPUTATIONAL SOLID MECHANICS	19
4.1 Introduction on Continuum Mechanics	19
4.2 Kinematics.....	19
4.2.1 Configurations of a Continuous Body and Motion	20
4.2.2 Deformation Tensors	21
4.2.3 Polar Decomposition	22
4.2.4 Strain Measures	23
4.2.5 Velocity and Velocity Gradient.....	24
4.3 Concept of Stress.....	24

4.4	Balance Principles	26
4.4.1	Balance of Mass	27
4.4.2	Balance of Linear Momentum.....	27
4.4.1	Balance of Angular Momentum	27
4.5	Constitutive Equations	28
4.5.1	Hyperelasticity.....	28
4.5.2	Elasticity Tensor.....	29
4.5.3	Isotropic Hyperelasticity	29
4.5.4	Incompressible Hyperelasticity	30
4.5.5	Nearly Incompressible Hyperelasticity	31
4.5.6	Transversely Isotropic Hyperelastic Materials	33
4.6	Finite Element Method.....	34
4.6.1	Principle of Virtual Work.....	35
4.6.2	Variational Principles and Incompressibility	36
4.6.3	Linearization of the Principle of Virtual Work	37
4.6.4	Discretization.....	38
5.	MODELLING THE SMALL INTESTINE RESPONSE	41
5.1	Hill Model	41
5.2	Constitutive Model for the Passive and Active Muscle's Behavior	43
5.3	Constitutive Modelling the Small Intestine's Wall with the Martins Model.....	44
5.4	Benchmark Examples	45
5.4.1	UMAT Validation for the Passive Behavior	47
5.4.2	UMAT Validation for the Active Behavior.....	50
6.	EXPERIMENTAL TENSILE TESTS OF THE SMALL INTESTINE.....	53
6.1	Experimental Procedure	53
6.1.1	Sample Preparation.....	53
6.1.2	Uniaxial Tensile Tests	55
6.2	Results	56
6.2.1	Duodenum	56
6.2.2	Ileum.....	57
6.3	Statistical Analysis	59
6.3.1	Thickness.....	59
6.3.2	First Piola-Kirchhoff Stress.....	60
6.4	Passive Properties of the Small Intestine.....	61
6.4.1	Duodenum	61

6.4.2	Ileum.....	62
6.5	Discussion	63
7.	SIMULATION ON THE ACTIVE CONTRACTION OF SMALL INTESTINE	65
7.1	Model.....	65
7.2	Mechanical Properties of the Small Intestine	68
7.2.1	Influence of the Mechanical Properties Diameter Reduction of the Constriction	70
7.3	Activation	72
7.3.1	Influence of the Activation Level Along the Cylinder’s Thickness	73
7.3.2	Implementation of the Peristaltic Wave in the Element Dependent USDFLD	75
7.4	Selecting Initial and Boundary Conditions for the Small Intestine	77
7.5	Selecting Propulsive Resistance	79
7.6	Variation of the Propulsive Capability with the Distal Direction.....	80
7.7	Influence of Chyme Stiffness in Propulsion.....	83
7.8	Influence of Gastrointestinal Limitations in the Chyme Propulsion	84
7.9	Final Remarks.....	86
8.	CONCLUSIONS AND FUTURE WORK.....	87
8.1	Conclusions	87
8.2	Future Work	88
	REFERENCES	89
A	DEFINITION OF THE ELASTICITY TENSOR FOR THE MARTINS MODEL	95

LIST OF FIGURES

Figure 2.1. Portion of the gastrointestinal tract covering the stomach, small (divided into the duodenum, jejunum and ileum) and large intestines [inspired in (Feldman et al. 2010)].	5
Figure 2.2. Laminate structure of the small intestine wall and alignment of the muscle fibers in the muscularis propria and of the collagen fibers in the submucosa [inspired in (Ciarletta et al. 2009)].	6
Figure 2.3. Histology of the duodenum wall in a longitudinal cut with identification of the mucosa (M), submucosa (SM), circular (CM) and longitudinal (LM) muscle layers (a) (Calvo 2020a) and in a transverse cut where the folded configuration of the small intestine mucosa can be identified (b) (Calvo 2020b).	7
Figure 2.4. Time variation of the contractile force during the lag, contraction and relaxation phases of the smooth muscle activation [inspired in (Koeppen and Stanton 2018)].	8
Figure 3.1. Segmentation contractions resultant from the contraction of the circumferential muscle fibers [inspired in (Wood 2004b)].	15
Figure 3.2. Coordinated action of the circular muscle layer and longitudinal muscle layer during a peristaltic contraction, propelling the chyme from the oral (near to the stomach) to the aboral (near to the large intestine) direction [inspired in (Wood 2004a)].	15
Figure 3.3. Progression of the propulsive segment originated by the contraction of the circumferential muscle fibers over 30 mm during a peristaltic contraction.	16
Figure 4.1. Motion of a continuum body \mathcal{B} from the initial Ω_0 to the current Ω configuration [inspired in (Oliver and Saracibar 2017)].	20
Figure 4.2. Transformation of the line, area and volume elements from the material Ω_0 to the spatial Ω configuration [inspired in (Korelc and Wriggers 2016)].	22
Figure 4.3. Stress vectors in the initial Ω_0 and deformed Ω configurations [inspired in (Holzapfel 2000)].	25
Figure 4.4. Newton-Raphson algorithm (Bonet and Wood 2008).	40
Figure 5.1. Hill's muscle model with the contractile (CE), series (SE) and parallel (PE) elements [inspired in (Martins et al. 2006)].	41

Figure 5.2. ABAQUS flowchart and link to the UMAT subroutine for the Martins constitutive model.	46
Figure 5.3. Geometrical configuration of the unitary cube subjected to different load cases.	48
Figure 5.4. Cauchy stress as a function of stretch for a C3D8H finite element with a family of fibers aligned along the directions 0° or 90° subjected to a uniaxial deformation.	49
Figure 5.5. Cauchy stress as a function of stretch for a C3D8H finite element with a family of fibers aligned along the directions 0°, 30°, 45°, 60° or 90° subjected to an equibiaxial deformation.	49
Figure 5.6. Cauchy stress as a function of stretch λ_x for a C3D8H finite element with a family of fibers aligned along the directions 0°, 30°, 45°, 60° or 90° subjected to a biaxial deformation with $\lambda_z = \lambda_{x_{\min}} + \frac{\lambda_x - \lambda_{x_{\min}}}{2}$	50
Figure 5.7. Cauchy stress as a function of stretch for a C3D8H finite element with a family of fibers aligned along the directions 0°, 30°, 45°, 60° or 90° subjected to simple shear.	50
Figure 5.8. Square membrane used for the UMAT validation for active behavior in an isometric contraction (Martins et al. 2006).	51
Figure 5.9. Activation function for an isometric contraction (Martins et al. 2006).....	51
Figure 5.10. Cauchy stress along the direction xx (σ_{xx}) as a function of time in the membrane subjected to an isometric contraction (Martins et al. 2006).	52
Figure 6.1. Small intestine tubular section (b) with the ice burned parts discarded (a).	54
Figure 6.2. Small intestine tube cut along the longitudinal (a) and straightened (b). The undulated edges in the straightened rectangular section are visible in (b).	54
Figure 6.3. Specimens' configuration in the rectangular section (a) and cutting procedure (b).....	55
Figure 6.4. Fixation of the sample in the testing machine: initial (a) and deformed configurations (b).	55
Figure 6.5. Stress-stretch data for the porcine duodenum in the longitudinal (a, c) and transverse directions (b, d). In (c) and (d), the curves were limited by an upper stretch to avoid mechanical damage and the average curves were drawn.....	57
Figure 6.6. Stress-stretch data for the porcine ileum in the longitudinal (a, c) and transverse directions (b, d). In (c) and (d), the curves were limited by an upper stretch to avoid mechanical damage and the average curves were drawn.	58
Figure 6.7. Bar plot indicating the statistically significant difference between the duodenum and ileum thicknesses ($p^{***} < 0.0005$).	59
Figure 6.8. Averaged stress-stretch curves for the porcine duodenum and ileum in the longitudinal and transverse directions with respective standard deviations.	60
Figure 6.9. Bilinear regression of the stress-stretch curves with the slopes E1 and E2.	60

Figure 6.10. Bar plot indicating the statistically significant difference between the longitudinal and transverse directions and between the duodenum and ileum for the slopes E1 and E2 ($p^* < 0.05$, $p^{**} < 0.005$, $p^{***} < 0.0005$).....	61
Figure 6.11. Fitting comparison of the first Piola-Kirchhoff stress for the uniaxial tests in the longitudinal and circumferential directions in the porcine duodenum.	62
Figure 6.12. Fitting comparison of the first Piola-Kirchhoff stress for the uniaxial tests in the longitudinal and circumferential directions in the porcine ileum.	62
Figure 7.1. Biomechanical model of the small intestine as a quarter of a deformable cylinder.....	66
Figure 7.2. Biomechanical model for the chyme propulsion in the small intestine with the chyme modelled as an analytical rigid sphere (a), as a quarter of a deformable sphere (b) and as an analytical rigid sphere connected by springs in its reference point (RP) to built-in points in the axial axis of the cylinder (c).	67
Figure 7.3. Fibers aligned in the circumferential (a) and longitudinal (b) directions.....	69
Figure 7.4. Small intestine ulcers with 5 (top) and 10 mm (bottom) in the inner surface.....	69
Figure 7.5. Connection between the UEXTERNALDB where the fibers direction and ulcer elements are identified and the UMAT subroutine.....	70
Figure 7.6. Influence of the matrix properties (a), passive properties of the longitudinal fibers (b) and active properties of the circumferential fibers (c) in the variation of the lumen relative diameter along the normalized distance of a longitudinal path of the inner surface.	71
Figure 7.7. Activation function in each time increment.	72
Figure 7.8. Flowchart of the position dependent USDFLD and its link to the UMAT subroutine.	72
Figure 7.9. Flowchart of the element dependent USDFLD and its link to the UMAT subroutine.	73
Figure 7.10. Evaluation of the activation level along different paths of the cylinder's thickness applied with the position dependent USDFLD (a) and with the element dependent USDFLD (b).	74
Figure 7.11. Evolution of the activation level (ACT) of the circumferential fibers and reference position (ZREF) during a peristaltic contraction with the time t. The evolution of the ZREF was represented for a cylindrical wedge i ($i = 1, \dots, \text{NCIRC}$), containing a NLRAD number of finite elements, each identified by a number J ranging between $(i - 1)\text{NLRAD} + 1$ and $\text{NLRAD} * i$	76
Figure 7.12. Boundary conditions applied to the small intestine's ends: fixed-fixed Z00 (a), fixed-free Z0F (b) and fixed-springs Z0S (c).....	77
Figure 7.13. Variation of the lumen relative diameter along the normalized distance of a longitudinal path of the inner surface for three sets of boundary conditions applied to the small intestine's ends: fixed-free (Z0F), fixed-springs (Z0S) and fixed-fixed (Z00).....	78
Figure 7.14. Cylinder's boundary conditions: fixed with springs along the longitudinal direction to the ground in the surface Z100 (a); simply supported along the longitudinal direction in the surface Z0 (b); symmetry along the planes Oyz and Oxz (a) and (b).....	79

Figure 7.15. Displacement induced in the chyme by the contraction of the circumferential muscle fibers with variable friction coefficient.	80
Figure 7.16. Displacement induced in the chyme by the contraction of the circumferential muscle fibers with variable spring's stiffness.	80
Figure 7.17. Displacement induced in the chyme by the contraction of the circumferential muscle fibers considering an axial variation of the mechanical properties of the small intestine in the duodenum and ileum.	81
Figure 7.18. Axial reaction force (absolute value) in the chyme measured in the reference point during a contraction of the circumferential muscle fibers considering an axial variation of the mechanical properties of the small intestine in the duodenum and ileum.	82
Figure 7.19. Distribution of the maximum principal stress in a normalized axial path on the inner surface of the small intestine considering an axial variation of the mechanical properties of the small intestine in the duodenum and ileum for $t^* = \frac{1}{3}$	82
Figure 7.20. Displacement induced in the chyme by the contraction of the circumferential muscle fibers with variable chyme's stiffness.	83
Figure 7.21. Distribution of the maximum principal logarithmic strain on the model of the chyme for $t^* = 1$	83
Figure 7.22. Displacement (a) and axial reaction force (absolute value) (b) in the chyme measured in the reference point during a contraction of the circumferential muscle fibers in a normal patient, a SS patient and a patient with an ulcer of variable size.	84
Figure 7.23. Temporal variation of the strain energy in the duodenum for a normal patient, a SS patient and a patient with an ulcer of variable size.	85
Figure 7.24. Distribution of the maximum principal stress in a normalized axial path on the inner surface of the small intestine duodenum for a normal patient, a SS patient and a patient with an ulcer of variable size for $t^* = \frac{1}{3}$	85

LIST OF TABLES

Table 5.1. Deformation gradient, respective deformation and direction of a family of fibers in the unitary undeformed cube for the uniaxial, equibiaxial, biaxial and simple shear stress states.....	47
Table 5.2. Material parameters selected for validation of the passive behavior with the mechanical properties defined in the UMAT subroutine.	48
Table 5.3. Material parameters selected for validation of the active behavior for an isometric contraction with the mechanical properties defined in the UMAT subroutine (Humphrey and Yin 1987).....	51
Table 6.1. Geometrical parameters for the porcine duodenum samples D1 (values in mm).....	56
Table 6.2. Geometrical parameters for the porcine duodenum samples D2 (values in mm).....	56
Table 6.3. Geometrical parameters for the porcine ileum samples (values in mm).	58
Table 6.4. Mean thickness and respective standard deviations for the duodenum and ileum.	59
Table 6.5. Fitted values for the constitutive parameters of the Martins Model for uniaxial traction in the porcine duodenum.	62
Table 6.6. Fitted values for the constitutive parameters of the Martins Model for uniaxial traction in the porcine ileum.....	62

NOMENCLATURE

Physical quantities symbols

a	Scalar value
$\underline{\mathbf{a}}, \underline{\mathbf{A}}$	Vector
\mathbf{A}	Second-order tensor
\mathbb{A}	Fourth-order tensor

Operators

$\nabla_{\underline{\mathbf{x}}}$	Material gradient operator
$\nabla_{\underline{\mathbf{x}}}$	Spatial gradient operator
χ_*	Push-forward operation
$\text{div}_{\underline{\mathbf{x}}}$	Material divergence
$\text{div}_{\underline{\mathbf{x}}}$	Spatial divergence
$:$	Double product
\otimes	Tensor product

Acronyms

FEM	Finite Element Method
FGID	Functional Gastrointestinal Disorder
SS	Systemic Sclerosis
NSAID	Nonsteroidal Anti-inflammatory Drug
DBE	Double-balloon Enteroscopy
VCE	Video Capsule Endoscopy
MMC	Migrating Motor Complex
UMAT	ABAQUS User-subroutine to Define the Mechanical Constitutive Behavior of a Material
USDFLD	ABAQUS User-subroutine to Define Field Variables as Function of Time
C3D8H	Continuum three-dimensional element with 8 nodes, hybrid with constant pressure
C3D8	Continuum three-dimensional element with 8 nodes

Symbols

Ω_0	Initial or material configuration
Ω	Current or spatial configuration
$\underline{\mathbf{X}}$	Material coordinates
$\underline{\mathbf{x}}$	Spatial coordinates
t	Time
$\underline{\mathcal{X}}$	Motion
$\underline{\mathbf{U}}$	Material displacement field
$\underline{\mathbf{u}}$	Spatial displacement field
\mathbf{F}	Deformation gradient
J	Jacobian determinant
\mathbf{I}	Second order identity tensor
$d\underline{\mathbf{X}}$	Line element in the material configuration
$d\underline{\mathbf{S}}$	Surface element in the material configuration
dV	Volume element in the material configuration
$d\underline{\mathbf{x}}$	Line element in the spatial configuration
$d\underline{\mathbf{s}}$	Surface element in the spatial configuration
dv	Volume element in the spatial configuration
\mathbf{C}	Right Cauchy-Green deformation tensor
\mathbf{b}	Left Cauchy-Green deformation tensor
\mathbf{Q}	Rotation tensor
\mathbf{U}	Right stretch tensor
\mathbf{V}	Left stretch tensor
$\boldsymbol{\varepsilon}$	Engineering strain tensor
\mathbf{E}	Green-Lagrange strain tensor
\mathbf{e}	Almansi strain tensor
$\underline{\mathbf{v}}$	Velocity field
\mathbf{l}	Velocity gradient
\mathbf{d}	Rate of deformation tensor
\mathbf{w}	Spin tensor
$\underline{\mathbf{N}}_0$	Outward normal in material configuration
$\underline{\mathbf{n}}_0$	Outward normal in spatial configuration
$\underline{\mathbf{f}}$	Body force vector
$\underline{\mathbf{T}}$	Traction vector in the material configuration
$\underline{\mathbf{t}}$	Traction vector in the spatial configuration
$\boldsymbol{\sigma}$	Cauchy stress tensor

\mathbf{s}	Deviatoric part of the Cauchy stress tensor
p	Hydrostatic pressure
$\boldsymbol{\tau}$	Kirchhoff stress tensor
\mathbf{P}	First Piola-Kirchhoff stress tensor
\mathbf{S}	Second Piola-Kirchhoff stress tensor
m	Mass
ρ_0	Mass density in the material configuration
ρ	Mass density in the spatial configuration
V	Body volume in the material configuration
v	Body volume in the spatial configuration
S	Surface area in the material configuration
s	Surface area in the spatial configuration
$\underline{\mathbf{L}}$	Linear momentum
$\underline{\mathbf{b}}_f$	Volume forces vector
$\underline{\mathbf{J}}$	Angular momentum
$\underline{\mathbf{r}}$	Position vector
Ψ	Strain energy function
\mathbb{C}	Lagrangian or material elasticity tensor
\mathbf{c}	Eulerian or spatial elasticity tensor
$I_{1,2,3}$	Invariants of the right and left Cauchy-Green deformation tensors
$\lambda_{1,2,3}$	Principal stretches
\mathbf{F}_V	Volume-changing part of the deformation gradient
$\bar{\mathbf{F}}$	Isochoric part of the deformation gradient
\mathbf{C}_V	Volume-changing part of the right Cauchy-Green deformation tensor
$\bar{\mathbf{C}}$	Isochoric part of the right Cauchy-Green deformation tensor
Ψ_{vol}	Volume part of the strain energy function
Ψ_{iso}	Isochoric part of the strain energy function
κ	Bulk modulus
\mathbb{I}	Fourth-order unit tensor
\mathbb{P}	Fourth-order projection tensor in the material or spatial configuration
$\bar{I}_{1,2,3}$	Invariants of the isochoric part of the right and left Cauchy-Green deformation tensors
$\bar{\mathbf{S}}$	Isochoric part of the second Piola-Kirchhoff stress tensor
$\bar{\boldsymbol{\sigma}}$	Isochoric part of the Cauchy stress tensor
$\underline{\mathbf{N}}$	Direction of the fibers in the material configuration
$\underline{\mathbf{n}}$	Direction of the fibers in the spatial configuration

λ	Fiber's stretch
$I_{4,5}$	Pseudo-invariant resultant from the anisotropic behavior
$\partial\Omega_{\underline{\mathbf{u}}}$	Displacement boundary of the continuum body
$\partial\Omega_{\underline{\boldsymbol{\sigma}}}$	Traction boundary of the continuum body
$\underline{\boldsymbol{\eta}}$	Weighting or test function
$\delta\mathbf{e}$	Variation of the Euler-Almansi strain tensor
$\delta\mathbf{E}$	Variation of the Green-Lagrange strain tensor
$\delta\underline{\mathbf{u}}$	Virtual displacement field
δW	Virtual work
δW_{int}	Internal virtual work
δW_{ext}	External virtual work
Π	Potential energy
Π_{int}	Internal potential energy
Π_{ext}	External potential energy
N_a	Shape function a
$\underline{\mathbf{R}}$	Residual force
$\underline{\mathbf{F}}_{\text{int}}$	Internal force
$\underline{\mathbf{F}}_{\text{ext}}$	External force
\mathbf{K}	Stiffness matrix
$\mathbf{K}_{\sigma,ab}$	Initial stress component of the stiffness matrix
$\mathbf{K}_{c,ab}$	Material component of the stiffness matrix
$\mathbf{K}_{p,ab}$	External force of the stiffness matrix
F^M	Muscle force
F^{CE}	Force of the contractile element
F^{SE}	Force of the series element
F^{PE}	Force of the passive element
F_O^M	Peak isometric muscle force
L^M	Muscle length
L^{CE}	Length of the contractile element
L^{SE}	Length of the series element
L^{PE}	Length of the passive element
L_O^M	Rest length of the muscle
λ^M	Muscle stretch
α	Activation level
A_O	Physiological cross-sectional area of the muscle

T^{SE}	Stress developed by the series element
T^{PE}	Stress developed by the passive element
T_O^M	Muscle peak stress
Ψ_{mat}	Isotropic matrix contribution to the strain energy function
Ψ_{fib}	Fiber-reinforcement contribution of the strain energy function
Ψ_{PE}	Passive behavior of the fiber-reinforcement contribution to the strain energy function
Ψ_{CE}	Active behavior of the fiber-reinforcement contribution to the strain energy function
$\bar{\lambda}_f$	Stretch ratio of the muscle fibers
D_1	Penalty parameter to ensure incompressibility
c, b	Parameters of the matrix for the Martins constitutive model
A, a	Parameters of the fibers for the Martins constitutive model
t_0	Initial thickness
w_0	Initial width
l_0	Initial length between clamps
l	Final length between clamps
Δy	Displacement of the upper crosshead
RMSE	Root mean-squared error
ζ	Damping factor
\mathbf{M}^*	Artificial mass matrix
\underline{v}	Vector of the nodal velocities
C_{10}	Parameter for the Neo-Hooke constitutive model

CHAPTER 1

INTRODUCTION

1.1 Background and Motivation

Biomechanics is the field of Mechanical Engineering applied to the study of living organisms and their complex biological phenomena, ranging from the cellular level to the tissue level – hard (bone) or soft (skin, muscle, cartilage) tissues. The engineering principles help to make the mechanical behavior of living organisms clearer, through the study of the motion and mechanical responses to forces and displacements, the study of biological fluids and its flow patterns and even through the study of the physiological behavior of the living tissues, useful for the development of Tissue Engineering. Within the subfields of Biomechanics, this work is mainly focused on the Computational, Continuum and Experimental Biomechanics.

Computational Biomechanics applies the computational tools of Mechanical Engineering to the study of biological systems. The Finite Element Method is a powerful numerical method in the analysis of biological systems as it allows simulating the complex geometries of biological structures and the stresses and strains resultant from both a normal or altered behavior (derived from injuries or pathologies), or even from the interaction with medical devices during surgical or examination procedures. With the usage of Computational Biomechanics, the outcomes of new surgical techniques or medical devices can be predicted and the ethical constraints resulting from *in vivo* and *ex vivo* preparations can be avoided, allowing the progressive evolution of the medical procedures.

Continuum Biomechanics is the field of Biomechanics responsible for analyzing the biomaterials and fluids under the Continuum Mechanics Theory. The mechanical properties of materials are expressed by constitutive equations. Unlike many engineering materials, which can be described by the linear elasticity theory, the biological soft tissues present a complex behavior featured by nonlinearities, anisotropy, incompressibility, and viscoelasticity. Therefore, though some constitutive models are already used to describe the behavior of soft tissues, like the isotropic Mooney-Rivlin and Neo-Hooke material models or the anisotropic Martins and Holzapfel-Gasser-Ogden material models, these are still underdeveloped, as other mechanical features of the biological tissues should be considered.

Experimental Biomechanics results from the application of experimental procedures to the biological structures. In fact, by performing simple uniaxial, biaxial and shear mechanical tests to the biological tissues, the stress-strain curves can be plotted and the parameters for each of the constitutive models can be predicted. Continuum and Experimental Mechanics allow the accomplishment of more realistic results from the simulations performed within the finite element simulations.

The simulations performed for a biological system can be performed using the finite element software ABAQUS. Although it is possible to define a wide range of materials, the ABAQUS database of materials is not packed with all constitutive models for biological tissues. However, it has the ability of being tailored, and the constitutive equations can be integrated into a user defined UMAT subroutine, written using the FORTRAN language.

Applied to Gastroenterology, the experimental, numerical, or analytical methods of Biomechanics aids in understanding the smooth muscle activity, the transport of the luminal contents, the tissue growth, the behavior of the intestine under disease and its interaction with the equipment used in medical interventions.

In this thesis, the goal was to model the propulsive behavior of the small intestine under a peristaltic contraction and to compare the results of normal individuals with the results of patients with gastrointestinal limitations, like ulcers or systemic sclerosis. To define the mechanical properties of the small intestine, an UMAT, developed by Ferreira et al. (2017) to describe the Martins model, was used with the constitutive parameters fitted from the experimental stress-strain curves of the uniaxial tests performed. The peristaltic contraction was established by a space and time-dependent variable in a USDFLD subroutine.

1.2 Milestones

The development of the present work was supported by the following set of objectives:

- Understand the small intestine's and its wall constituents' anatomy, mechanical properties and motility;
- Investigate some gastrointestinal limitations, their associated complications and methods of inspection and treatment;
- Analyze the Martins constitutive model and its suitability in describing the mechanical behavior of the small intestine's wall;
- Obtain the fitted constitutive parameter for the Martins model, using the stress-stretch curves acquired through the uniaxial tensile tests performed on the porcine small intestine;
- Validate an existing UMAT subroutine for the Martins model and introduce an USDFLD subroutine for defining the fiber's activation level;

- Define a biomechanical model for the chyme propulsion during a peristaltic contraction in the small intestine and test the propulsive capacity in patients with gastrointestinal limitations.

1.3 Thesis Organization

The Chapter 2 introduces an anatomic description of the small intestine wall, as well as a narrative on the activation process in the smooth muscle cells. Moreover, some gastrointestinal disorders are presented (systemic sclerosis and peptic ulcer disease) alongside the techniques used for their anatomic inspection and for the treatment of the possible complications they might cause.

In the Chapter 3, the mechanical characteristics and the motility patterns of the small intestine are introduced in addition to a description of peristalsis.

The Chapter 4 offers an overview on the Continuum Mechanics and the Finite Element Method theories. This departs from a description of the kinematics, stress and balance principles, followed by the presentation of the constitutive equations for describing isotropic and transversely isotropic hyperelasticity. Only after all this is the Finite Element Method presented.

Chapter 5 focus on presenting the Martins constitutive model and validating the UMAT for the passive and active isometric behavior.

In the Chapter 6, the experimental procedure and results for the uniaxial tests on the porcine small intestine are presented. A statistical analysis is performed to compare mechanical properties over the small intestine's length and direction. Then, a fitting procedure is implemented to obtain the constitutive parameters for the duodenum and ileum.

In the Chapter 7, a biomechanical model of the small intestine chyme propulsion is developed. Several tests are performed to evaluate the influence of the mechanical properties and boundary conditions in the muscular contraction, as well as to validate the USDFLD used for defining the activation variable. In the end, a comparison of the propulsive capability was established between the small intestine sections, between different stiffnesses of the chyme and also between normal individuals and patients suffering from gastrointestinal limitations.

Finally, the Chapter 8 presents the concluding remarks and some suggestions for future improvements in the work developed.

CHAPTER 2

ANATOMY OF THE SMALL INTESTINE

The small intestine is the portion of the gastrointestinal tract that extends from the end of the stomach (pyloric region) to the beginning of the large intestine (ileocecal valve). A major part of the digestion and water and nutrients absorption occurs at this visceral organ, which is commonly divided into 3 segments (duodenum, jejunum and ileum) based on their different functions during the digestive process (Seeley et al. 2007) – Figure 2.1.

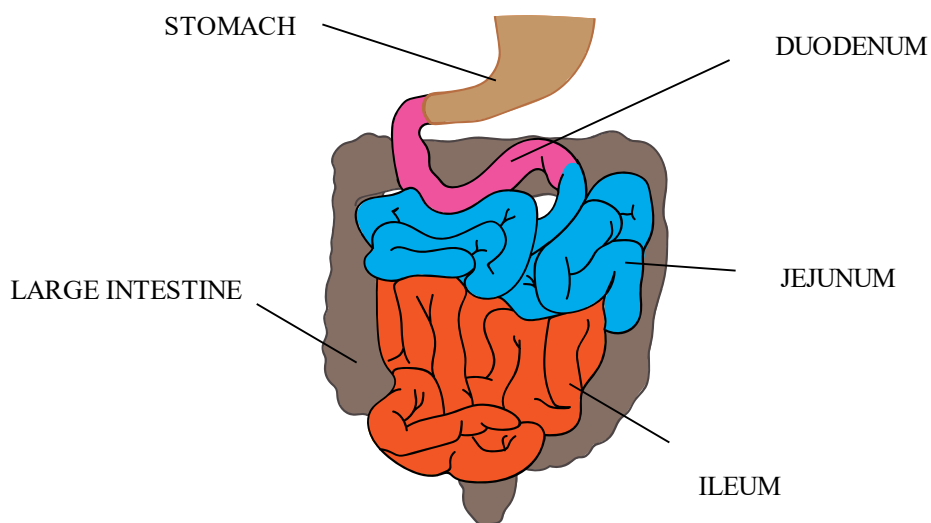


Figure 2.1. Portion of the gastrointestinal tract covering the stomach, small (divided into the duodenum, jejunum and ileum) and large intestines [inspired in (Feldman et al. 2010)].

Besides the distinct performed functions, these segments also differ in their geometric and anatomic structures and mechanical properties. The duodenum is the only portion fixed in a position. The remaining are suspended by the mesentery (organ attaching the small intestine to the posterior abdominal wall), which allows the intestinal movements during its contractions while preventing large deformations and twists (Gregersen 2003).

2.1 Anatomy of the Small Intestine's Wall

The wall of the gastrointestinal tract has a multilayered structure, like a laminate composite, as it is made of several layers with different properties. Considering the direction towards the tube's interior, four main layers can be defined: serosa, muscularis propria, submucosa and mucosa (Seeley et al. 2007) – Figure 2.2.

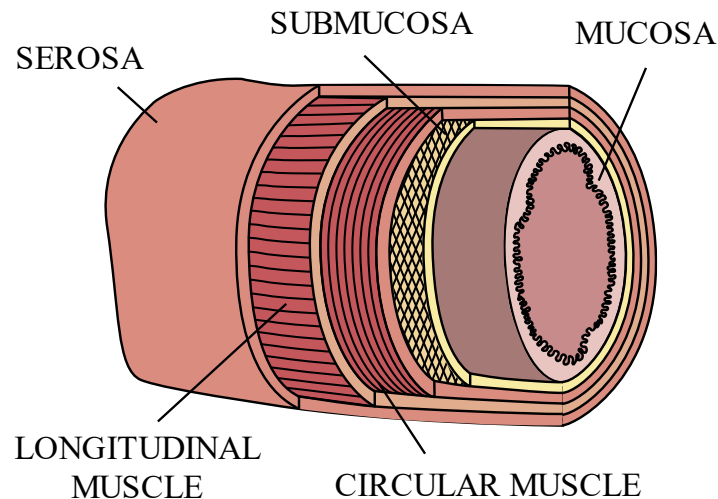


Figure 2.2. Laminate structure of the small intestine wall and alignment of the muscle fibers in the muscularis propria and of the collagen fibers in the submucosa [inspired in (Ciarletta et al. 2009)].

The serosa is a layer of adherent epithelial cells (peritoneum) that surround the intra-abdominal organs. These cells segregate a fluid which forms a thin film over the intra-abdominal organs, reducing the friction between them. The muscularis propria (the main muscle layer) is also covered by the epithelial cells of the serosa (Gregersen 2003).

The muscularis propria is composed of two layers, separated by the myenteric plexus, which differ in the orientation of their smooth muscle cells and are the basis for the small intestine's motility. The outer one, with its cells oriented along the revolution axis of the tube (longitudinal layer), and the inner one, with its cells oriented in the circumferential direction (circular layer) (Gregersen 2003). The cells of Cajal (pacemaker cells which generate the slow wave activity) establish the communication between gastrointestinal muscle cells and the nervous system and serve as mechanoreceptors to the muscle stretch – transducing extracellular mechanical stimulus to intracellular signal. These are located in-between and within the circular and longitudinal muscle layers (Al-Shboul 2013).

The submucosa, the region that separates the main muscle and mucosa, has a massive percentage of collagen and water. The stressed collagen fibers in the submucosa have a $\pm 30^\circ$ orientation from the longitudinal direction (Gregersen 2003).

The mucosa is composed by the muscularis mucosa, whose muscle cells are oriented along their own axis, having no specified direction; by the lamina propria (composed by fibers of collagen and

elastin, scattered small cells and nerve fiber), which is responsible for the attachment of the epithelium to the muscularis mucosa; and, finally, by the gastrointestinal epithelium, which corresponds to the inner surface of the gastrointestinal tract (Gregersen 2003). The epithelial cells, which release secretions to protect the mucosa and lubricate the luminal content (Seeley et al. 2007), are arranged into villi (finger-like projections) and crypts (folds) (Koeppen and Stanton 2018). This anatomic configuration increases the contact area with the chyme and delays the intestinal transit (Avvari 2019).

The histology of the small intestine's wall under a longitudinal and transverse cut is presented in the Figure 2.3.

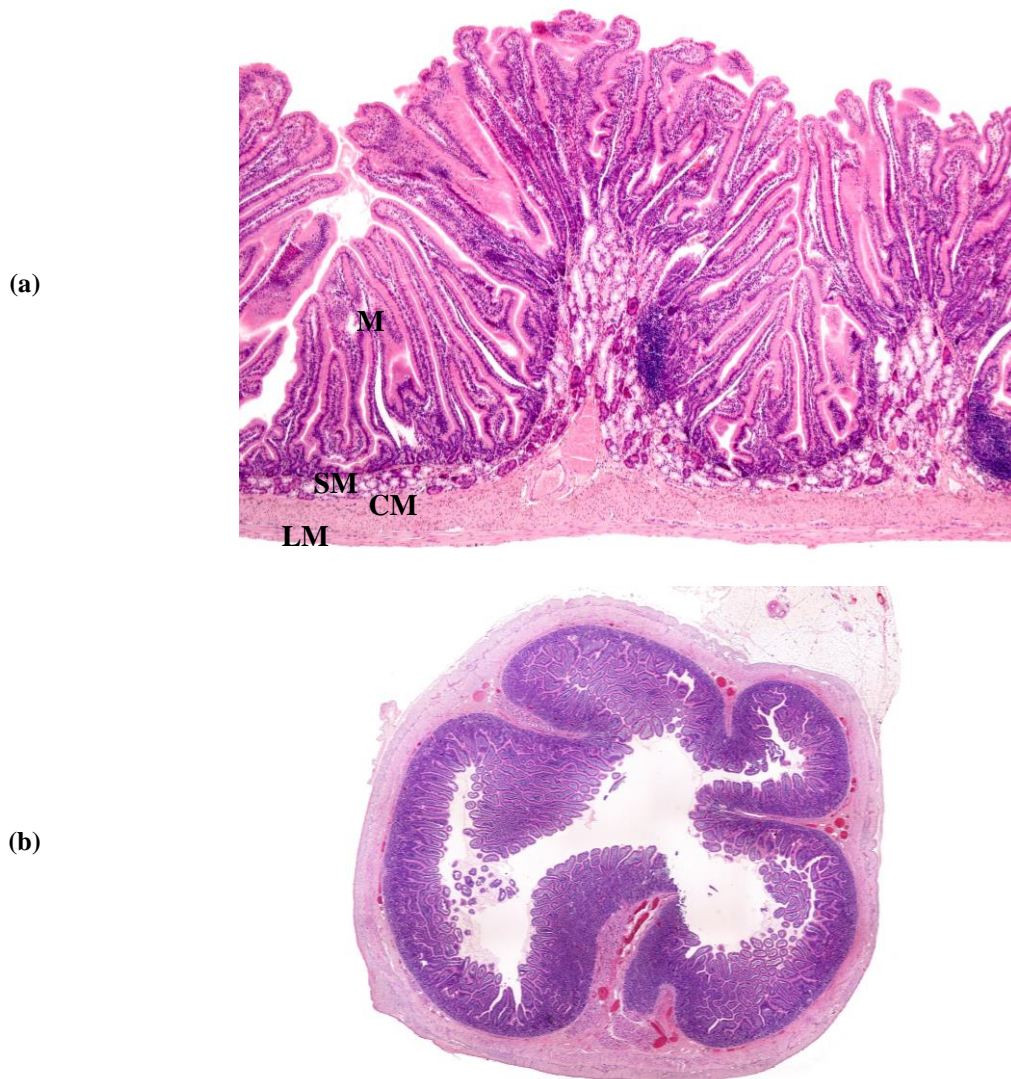


Figure 2.3. Histology of the duodenum wall in a longitudinal cut with identification of the mucosa (M), submucosa (SM), circular (CM) and longitudinal (LM) muscle layers (a) (Calvo 2020a) and in a transverse cut where the folded configuration of the small intestine mucosa can be identified (b) (Calvo 2020b).

2.2 Smooth Muscle

In the gastrointestinal tract, the smooth muscle is considered unitary as it is arranged in bundles of about 1000 fibers which contract together (Guyton and Hall 2006). In this visceral organ, each smooth muscle fiber has a diameter of 2 to 10 μm and a length of 200 to 500 μm . These bundles are separated by connective tissue (Guyton and Hall 2006). The smooth muscle cells are composed of actin and myosin filaments like the skeletal muscle, but these are not arranged in a striated configuration (Guyton and Hall 2006).

The activation process, caused by nervous signals, hormonal stimulations, fiber stretch, etc., is characterized by an increase in the intracellular calcium ions. These trigger the myosin filament, promoting the development of attractive forces between myosin and actin filaments and, consequently, the muscle contraction (Guyton and Hall 2006). This process is slower (2% per unit length per second (Lentle and Loubens 2015)) than the process within the skeletal muscle due to a slower attachment and detachment of the myosin cross-bridges to the actin filament. The smooth muscle contracts 50 to 100 milliseconds after being excited (lag phase). In about 0.5 seconds, it reaches full contraction (contraction phase), which is followed by a relaxation process which may last from 1 to 2 seconds (relaxation phase). Even though this is a typical behavior of the smooth muscle contraction, depending on the type of smooth muscle the total time may vary between 0.2 and 30 seconds. The maximum contractile force can reach 4 to 6 kg/cm^2 of cross-sectional area (Guyton and Hall 2006).

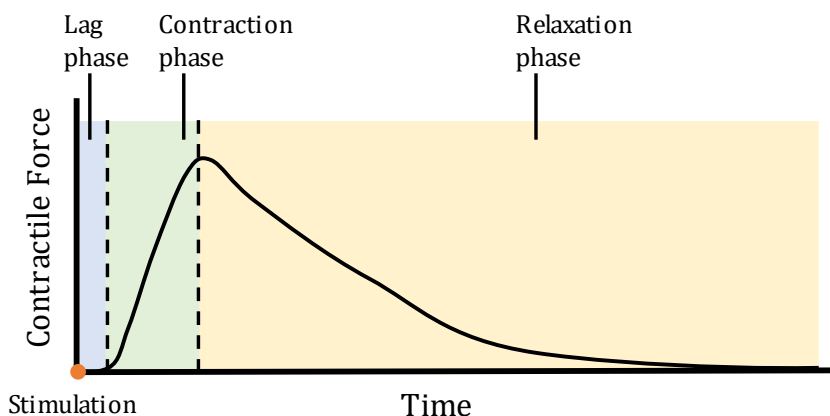


Figure 2.4. Time variation of the contractile force during the lag, contraction and relaxation phases of the smooth muscle activation [inspired in (Koeppen and Stanton 2018)].

The smooth muscle can sustain phasic and tonic contractions. Phasic contractions refer to coordinated contractions of short duration with neural (initiated by the nerve cell) or myogenic (initiated by the smooth muscle cell) stimulation. In the small intestine, peristalsis and segmentation are examples of phasic contractions. Tonic contractions refer to sustained contractions of the muscle fibers that generate tone (continuous muscle tension) (Lentle and Loubens 2015).

2.3 Gastrointestinal Diseases

Regular intestinal motility is essential to guarantee the complete digestive function. The smooth muscle layers' coordinative action and integrity are critical for mixing and propelling the luminal content. However, some patients present gastrointestinal limitations which may negatively influence the normal motility of the intestine, either by changing the wall's mechanical properties or anatomy, the muscle's contractile ability, or the motility patterns (Ghoshal 2019). Furthermore, these limitations can lead to severe complications – some of them of a life-threatening level whose treatment usually requires medical interventions (Feldman et al. 2010).

The scope of diseases affecting the small intestine is large, as well as the associated symptoms and impacts on the quality of the patients' life. In a study conducted in 33 countries spread out over six continents (Sperber et al. 2021), it was found that 40% of the inquired had a functional gastrointestinal disorder (FGID). The FGIDs are disorders affecting the brain-gut connection, which result in movement impairment, hypersensitivity, and altered microbiota. Even though no structural abnormalities can be identified, its symptoms affect the quality of life (Sperber et al. 2021).

Some of the diseases that affect the small intestine are celiac disease, cancer, Crohn's disease, systemic sclerosis and peptic ulcer disease (Feldman et al. 2010). In this subchapter, the systemic sclerosis and peptic ulcer disease are analyzed

2.3.1 Systemic Sclerosis

Systemic sclerosis (SS) is an autoimmune disease, which affects the connective tissue, causing inflammation, progressive degenerative changes, and an increase in the percentage of collagen produced and deposited (fibrosis) in the skin, joints and internal organs, such as the gastrointestinal tract, lungs, and kidneys (Gao et al. 2009).

Symptoms arising from SS in the gastrointestinal tract can be found in over 90% of the patients, while the percentage of severe cases associated with a high mortality rate is about 8% (McFarlane et al. 2018). As a constituent organ of the gastrointestinal tract, the small intestine might be one of the target organs of this chronic disease, being asymptomatic in approximately 65% of the patients (McFarlane et al. 2018). This is the second most affected organ of the gastrointestinal tract, surpassed only by the esophagus. Although SS is a rare disease, with a prevalence of 7.2-33.9 per 100000 individuals in Europe, it decreases deeply the live expectancy of the patients (ten-year survival at 65-76% of patients) (Bergamasco et al. 2019). In fact, the involvement of the gastrointestinal tract in this disease has correlated with a decrease in the survival rate (nine-year survival in 15% of patients), mainly due to problems associated with malabsorption (McFarlane et al. 2018).

In the small intestine, this disease is expressed by intestinal dilatation, muscle atrophy, fibrosis and dysmotility. Dysmotility (associated with slower intestinal transit) is present both as a neuropathic (nerves) atrophy, with absent, abnormal or uncoordinated motility patterns, and myopathic (muscle)

atrophy, with reduced contraction amplitudes (Feldman et al. 2010). Even though dysmotility itself does not present symptoms, it might lead to inertia which favors the overgrowth of bacteria in the small intestine. As a direct consequence, symptoms like nausea, vomiting, diarrhea, bloating, and malabsorption can arise (Shreiner et al. 2016).

To explore the repercussions of the disease in the mechanical properties of the duodenum, Pedersen et al. (2003) have conducted an *in vivo* experiment of balloon distension both in individuals with systemic sclerosis and in healthy individuals to assess the differences. From this study, it was found that the duodenal walls of SS patients presented dilatation and higher stiffness (probably due to the collagen deposition with a higher elastic modulus than the smooth muscle). Moreover, it was noticed that the maximum of the active tension-strain curves in patients with SS occurred at both lower tension and strain. This is an indicator of the muscular atrophy and the fibrosis, which are evidenced through the fact that the muscle is not able to generate the same force as it is in a healthy individual.

2.3.2 Peptic Ulcer Disease

A peptic ulcer is a sore developed in the lower esophagus, stomach or upper small intestine mucosa due to a disparity between the quantity of pepsin (digestive enzyme) and gastric acid secreted by the gastric mucosa, and its neutralization by the alkaline pancreatic juice in the duodenum (Guyton and Hall 2006).

The origin of peptic ulcers is largely associated with a bacterial infection caused by the bacteria *Helicobacter pylori* (7 to 33% of prevalence in the USA and European countries between 2009 and 2011 (Wang and Peura 2011)), whose released digestive enzymes destroy the mucosa. It is also linked to the use of nonsteroidal anti-inflammatory drugs (NSAIDs), which deregulate the mucosa defense mechanisms against acid and pepsin (Feldman et al. 2010). Even though these are the main initiators of peptic ulcers, there are many other factors which can be its facilitators, like stress, smoking and alcohol (Guyton and Hall 2006).

Peptic ulcers can be single or multiple and are diagnosed in endoscopies by mucosal breaks of diameters of 5 mm or higher. Below this minimum diameter, the sores are called erosions (Feldman et al. 2010). In fact, the best way to prevent the peptic ulcer disease and its evolution is through a regular monitorization of the area, resorting to steady endoscopic checkups in response to the appearance of the first symptoms. A common mistake is to use antacids as a way to prevent NSAIDs ulcers as these only relieve the symptoms and enable a silent evolution of the disease (Feldman et al. 2010).

In an initial stage, the symptoms include epigastric pain (associated with hunger), bloated sensation, fullness, and heartburn. However, as the ulcer develops itself, other common complications can arise, such as bleeding, perforation or obstruction (Malfertheiner et al. 2009).

This disease achieved its peak of incidence and mortality rate during the 19th century, being largely associated then with the *H. pylori* infections. With the improvement of sanitary conditions, food and water supply (Feldman et al. 2010) and the development of an efficient treatment with antibiotics

(Guyton and Hall 2006), the amount of infections by this bacteria has decreased, as well as the incidence of peptic ulcers (Feldman et al. 2010) (which is about 0.03% to 0.17% regarding hospitals' diagnostics, according to a literature review between 1997 and 2007 (Sung et al. 2009)). Moreover, the complications associated with the disease have also been reported to be dropping (Laine et al. 2012). Nevertheless, nowadays, peptic ulcer disease remains a real concern, due to a steady increase in the *H. pylori* resistance to antibiotics, which limits its eradication (Almeida et al. 2014). Besides this, the NSAIDs, like ibuprofen and aspirins, are also a rising concern as they are frequently used on a regular basis without medical prescription for relieving pain. In fact, a study conducted in Portugal in 2016 indicated that the prevalence of NSAIDs was of 57,6% and the rate of self-medication with this type of medicine was about 64.2% (Monteiro et al. 2017).

2.4 Anatomic Inspection and Treatment

Several techniques and surgical procedures are implemented to inspect the small intestine mucosa or treat the complications encountered along the tract.

Enteroscopy is a procedure where an endoscope passes through the gastrointestinal tract. In a standard upper enteroscopy, the endoscope field of action is limited to the second portion of the duodenum, whereas in a colonoscopy only a few centimeters of the terminal part of the small intestine (ileum) can be accessed (Feldman et al. 2010).

Other techniques can be used to access the entire length of the small intestine, like the double-balloon enteroscopy (DBE). This technique, introduced in 2001, consists of an endoscope equipped with two balloons, which, once inflated, attach themselves to the small intestine's wall, allowing a controlled maneuver of the endoscope (Feldman et al. 2010).

The techniques previously described allow both the inspection of the tube, as the endoscope has a source of light and video camera incorporated, and also the performance of some medical procedures: collection of tissue fragments for subsequent analysis (biopsy) and treatment of some complications, such as bleeding, polyps removal and obstructions (Feldman et al. 2010).

Another methodology is to use video capsule endoscopy (VCE). VCE is a noninvasive technique used to inspect the entire length of the small intestine mucosa for bleeding but it can equally be used to diagnose Crohn or celiac disease (Feldman et al. 2010). It consists in the ingestion of a capsule of the size of a pill with a LED light, a camera, a battery and a transmitter (Bellini et al. 2017). As the capsule moves forward through the gastrointestinal tract, aided by the natural contractions of the smooth muscle layers, the camera captures images in a rate of 2 frames-per-second (Fernandez-Urien et al. 2014). As the peristaltic movement controls the capsule's motion, the camera's direction is uncontrollable, and some areas might remain inaccessible to the inspection (Ciarletta et al. 2009).

CHAPTER 3

MECHANICAL RESPONSE OF THE SMALL INTESTINE

3.1 Mechanical Characteristics of the Small Intestine's Tissue

The small intestine is a roughly cylindrical structure with high heterogeneity along the wall's radial direction as it is composed by several distinct layers formerly described in the Section 2.1 (Ciarletta et al. 2009). Because of the multilayered wall, the small intestine presents an anisotropic behavior, described by a directional variation of the mechanical properties. The cross-ply arrangement of the collagen fibers in the submucosa and the orientation of the smooth muscle fibers in the muscularis propria have major contributions for the tissue's anisotropy (Ciarletta et al. 2009).

Soft tissues are known for enduring large deformations, within the physiological range (Holzapfel et al. 2000), with a very low level of compressibility (Gregersen 2003). The incompressibility assumption for the small intestine (Ciarletta et al. 2009) (Bellini et al. 2017) is highly motivated by the high percentage of water in the soft tissue's composition (Gilchrist et al. 2014).

Biological tissues have a nonlinear passive response (Martins et al. 1998), which leads to a stiffer mechanical response with an increase in their deformation level (Ciarletta et al. 2009), related to the recruitment of the wavy collagen fibers (Holzapfel et al. 2000). This property is particularly relevant as it helps protecting the small intestine wall against over-distention due to high luminal pressure (Gregersen 2003).

Viscoelasticity is a property than sets stress and strain time-dependent responses. Therefore, the stress depends on the quantity and rate of the applied strain (Gregersen 2003). There are three features of viscoelasticity: stress relaxation (after the material is suddenly deformed, if the strain remains constant, the induced stress decreases over time), creep (after the material is suddenly loaded, if the stress remains constant, the material deformation persists) and hysteresis (when subjected to a cyclic load, the loading and unloading load-deformation curves are different) (Gregersen 2003). The stress-relaxation (ability of the tissue to return to the homeostatic state after being deformed) is vital in hollow organs as it allows a constant lumen pressure even with volume variations (Guyton and Hall 2006). Even

though viscoelasticity is a common property of biological tissues, like the small intestine (Ciarletta et al. 2009), it is out of the scope of this work.

3.2 Motility Patterns

In the small intestine, the smooth muscle produces motility patterns which differ between periods of fasting and periods of food ingestion (Koeppen and Stanton 2018).

The inter-digestive motility pattern is known as migrating motor complex (MMC). It starts right after the digestion and the absorption of nutrients are concluded, being the motility pattern present in fasting or in-between meals periods (Wood 2004a). The purpose of the MMC is to clean the small intestine from undigested food, microorganisms, and dead epithelial cells (Hasler 2004). The MMC is a motility cycle with an average time of 80-120 minutes in humans which is divided into 3 phases. Firstly, it starts with a quiescent period, without contractile activity, which lasts from 40% to 60% of the total duration of the cycle (phase I). Then, it is followed by a period of irregular phasic contractions, which takes over 20% to 30% of the time (phase II). Finally, the cycle ends with a set of strong and regular contractions which last 5 to 10 minutes (phase III) (Hasler 2004). After phase III, the cycle returns to phase I and repeats itself until it is interrupted by the ingestion of food (Wood 2004c).

The digestive motility pattern or fed motor pattern, occurring in the postprandial period (period which follows a meal), is characterized by intermittent phasic contractions of varying amplitude. The duration of this period can change according to the content and volume of the consumed meal, being extended by a higher fat percentage. This pattern is mainly portrayed by two types of mechanical movements: mixing and propulsion over small distances (Hasler 2004).

The small intestine movement in the MMC and in the fed motor pattern is promoted by phasic contractions, with different propagation rates, of the smooth muscle present in the organ's wall: segmentation, pendular activity and peristalsis (Lentle and Loubens 2015).

Segmentation contractions are responsible for mixing the chyme with the bile, pancreatic secretions and intestinal fluid and for enhancing absorption (Seeley et al. 2007), being quite important in the postprandial period (Lentle and Loubens 2015). Segmentation results from alternating stationary contraction/relaxation of the circular muscle layer (Tobergte and Curtis 2013) – Figure 3.1. The pendular activity, occurring both during the MMC and postprandial period, results from non-propulsive contractions of the longitudinal smooth muscle layer (Lentle and Loubens 2015).

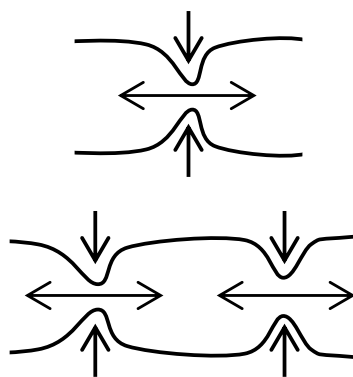


Figure 3.1. Segmentation contractions resultant from the contraction of the circumferential muscle fibers [inspired in (Wood 2004b)].

Peristalsis results from the coordinate contraction/relaxation of the longitudinal and circular muscle layers and it is responsible for propelling the chyme throughout the gastrointestinal tract (Seeley et al. 2007). The distance travelled by the peristaltic wave varies, being smaller in the postprandial period (Lentle and Loubens 2015).

The initiation of the peristalsis occurs after the tube is stretched by the chyme, which induces the activation of the smooth muscle (Koeppen and Stanton 2018). In order to facilitate the analysis, the portion of the tube enduring a peristaltic contraction can be divided into three segments: a segment which does not contract (**A**), the propulsive segment (**B**) and the receiving segment (**C**) (Wood 2004a) – Figure 3.2.

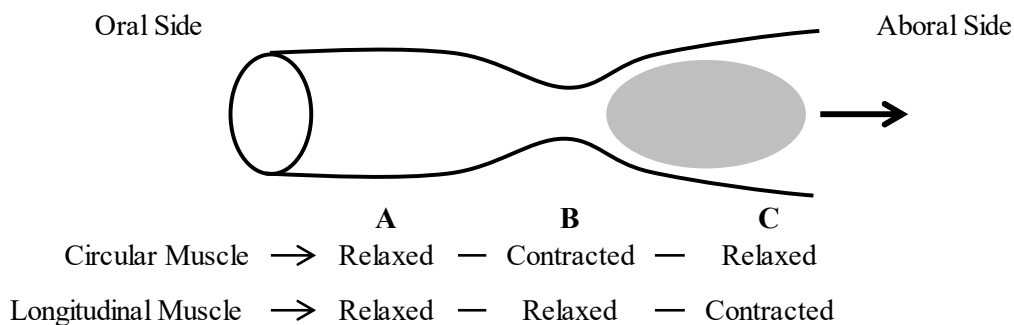


Figure 3.2. Coordinated action of the circular muscle layer and longitudinal muscle layer during a peristaltic contraction, propelling the chyme from the oral (near to the stomach) to the aboral (near to the large intestine) direction [inspired in (Wood 2004a)].

The activation of the circumferential muscle fibers happens from 2 to 3 cm to the left of the chyme (oral side) (Guyton and Hall 2006). This creates the propulsive segment (segment **B**) – a contractile ring with an axial length of 1 to 2 cm (Hasler 2004) – which pushes the luminal content 3 to 5 cm until the peristaltic wave (travelling at a velocity of 0.5 to 2.0 cm/s) dies out (Guyton and Hall 2006). In *ex vivo* preparations with both ends fixed, the tube's diameter reduction in the propulsive segment was reported

up to 40% of its initial size. However, the amplitude of these contractions increases when the intestine is free to shorten. In fact, *in vivo*, as the length of the intestine is not constrained, full occlusion of the lumen may occur (Tobergte and Curtis 2013).

In the Figure 3.3, the progression of a 60% occlusion circular muscle contraction is drawn for a peristaltic wave travelling for 3 cm. Even though they are reported in the literature, the visual parameters considered for drawing the Figure 3.3 are merely illustrative – *in vivo* the shape of the propulsive segment may vary between contractions or even within the same contraction (Tobergte and Curtis 2013). Therefore, despite being considered with axial symmetry during propagation (Figure 3.3), truly, “the occluding segment undergoes progressive lengthening” (Tobergte and Curtis 2013), which means that the downward and the upward segments (of the contractile ring) propagate at different rates in the longitudinal direction (Schulze-Delrieu 1999).

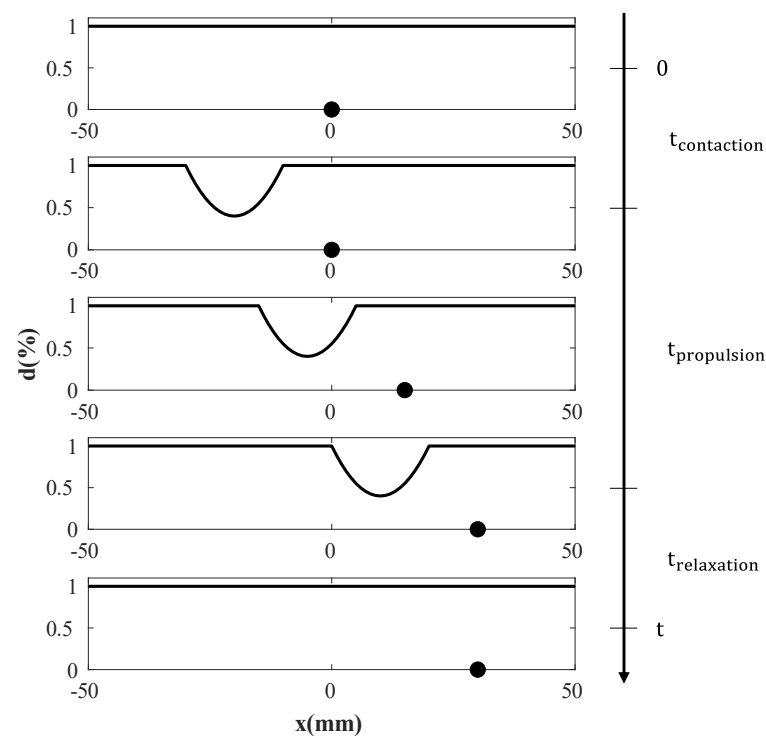


Figure 3.3. Progression of the propulsive segment originated by the contraction of the circumferential muscle fibers over 30 mm during a peristaltic contraction.

In the receiving segment (segment C), the longitudinal muscle contracts, shortening the tube in the axial direction and enlarging it in the radial direction, facilitating the propulsion of the intraluminal content towards this segment (Wood 2004a).

The coordination between the contraction of the muscle layers during the peristaltic event is rather controversive (Tobergte and Curtis 2013). Some authors have reported synchronous contractions (Wood and Perkins 1970), while others described them as being out of phase (Kottegoda 1969). In the spatiotemporal mapping of an *ex vivo* opossum’s small intestine, where the circular and longitudinal

motility was closely recorded, the variation of diameter and longitudinal strain showed that the lumen's constriction in the propulsive segment occurred synchronously with the radial extension in the receiving segment (Lentle et al. 2007).

3.3 Discussion

In Chapter 2, the anatomic structure of the small intestine's wall and some underlying diseases and treatments were evaluated. In this Chapter 3, the mechanical behavior of the small intestine wall and respective motility were accessed.

Thus, an introduction to the physiology of the biological structure (small intestine) was tackled and the respective mechanical considerations accomplished. This corresponds to the first stage of a biomechanical study. Once the biological features and phenomena are understood, the subsequent effects of the diseases, which decrease the life quality and expectancy of the patients, can be studied through Mechanical Engineering methods.

In Gastroenterology, particularly in the case of the small intestine, the application of Biomechanics plays a considerable advantage. It contributes to the evolution of Tissue Engineering since the engineered tissues can be either validated or rejected by the study of in vivo mechanical properties.

The means of inspection and treatment described in Section 2.4 are still being developed nowadays due to the difficulty in accessing the small intestine. In this context, the VCE is probably the most attractive technique to improve because of its non-invasive character. Numerical simulations can help the study of the contact between endoscopic capsules and the gastrointestinal wall. Therefore, its scope could potentially be applicable to capsule maneuver towards specific areas of the small intestine for a more accurate examination (independent of the natural contractions of the organ) or even for tissue collection. Here, simulations could help to understate the injury risks of these techniques for patients.

Patients with gastrointestinal limitations (like celiac disease, cancer, Crohn's disease, SS, and peptic ulcer disease) will likely need medical intervention. However, these patients usually present impaired contractility, distinct passive mechanical, or even an altered pain sensation. So, understanding the propulsion in these patients can simplify the means of accessing and treating possible upcoming complications in their condition.

This work aims to compare the chyme propulsion and force generated in patients with gastrointestinal limitations based on the gathered information. This allows a comparison concerning the impaired propulsion, which ultimately can affect the correct usage of the referred medical devices.

CHAPTER 4

COMPUTATIONAL SOLID MECHANICS

In this chapter, the fundamentals of Continuum Mechanics, constitutive equations for dealing with hyperelastic materials and the Finite Element Method are presented.

The books of Holzapfel (2000), Oliver and Saracibar (2017), Kim (2015), Korelc and Wriggers (2016) and Bonet and Wood (2008) are recommended for a detailed formulation of the concepts of Continuum Mechanics; for the better understanding of the presented constitutive equations and of more complex constitutive models; and for the implementation of the Finite Element Method in large deformations.

4.1 Introduction on Continuum Mechanics

Continuum mechanics is the field of studies whose focus is understanding the material's response under different loading conditions. This theory may be divided into the study of general balance principles applied to all bodies and the constitutive equations defined for a particular material, which may vary depending on the loading conditions (Lai et al. 1996).

A continuum body \mathcal{B} is a continuous distribution of matter in time and space and is composed of a set of particles \mathcal{P} ($\mathcal{P} \in \mathcal{B}$). When referring to a body as continuous, the physical phenomena may be simplified as if the body was a macroscopic system. This simplification takes place due to a lack of relevance of the underlying microscopic events while macroscopically deforming a body. As so, continuum mechanics studies body motion and consequent deformation, and stress generation.

4.2 Kinematics

Kinematics concerns the study of motion and deformation of a continuum body without considering the source of these events. Therefore, the motion of a body along space and time can be defined.

4.2.1 Configurations of a Continuous Body and Motion

A body \mathcal{B} moving through space occupies a sequence of regions $\Omega \in \mathbb{R}^3$, which represent the configurations (deformed state) of this body at a specific time t – Figure 4.1. Therefore, the referential used for describing the behavior of the body under motion is relevant to consider.

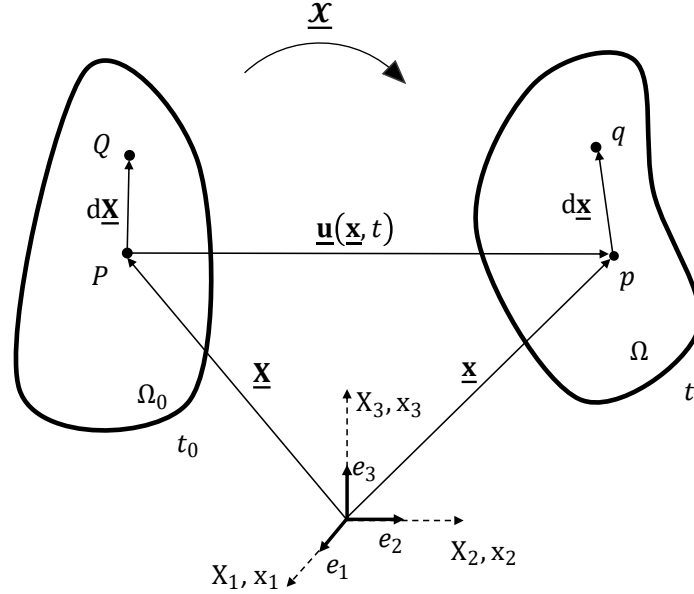


Figure 4.1. Motion of a continuum body \mathcal{B} from the initial Ω_0 to the current Ω configuration [inspired in (Oliver and Saracibar 2017)].

When $t = 0$, the body presents an initial configuration (Ω_0), known as the reference (undeformed) configuration and the position vector of the generical point P is $\underline{\mathbf{X}}$ (material coordinates of the point P). This referential offers a material or Lagrangian description of the variation of the kinematic quantities to be studied.

When a motion $\underline{\mathcal{X}}$ (change in shape, position or orientation) is induced in the body \mathcal{B} , a new region Ω is occupied at a certain time t . This new configuration is called current (deformed) configuration and the position vector $\underline{\mathbf{x}}$ (spatial coordinates of point p) at a certain time t is given by the Equation (4.1). If the current configuration is set as the coordinate system used for describing the kinematic quantities, a spatial or Eulerian description is used.

$$\underline{\mathbf{x}} = \underline{\mathcal{X}}(\underline{\mathbf{X}}, t) \quad (4.1)$$

The motion $\underline{\mathcal{X}}$ is a vector field that relates the current configuration $\underline{\mathbf{x}}$ with the reference configuration $\underline{\mathbf{X}}$ for each time t . As $\underline{\mathcal{X}}$ might be assumed invertible, the position vector $\underline{\mathbf{X}}$ can be written as:

$$\underline{\mathbf{X}} = \underline{\mathcal{X}}^{-1}(\underline{\mathbf{x}}, t) \quad (4.2)$$

The material $\underline{\mathbf{U}}$ and spatial $\underline{\mathbf{u}}$ displacement fields, relating the position $\underline{\mathbf{X}}$ with the position $\underline{\mathbf{x}}$, are defined by the Equation (4.3) and (4.4), accordingly.

$$\underline{\mathbf{U}}(\underline{\mathbf{X}}, t) = \underline{\mathbf{x}}(\underline{\mathbf{X}}, t) - \underline{\mathbf{X}} \quad (4.3)$$

$$\underline{\mathbf{u}}(\underline{\mathbf{x}}, t) = \underline{\mathbf{x}} - \underline{\mathbf{X}}(\underline{\mathbf{x}}, t) \quad (4.4)$$

Looking more carefully into the Equations (4.3) and (4.4), it is possible to deduce that the displacement field is equal in both formulations.

$$\underline{\mathbf{U}}(\underline{\mathbf{X}}, t) = \underline{\mathbf{U}}(\underline{\mathcal{X}}^{-1}(\underline{\mathbf{x}}, t), t) = \underline{\mathbf{u}}(\underline{\mathbf{x}}, t) \quad (4.5)$$

4.2.2 Deformation Tensors

The deformation applied to a body is described by the deformation gradient \mathbf{F} (primary measure of deformation), which is a second order tensor that represents the gradient of the motion $\underline{\mathcal{X}}$ – Equation (4.6). Thus, this enables the linear transformation of the material tangent vector $d\underline{\mathbf{X}}$ into the spatial tangent vector $d\underline{\mathbf{x}}$ – Equation (4.7). The determinant of the deformation gradient is known as the Jacobian determinant J and corresponds to the volume ratio.

$$\mathbf{F}(\underline{\mathbf{X}}, t) = \frac{\partial \underline{\mathcal{X}}(\underline{\mathbf{X}}, t)}{\partial \underline{\mathbf{X}}} = \nabla_{\underline{\mathbf{X}}} \underline{\mathcal{X}}(\underline{\mathbf{X}}, t) \quad (4.6)$$

$$d\underline{\mathbf{x}} = \mathbf{F}(\underline{\mathbf{X}}, t) d\underline{\mathbf{X}} \quad (4.7)$$

As \mathbf{F} and $\nabla_{\underline{\mathbf{x}}}$ are linear, the mapping of the Equation (4.6) is one-to-one, which results in the inexistence of singularities in \mathbf{F} ($J \neq 0$) and in the definition of the inverse deformation gradient $\mathbf{F}^{-1}(\underline{\mathbf{x}}, t)$ – Equation (4.8). Furthermore, the body cannot endure self-penetration, which leads to a Jacobian determinant restricted by $J > 0$. In a volume-preserving or isochoric deformation, the Jacobian determinant is unitary ($J = 1$).

$$\mathbf{F}^{-1}(\underline{\mathbf{x}}, t) = \frac{\partial \underline{\mathcal{X}}^{-1}(\underline{\mathbf{x}}, t)}{\partial \underline{\mathbf{x}}} = \nabla_{\underline{\mathbf{x}}} \underline{\mathcal{X}}^{-1}(\underline{\mathbf{x}}, t) \quad (4.8)$$

The inverse deformation gradient tensor $\mathbf{F}^{-1}(\underline{\mathbf{x}}, t)$ is also a primary measure of deformation which does not represent the description of $\mathbf{F}(\underline{\mathbf{X}}, t)$ in the spatial coordinates, but instead characterizes the displacement's variation in the neighborhood of a spatial point.

The deformation gradient \mathbf{F} and the inverse of the deformation gradient \mathbf{F}^{-1} may also be expressed as a function of the displacement field in the Equations (4.9) and (4.10), where \mathbf{I} is the second order identity tensor.

$$\mathbf{F}(\underline{\mathbf{U}}, t) = \nabla_{\underline{\mathbf{x}}} \underline{\mathbf{U}} + \mathbf{I} \quad (4.9)$$

$$\mathbf{F}^{-1}(\underline{\mathbf{u}}, t) = \nabla_{\underline{\mathbf{x}}} \underline{\mathbf{u}} - \mathbf{I} \quad (4.10)$$

If the deformation gradient \mathbf{F} is independent from the material coordinates $\underline{\mathbf{X}}$, the deformation is said to be homogeneous – $\mathbf{F}(\underline{\mathbf{X}})$. In opposition, the deformation is inhomogeneous if dependent both on time and on the material coordinates – $\mathbf{F}(\underline{\mathbf{X}}, t)$.

Once the deformation gradient and its determinants are defined, the line, surface and volume elements (Figure 4.2) in the spatial configuration ($d\underline{\mathbf{x}}, d\underline{\mathbf{s}}, dv$) can be transformed from the material configuration ($d\underline{\mathbf{X}}, d\underline{\mathbf{S}}, dV$).

$$d\underline{\mathbf{x}} = \mathbf{F} d\underline{\mathbf{X}} \quad (4.11)$$

$$d\underline{\mathbf{s}} = J\mathbf{F}^{-T} d\underline{\mathbf{S}} \quad (4.12)$$

$$dv = J dV \quad (4.13)$$

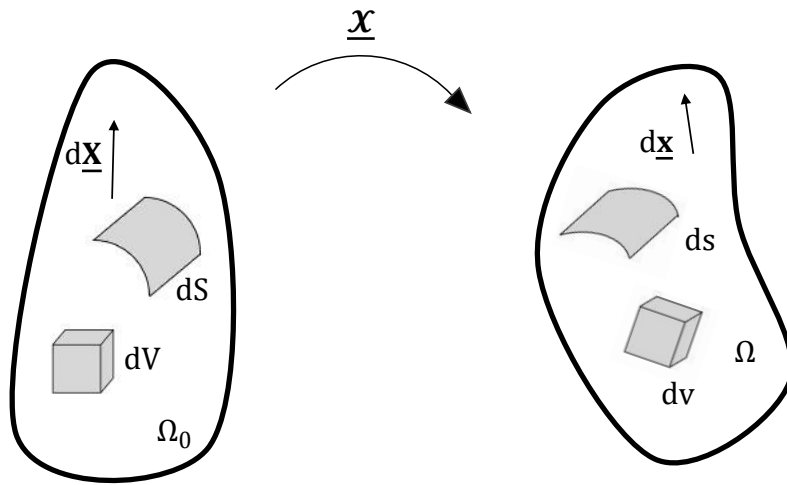


Figure 4.2. Transformation of the line, area and volume elements from the material Ω_0 to the spatial Ω configuration [inspired in (Korelc and Wriggers 2016)].

As the deformation gradient is not a symmetric tensor, it is possible to introduce the right \mathbf{C} and left \mathbf{b} Cauchy-Green deformation tensor in the material and spatial coordinates, respectively – Equations (4.14) and (4.15). These are symmetric and positive second order tensors which eases the development of the constitutive equations.

$$\mathbf{C} = \mathbf{F}^T \mathbf{F} \quad (4.14)$$

$$\mathbf{b} = \mathbf{F} \mathbf{F}^T \quad (4.15)$$

4.2.3 Polar Decomposition

The polar decomposition refers to a decomposition of the deformation gradient \mathbf{F} to differentiate pure rotations from pure stretches. So, a rotational and a stretching part can be accounted. This decomposition is usually performed because the rotational part of the deformation imposed to a body does not have any contribution to the strain.

Using this terminology, three second order tensors can be defined: the rotation tensor \mathbf{Q} , which is orthogonal ($\mathbf{Q}^T \mathbf{Q} = \mathbf{Q} \mathbf{Q}^T = \mathbf{I}$), and the right \mathbf{U} and left \mathbf{V} stretch tensors, which are positive and symmetric – Equations (4.16) and (4.17), respectively.

$$\mathbf{U} = \sqrt{\mathbf{F}^T \mathbf{F}} = \sqrt{\mathbf{C}} \quad (4.16)$$

$$\mathbf{V} = \sqrt{\mathbf{F} \mathbf{F}^T} = \sqrt{\mathbf{B}} \quad (4.17)$$

From the Equations (4.16) and (4.17), it is possible to see that \mathbf{C} and \mathbf{b} are deformation measures independent on the body's rotation.

The deformation gradient can be obtained either by stretching the body first and then rotating it, Equation (4.18), or the other way around – Equation (4.19).

$$\mathbf{F} = \mathbf{Q} \mathbf{U} \quad (4.18)$$

$$\mathbf{F} = \mathbf{V} \mathbf{Q} \quad (4.19)$$

4.2.4 Strain Measures

A body which undergoes deformation can stretch (the relative distance between the undeformed and deformed bodies changes), rotate (the relative distance between the undeformed and deformed bodies remains the same) or stretch and rotate at the same time. So, to quantify the relative motion of a particle in its neighborhood (related with pure stretches), strain measures can be used. Unlike displacements, the strain measures are merely conceptual unmeasurable quantities whose usage may be considered within some limits, but usually results only from mathematical convenience.

The engineering strain tensor $\boldsymbol{\varepsilon}$ is used when infinitesimal deformations occur as the deformed and undeformed configurations are the same – Equation (4.20).

$$\boldsymbol{\varepsilon} = \frac{1}{2} (\nabla_{\underline{\mathbf{x}}} \underline{\mathbf{u}} + \nabla_{\underline{\mathbf{x}}} \underline{\mathbf{u}}^T) = \frac{1}{2} (\nabla_{\underline{\mathbf{x}}} \underline{\mathbf{u}} + \nabla_{\underline{\mathbf{x}}} \underline{\mathbf{u}}^T) \quad (4.20)$$

When a body undergoes large deformations, the deformed configuration is largely different from the undeformed, meaning that they can no longer be considered equal. Moreover, as the strain measures imply deriving the displacement to the reference coordinates it is necessary to set a reference. In this context, two second order tensors can be introduced: the Green Lagrange \mathbf{E} (referent to the material configuration) and the Almansi strain tensor \mathbf{e} (referent to the spatial configuration) – Equations (4.21) and (4.22), respectively.

$$\mathbf{E} = \frac{1}{2} (\nabla_{\underline{\mathbf{x}}} \underline{\mathbf{u}} + \nabla_{\underline{\mathbf{x}}} \underline{\mathbf{u}}^T - \nabla_{\underline{\mathbf{x}}} \underline{\mathbf{u}}^T \nabla_{\underline{\mathbf{x}}} \underline{\mathbf{u}}) = \frac{1}{2} (\mathbf{C} - \mathbf{I}) \quad (4.21)$$

$$\mathbf{e} = \frac{1}{2} (\nabla_{\underline{\mathbf{x}}} \underline{\mathbf{u}} + \nabla_{\underline{\mathbf{x}}} \underline{\mathbf{u}}^T - \nabla_{\underline{\mathbf{x}}} \underline{\mathbf{u}}^T \nabla_{\underline{\mathbf{x}}} \underline{\mathbf{u}}) = \frac{1}{2} (\mathbf{I} - \mathbf{b}^{-1}) \quad (4.22)$$

When the deformation gradient is small enough, the quadratic terms of the Equations (4.21) and (4.22) can be neglected and $\boldsymbol{\varepsilon}$, \mathbf{E} and \mathbf{e} are coincident – Equation (4.20). Comparing these three strain measures, it is possible to state that $\boldsymbol{\varepsilon}$ is not an exact measure of deformation, as it is affected by rigid-body rotation. This should only be used if small strains are present and has the advantage of varying linearly with the displacement gradient. Both \mathbf{E} and \mathbf{e} are strain measures independent from the body's rotation and may be used when a body endures large displacements.

4.2.5 Velocity and Velocity Gradient

In nonlinear problems, motion is a time-dependent quantity. Therefore, it is necessary to obtain some time derivatives of the kinematics quantities.

The velocity of a particle $\underline{\mathbf{v}}(\underline{\mathbf{X}}, t)$ corresponds to the first derivative of the motion $\underline{\mathbf{X}}(\underline{\mathbf{X}}, t)$ in respect to time t – Equation (4.23). Even though it is expressed in terms of material coordinates, velocity $\underline{\mathbf{v}}(\underline{\mathbf{X}}, t)$ is a spatial field. In the Equation (4.24), the velocity field is defined as a function of the spatial coordinates $\underline{\mathbf{v}}(\underline{\mathbf{x}}, t)$.

$$\underline{\mathbf{v}}(\underline{\mathbf{X}}, t) = \frac{\partial \underline{\mathbf{X}}(\underline{\mathbf{X}}, t)}{\partial t} \quad (4.23)$$

$$\underline{\mathbf{v}}(\underline{\mathbf{x}}, t) = \underline{\mathbf{v}}(\underline{\mathbf{X}}^{-1}(\underline{\mathbf{x}}, t), t) \quad (4.24)$$

The velocity gradient \mathbf{l} corresponds to the derivative of the velocity field with respect to the spatial coordinates – Equation (4.25). This can be decomposed into a symmetric part \mathbf{d} (rate of deformation tensor) and a skew part \mathbf{w} (spin tensor).

$$\mathbf{l} = \nabla_{\underline{\mathbf{x}}} \underline{\mathbf{v}} = \frac{\partial \underline{\mathbf{v}}}{\partial \underline{\mathbf{x}}} = \mathbf{d} + \mathbf{w} \quad (4.25)$$

$$\mathbf{d} = \text{sym } \mathbf{l} = \frac{1}{2}(\mathbf{l} + \mathbf{l}^T) \quad (4.26)$$

$$\mathbf{w} = \text{skew } \mathbf{l} = \frac{1}{2}(\mathbf{l} - \mathbf{l}^T) \quad (4.27)$$

4.3 Concept of Stress

Stress is a direct consequence of the interactions between neighboring particles inside a body when it undergoes motion and deformation. Usually, it is defined as a force acting on an infinitesimal area. When analyzing large deformations, the infinitesimal area to be considered differs. Therefore, it is essential to distinguish the stress measures accordingly to the referential in which they are expressed.

Considering an area element Δs , with an outward normal $\underline{\mathbf{n}}_0$ in the spatial point p , the resulting force acting upon this area element is $\Delta \underline{\mathbf{f}}$ – Figure 4.3. Hence, it is possible to define the traction vector

$\underline{\mathbf{t}}$ by the Equation (4.28). The traction vector $\underline{\mathbf{t}}$ is a function of the position vector $\underline{\mathbf{x}}$, of time t and of the outward normal $\underline{\mathbf{n}}_o$.

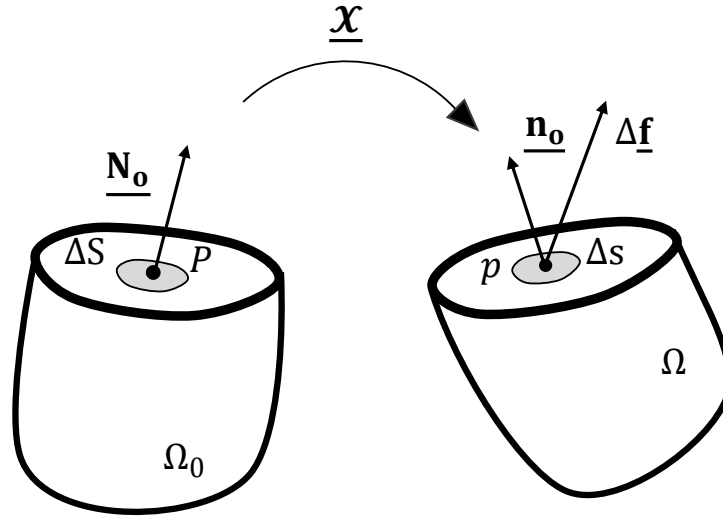


Figure 4.3. Stress vectors in the initial Ω_0 and deformed Ω configurations [inspired in (Holzapfel 2000)].

$$\underline{\mathbf{t}} = \lim_{\Delta s \rightarrow 0} \frac{\Delta \underline{\mathbf{f}}}{\Delta s} = \underline{\boldsymbol{\sigma}} \underline{\mathbf{n}}_o \quad (4.28)$$

From the Equation (4.28), it is also possible to define the Cauchy stress tensor $\boldsymbol{\sigma}$, which is a symmetric second order tensor with six independent components ($\boldsymbol{\sigma} = \boldsymbol{\sigma}^T$), that can be divided into two contributions – a deviatoric \mathbf{s} (related to a change in shape) and a hydrostatic pressure p (related to a change in volume):

$$\boldsymbol{\sigma} = \mathbf{s} + p\mathbf{I} = \mathbf{s} + \frac{1}{3} \text{tr } \boldsymbol{\sigma} \mathbf{I} \quad (4.29)$$

The Cauchy stress tensor is often called true stress as it represents the force per unit area in the current configuration. However, when dealing with large deformations, using stress measures referent to the undeformed configuration can be more effective.

Another symmetric stress tensor commonly used is the Kirchhoff stress tensor $\boldsymbol{\tau}$, which is related to the Cauchy stress tensor through the Jacobian determinant J – Equation (4.30). The Kirchhoff stress tensor is similar to the Cauchy stress tensor, but it refers to the undeformed configuration. This is widely used when isochoric deformations occur.

$$\boldsymbol{\tau} = J\boldsymbol{\sigma} \quad (4.30)$$

Using the same methodology considered to obtain the traction vector $\underline{\mathbf{t}}$ in the deformed configuration, it is also possible to obtain the traction vector $\underline{\mathbf{T}}$ in the undeformed configuration –

Equation (4.31). This depends on the position vector $\underline{\mathbf{X}}$, on time t and on the outward normal $\underline{\mathbf{N}}_0$ – Figure 4.3.

$$\underline{\mathbf{T}} = \lim_{\Delta S \rightarrow 0} \frac{\Delta \mathbf{f}}{\Delta S} = \mathbf{P}^T \underline{\mathbf{n}}_0 \quad (4.31)$$

In the Equation (4.31), it is introduced the first Piola-Kirchhoff stress tensor \mathbf{P} , which is an asymmetric second order tensor referred to the material configuration (it represents a force in the current configuration per unit area in the reference configuration). This can be related to the Cauchy stress tensor as:

$$\mathbf{P} = J \boldsymbol{\sigma} \mathbf{F}^{-T} \quad (4.32)$$

To develop the constitutive equations, symmetric tensors are preferred, a condition which \mathbf{P} fails. When the Equation (4.32) is multiplied by \mathbf{F}^{-1} in the left-side, the second Piola-Kirchhoff stress tensor \mathbf{S} can be obtained – Equation (4.33). This has now the advantage of being symmetric and defined in the material coordinates. However, \mathbf{S} does not have any relation to surface traction.

$$\mathbf{S} = \mathbf{F}^{-1} J \boldsymbol{\sigma} \mathbf{F}^{-T} \quad (4.33)$$

Finally, it is possible to establish a relationship between \mathbf{S} and $\boldsymbol{\sigma}$.

$$\boldsymbol{\sigma} = \frac{1}{J} \mathbf{F} \mathbf{S} \mathbf{F}^T \quad (4.34)$$

The Piola-Kirchhoff stress tensors are simply mathematical quantities and do not express the true stress in the deformed configuration. When small displacements and rotations are applied to a body (linear regime), the previously presented stress measures are coincident, as there is no difference between the initial and deformed configurations.

4.4 Balance Principles

Continuum Mechanics is based on fundamental relations which are valid for all bodies, no matter the materials used and the deformations applied. In this section, the spatial differential formulations of the balances of mass, linear momentum and angular momentum are presented. For problem solving, when these differential formulations are employed, it is said that a strong formulation is used (Reddy 2006).

4.4.1 Balance of Mass

In a deformation process, the mass m of the system should be conserved, which means that the mass is the same in the undeformed Ω_0 and in the deformed Ω configurations – Equation (4.35). The quantities ρ_0 and ρ are the densities in the current and deformed configurations, respectively.

$$m = \int_{\Omega_0} \rho_0 dV = \int_{\Omega} \rho dv \quad (4.35)$$

Therefore, the spatial formulation of the mass conservation can be expressed by:

$$\rho \operatorname{div}_{\underline{x}} \underline{v} + \dot{\rho} = 0 \quad (4.36)$$

4.4.2 Balance of Linear Momentum

The linear momentum \underline{L} is equal both in the initial and deformed configurations.

$$\underline{L} = \int_{\Omega_0} \rho_0 \underline{v} dV = \int_{\Omega} \rho \underline{v} dv \quad (4.37)$$

In a continuous body, there are two types of external forces to be considered: surface traction \underline{t} acting in the body surface $\partial\Omega$, and volume forces \underline{b}_f acting in its volume Ω . The balance of linear momentum corresponds to the equality between the variation of the linear momentum in time and the sum of the external forces acting upon the body – Equation (4.38).

$$\dot{\underline{L}} = \int_{\partial\Omega} \underline{t} ds + \int_{\Omega} \underline{f} dv \quad (4.38)$$

The local balance of linear momentum referred to a volume Ω in the current configuration is given by the Equation (4.39), where $\rho \dot{\underline{v}}$ corresponds to the inertial forces. In a static analysis, $\rho \dot{\underline{v}}$ can be disregarded.

$$\operatorname{div}_{\underline{x}} \underline{\sigma} + \underline{b}_f = \rho \dot{\underline{v}} \quad (4.39)$$

4.4.1 Balance of Angular Momentum

The angular momentum \underline{J} acting on a particle with a position vector \underline{r} is equal in the initial and current configurations – Equation (4.40).

$$\underline{J} = \int_{\Omega_0} \underline{r} \times \rho_0 \underline{v} dV = \int_{\Omega} \underline{r} \times \rho \underline{v} dv \quad (4.40)$$

The balance of angular momentum states that the variation in time of the angular momentum with respect to a point in space is equal to the moments resulting from the external forces acting upon the

body with respect to that same point – Equation (4.41). Finally, the balance of angular momentum results in the Cauchy's stress tensor symmetry $\boldsymbol{\sigma} = \boldsymbol{\sigma}^T$.

$$\underline{\mathbf{j}} = \int_{\partial\Omega} (\underline{\mathbf{r}} \times \underline{\mathbf{t}}) ds + \int_{\Omega} (\underline{\mathbf{r}} \times \underline{\mathbf{b}}_f) dv \quad (4.41)$$

4.5 Constitutive Equations

Besides kinematics, stresses, and balance principles, the complete definition of a body requires the establishment of the constitutive equations that characterize its properties. The constitutive equations are responsible for defining the stress state at a given point and time. These should provide a close representation of the real behavior of a body under the studied conditions.

4.5.1 Hyperelasticity

The hyperelastic materials are examples of nonlinear materials. In these materials, the work done by stress during the deformation process is path independent, meaning that it depends only on the initial Ω_0 and deformed Ω configurations. Therefore, it can be described by a strain energy function Ψ (defined per unit of undeformed volume) which illustrates the elastic strain energy stored in the body.

If the continuum body is inhomogeneous, the strain energy function Ψ relies on the deformation gradient \mathbf{F} and on the position vector $\underline{\mathbf{X}}$: $\Psi(\mathbf{F}, \underline{\mathbf{X}})$. Regarding homogeneous materials, the distribution is assumed as uniform and the strain energy function Ψ depends only on the deformation gradient \mathbf{F} : $\Psi(\mathbf{F})$.

In an hyperelastic material, the first second Piola-Kirchhoff stress tensor \mathbf{P} can be rewritten based on this strain energy function – Equation (4.42).

$$\mathbf{P} = \frac{\partial \Psi(\mathbf{F}, \underline{\mathbf{X}})}{\partial \mathbf{F}} \text{ or } \mathbf{P} = \frac{\partial \Psi(\mathbf{F})}{\partial \mathbf{F}} \quad (4.42)$$

As the strain energy must stay constant under rigid body rotations, \mathbf{F} depends only on the stretch component \mathbf{U} . Since $\mathbf{C} = \mathbf{U}^2$ and $\dot{\mathbf{E}} = \frac{1}{2}\dot{\mathbf{C}}$, Ψ can be expressed as functions of \mathbf{C} or \mathbf{E} – $\Psi(\mathbf{C}, \underline{\mathbf{X}})$ or $\Psi(\mathbf{E}, \underline{\mathbf{X}})$.

Thus, the second Piola-Kirchhoff stress tensor \mathbf{S} and the Cauchy stress tensor $\boldsymbol{\sigma}$ can also be rewritten based on this strain energy function – Equation (4.43) and (4.34).

$$\mathbf{S} = 2 \frac{\partial \Psi(\mathbf{C}, \underline{\mathbf{X}})}{\partial \mathbf{C}} = \frac{\partial \Psi(\mathbf{E}, \underline{\mathbf{X}})}{\partial \mathbf{E}} \text{ or } \mathbf{S} = 2 \frac{\partial \Psi(\mathbf{C})}{\partial \mathbf{C}} = \frac{\partial \Psi(\mathbf{E})}{\partial \mathbf{E}} \quad (4.43)$$

$$\boldsymbol{\sigma} = \frac{2}{J} \mathbf{F} \frac{\partial \Psi(\mathbf{C}, \underline{\mathbf{X}})}{\partial \mathbf{C}} \mathbf{F}^T \text{ or } \boldsymbol{\sigma} = \frac{2}{J} \mathbf{F} \frac{\partial \Psi(\mathbf{C})}{\partial \mathbf{C}} \mathbf{F}^T \quad (4.44)$$

From now on, the strain function is presented as independent from the position vector $\underline{\mathbf{X}}$, only for homogeneous materials.

4.5.2 Elasticity Tensor

In nonlinear problems, the resolution of the equations should be based on an incremental solution of Newton's type. Instead of solving the entire nonlinear problem, this allows the determination of the solution by solving, in each iteration, a linear problem. To achieve the solution, the linearization (based on directional derivatives) of the equations is required.

As in hyperelastic materials, the relation between stress and strain is nonlinear, so there is the need to linearize the constitutive equations. When taking the total differential of \mathbf{S} – Equation (4.45), a fourth-order tensor \mathbb{C} , also known as Lagrangian elasticity tensor, arises. This characterizes the change in stress resulting from a variation in strain and can be written as dependent on \mathbf{C} or \mathbf{E} – Equation (4.46).

$$d\mathbf{S} = 2 \frac{\partial \mathbf{S}(\mathbf{C})}{\partial \mathbf{C}} : \frac{1}{2} d\mathbf{C} = \mathbb{C} : \frac{1}{2} d\mathbf{C} \quad (4.45)$$

$$\mathbb{C} = 2 \frac{\partial \mathbf{S}(\mathbf{C})}{\partial \mathbf{C}} = \frac{\partial \mathbf{S}(\mathbf{E})}{\partial \mathbf{E}} \quad (4.46)$$

For hyperelastic materials, \mathbb{C} can be derived from the energy function Ψ – Equation (4.47), and possesses major symmetries – Equation (4.48).

$$\mathbb{C} = 4 \frac{\partial^2 \Psi(\mathbf{C})}{\partial \mathbf{C} \partial \mathbf{C}} \quad (4.47)$$

$$\mathbb{C} = \mathbb{C}^T \text{ or } C_{ABCD} = C_{CDAB} \quad (4.48)$$

To obtain the elasticity tensor in the spatial configuration \mathbb{c} , it is only necessary to apply a push-forward operation to \mathbb{C} - Equation (4.49).

$$\mathbb{c} = J^{-1} \chi_*(\mathbb{C}) \text{ or } c_{abcd} = \frac{1}{J} F_{aA} F_{bB} F_{cC} F_{dD} C_{ABCD} \quad (4.49)$$

4.5.3 Isotropic Hyperelasticity

When referring to a material as isotropic, this means that its properties are identical in all material directions. Therefore, the strain energy function can be expressed in terms of the invariants I_1 , I_2 and I_3 of \mathbf{C} – Equations (4.50), (4.51) and (4.52).

$$I_1(\mathbf{C}) = \text{tr } \mathbf{C} \quad (4.50)$$

$$I_2(\mathbf{C}) = \frac{1}{2} [(\text{tr } \mathbf{C})^2 - \text{tr}(\mathbf{C}^2)] \quad (4.51)$$

$$I_3(\mathbf{C}) = \det \mathbf{C} = J^2 \quad (4.52)$$

However, as \mathbf{C} and \mathbf{b} have the same eigenvalues λ_1^2 , λ_2^2 and λ_3^2 , then I_1 , I_2 and I_3 are also the invariants of \mathbf{b} – Equations (4.53), (4.54) and (4.55). The quantities λ_1 , λ_2 and λ_3 are the eigenvalues of the right stretch tensor \mathbf{U} and are known as the principal stretches:

$$I_1(\mathbf{C}) = I_1(\mathbf{b}) = \lambda_1^2 + \lambda_2^2 + \lambda_3^2 \quad (4.53)$$

$$I_2(\mathbf{C}) = I_2(\mathbf{b}) = \lambda_1^2 \lambda_2^2 + \lambda_2^2 \lambda_3^2 + \lambda_3^2 \lambda_1^2 \quad (4.54)$$

$$I_3(\mathbf{C}) = I_3(\mathbf{b}) = \lambda_1^2 \lambda_2^2 \lambda_3^2 \quad (4.55)$$

Since the strain energy functions is dependent on the invariants of \mathbf{C} ($\Psi(I_1, I_2, I_3)$), by applying the chain rule, the second Piola-Kirchhoff stress \mathbf{S} can be given by the Equation (4.56).

$$\mathbf{S} = 2 \frac{\partial \Psi(I_1, I_2, I_3)}{\partial \mathbf{C}} = 2 \sum_{i=1}^3 \frac{\partial \Psi(\mathbf{C})}{\partial I_i} \frac{\partial I_i}{\partial \mathbf{C}} \quad (4.56)$$

The derivatives of the invariants I_1 , I_2 and I_3 with respect to \mathbf{C} are:

$$\frac{\partial I_1}{\partial \mathbf{C}} = \mathbf{I} \quad (4.57)$$

$$\frac{\partial I_2}{\partial \mathbf{C}} = I_1 \mathbf{I} - \mathbf{C} \quad (4.58)$$

$$\frac{\partial I_3}{\partial \mathbf{C}} = I_3 \mathbf{C}^{-1} \quad (4.59)$$

By rewriting the Equation (4.56), the second Piola-Kirchhoff stress \mathbf{S} can be obtained – Equation (4.60). Additionally, the Cauchy stress tensor can also be achieved by introducing \mathbf{S} written in terms of the invariants in the Equation (4.34) – Equation (4.61).

$$\mathbf{S} = 2 \left[\left(\frac{\partial \Psi}{\partial I_1} + I_1 \frac{\partial \Psi}{\partial I_2} \right) \mathbf{I} - \frac{\partial \Psi}{\partial I_2} \mathbf{C} + I_3 \frac{\partial \Psi}{\partial I_3} \mathbf{C}^{-1} \right] \quad (4.60)$$

$$\boldsymbol{\sigma} = \frac{2}{J} \left[\left(\frac{\partial \Psi}{\partial I_1} + I_2 \frac{\partial \Psi}{\partial I_2} \right) \mathbf{b} - \frac{\partial \Psi}{\partial I_2} \mathbf{b}^2 + I_3 \frac{\partial \Psi}{\partial I_3} \mathbf{I} \right] \quad (4.61)$$

4.5.4 Incompressible Hyperelasticity

Incompressible hyperelastic materials are deformed without volume changes. They are constrained as their volume must remain constant during deformation: $J = 1$. The strain energy function for incompressible hyperelastic materials can be given as:

$$\Psi = \Psi(\mathbf{F}) - p(J - 1) \quad (4.62)$$

In the Equation (4.62), p corresponds to a Lagrange multiplier, which is used to assure the incompressibility constrain and can be referred as hydrostatic pressure.

The derivative of the Equation (4.62) to \mathbf{F} allows the establishment of the first Piola-Kirchhoff stress tensor \mathbf{P} – Equation (4.63), while the derivative in order to J is the hydrostatic pressure p .

$$\mathbf{P} = \frac{\partial \Psi(\mathbf{F})}{\partial \mathbf{F}} - p \frac{\partial J}{\partial \mathbf{F}} = \frac{\partial \Psi(\mathbf{F})}{\partial \mathbf{F}} - p J \mathbf{F}^T = \frac{\partial \Psi(\mathbf{F})}{\partial \mathbf{F}} - p \mathbf{F}^T \quad (4.63)$$

Through the multiplication of Equation (4.63) by \mathbf{F}^{-1} on the left side, the second Piola-Kirchhoff stress acquires a new formulation – Equation (4.64).

$$\mathbf{S} = \mathbf{F}^{-1} \frac{\partial \Psi(\mathbf{F})}{\partial \mathbf{F}} - p \mathbf{F}^{-1} \mathbf{F}^{-T} = 2 \frac{\partial \Psi(\mathbf{C})}{\partial \mathbf{C}} - p \mathbf{C}^{-1} \quad (4.64)$$

Finally, by substituting \mathbf{S} in the Equation (4.34), the Cauchy stress tensor $\boldsymbol{\sigma}$ can also be defined:

$$\boldsymbol{\sigma} = \frac{\partial \Psi(\mathbf{F})}{\partial \mathbf{F}} \mathbf{F}^T - p \mathbf{I} = \mathbf{F} \left(\frac{\partial \Psi(\mathbf{F})}{\partial \mathbf{F}} \right)^T - p \mathbf{I} \quad (4.65)$$

4.5.5 Nearly Incompressible Hyperelasticity

In constitutive models, dealing with incompressibility is not as easy as one may think, especially when nonlinearities, like large displacements, large strains, or contact, can occur. Even though it is impossible to obtain perfect incompressibility, it is possible to slightly relax the incompressibility restraint, which is referred as nearly incompressible hyperelasticity.

While working with nearly incompressibility, it is useful to split the deformation into a volumetric (dilatational) and an isochoric (distortional) part. Firstly, this helps to reduce the numerical difficulties that arise from distinct mechanical behavior portrayed by different stiffness values: higher in dilatation and smaller in distortion. Additionally, to deal with nearly incompressibility numerically, mixed formulations, where pressure and displacements are independent variables, can be used.

Therefore, the deformation gradient \mathbf{F} can be decomposed into a volume-changing \mathbf{F}_V part and a volume-preserving $\bar{\mathbf{F}}$ part – Equation (4.66). The same methodology can be applied to the right Cauchy-Green deformation tensor – Equation (4.67).

$$\mathbf{F} = \mathbf{F}_V \bar{\mathbf{F}} = \left[(\det \mathbf{F})^{\frac{1}{3}} \mathbf{I} \right] \left[(\det \mathbf{F})^{-\frac{1}{3}} \mathbf{F} \right] = \left[J^{\frac{1}{3}} \mathbf{I} \right] \left[J^{-\frac{1}{3}} \mathbf{F} \right] \quad (4.66)$$

$$\mathbf{C} = \mathbf{C}_V \bar{\mathbf{C}} = \left[(\det \mathbf{F})^{\frac{2}{3}} \mathbf{I} \right] \left[(\det \mathbf{F})^{-\frac{2}{3}} \mathbf{C} \right] = \left[J^{\frac{2}{3}} \mathbf{I} \right] \left[J^{-\frac{2}{3}} \mathbf{C} \right] \quad (4.67)$$

The strain energy function can be given as dependent on \mathbf{C} by the sum of the volumetric $\Psi_{\text{vol}}(J)$ and isochoric $\Psi_{\text{iso}}(\bar{\mathbf{C}})$ elastic responses of the material. In the Equation (4.68), the bulk modulus κ is presented as a penalty number used to ensure incompressibility.

$$\Psi(\mathbf{C}) = \Psi_{\text{vol}}(J) + \Psi_{\text{iso}}(\bar{\mathbf{C}}) = \frac{1}{2} \kappa (J - 1)^2 + \Psi_{\text{iso}}(\bar{\mathbf{C}}) \quad (4.68)$$

The derivative of the Equation (4.68), with respect to J , is given by the Equation (4.69), where the relationship between the hydrostatic pressure and the bulk modulus is established. The hydrostatic pressure is responsible for the volume change in materials. However, in incompressible materials, the volume remains the same when the pressure varies. If the restriction is relaxed, small variations of volume associated with high pressure might occur and they can be imposed using a large bulk modulus.

$$\frac{\partial \Psi(\mathbf{C})}{\partial J} = \kappa (J - 1) = p \quad (4.69)$$

The second Piola-Kirchhoff stress tensor may also be divided into a volumetric \mathbf{S}_{vol} and an isochoric \mathbf{S}_{iso} contribution – Equation (4.70).

$$\begin{aligned} \mathbf{S} &= 2 \frac{\partial \Psi(\mathbf{C})}{\partial \mathbf{C}} = \mathbf{S}_{\text{vol}} + \mathbf{S}_{\text{iso}} = 2 \frac{\partial \Psi_{\text{vol}}(J)}{\partial \mathbf{C}} + 2 \frac{\partial \Psi_{\text{iso}}(\bar{\mathbf{C}})}{\partial \mathbf{C}} \\ &= 2 \frac{\partial \Psi_{\text{vol}}(J)}{\partial J} \frac{\partial J}{\partial \mathbf{C}} + 2 \frac{\partial \Psi_{\text{iso}}(\bar{\mathbf{C}})}{\partial \bar{\mathbf{C}}} \frac{\partial \bar{\mathbf{C}}}{\partial \mathbf{C}} \end{aligned} \quad (4.70)$$

Understanding that $\frac{\partial J}{\partial \mathbf{C}} = \frac{J}{2} \mathbf{C}^{-1}$, it is possible to obtain the derivative of $\bar{\mathbf{C}}$ to \mathbf{C} :

$$\frac{\partial \bar{\mathbf{C}}}{\partial \mathbf{C}} = \frac{\partial \left(J^{-\frac{2}{3}} \mathbf{C} \right)}{\partial \mathbf{C}} = J^{-\frac{2}{3}} \left(\mathbb{I} - \frac{1}{3} \mathbf{C} \otimes \mathbf{C}^{-1} \right) = J^{-\frac{2}{3}} \mathbb{P}^T \quad (4.71)$$

In the Equation (4.71), \mathbb{I} is the fourth-order unit tensor and \mathbb{P}^T is the fourth-order tensor that calculates the transpose of the projection tensor \mathbb{P} (referent to the material configuration).

$$\mathbb{P} = \mathbb{I} - \frac{1}{3} \mathbf{C}^{-1} \otimes \mathbf{C} \quad (4.72)$$

Finally, the second Piola-Kirchhoff is obtained, bearing in mind that $\bar{\mathbf{S}}$ is the fictitious second Piola-Kirchhoff stress.

$$\mathbf{S} = Jp\mathbf{C}^{-1} + 2J^{-\frac{2}{3}} \left(\mathbb{I} - \frac{1}{3} \mathbf{C}^{-1} \otimes \mathbf{C} \right) : \frac{\partial \Psi_{\text{iso}}(\bar{\mathbf{C}})}{\partial \bar{\mathbf{C}}} = Jp\mathbf{C}^{-1} + J^{-\frac{2}{3}} \mathbb{P} : \bar{\mathbf{S}} \quad (4.73)$$

For compressible isotropic hyperelastic materials, the constitutive law can be written in terms of the strain modified invariants \bar{I} – Equation (4.74). However, as an isochoric transformation is subjected to a kinematic constrain ($\bar{I}_3 = 1$), there are only two independent invariants – \bar{I}_1 and \bar{I}_2 .

$$\Psi(\mathbf{C}) = \Psi_{\text{vol}}(J) + \Psi_{\text{iso}}(\bar{I}_1(\bar{\mathbf{C}}), \bar{I}_2(\bar{\mathbf{C}})) \quad (4.74)$$

The invariants \bar{I}_1 , \bar{I}_2 and \bar{I}_3 are the invariants of $\bar{\mathbf{C}}$ and $\bar{\mathbf{b}}$ and can be obtained similarly to the invariants I_1 , I_2 and I_3 .

$$\bar{I}_1 = \text{tr } \bar{\mathbf{C}} = \text{tr } \bar{\mathbf{b}} \quad (4.75)$$

$$\bar{I}_2 = \frac{1}{2} \left[(\text{tr } \bar{\mathbf{C}})^2 - \text{tr}(\bar{\mathbf{C}}^2) \right] = \frac{1}{2} \left[(\text{tr } \bar{\mathbf{b}})^2 - \text{tr}(\bar{\mathbf{b}}^2) \right] \quad (4.76)$$

$$\bar{I}_3 = \det \bar{\mathbf{C}} = \det \bar{\mathbf{b}} \quad (4.77)$$

As the strain energy function is dependent on the invariants of $\bar{\mathbf{C}}$, by applying the chain-rule, the fictitious second Piola-Kirchhoff stress $\bar{\mathbf{S}}$ becomes:

$$\bar{\mathbf{S}} = 2 \sum_{i=1}^2 \frac{\partial \Psi(\bar{\mathbf{C}})}{\partial I_i} \frac{\partial I_i}{\partial \bar{\mathbf{C}}} = 2 \left[\left(\frac{\partial \Psi_{\text{iso}}(\bar{I}_1, \bar{I}_2)}{\partial \bar{I}_1} + \bar{I}_1 \frac{\partial \Psi_{\text{iso}}(\bar{I}_1, \bar{I}_2)}{\partial \bar{I}_2} \right) \mathbf{I} - \frac{\partial \Psi_{\text{iso}}(\bar{I}_1, \bar{I}_2)}{\partial \bar{I}_2} \bar{\mathbf{C}} \right] \quad (4.78)$$

Following a similar approach for the Cauchy stress tensor, it is possible to obtain:

$$\boldsymbol{\sigma} = \boldsymbol{\sigma}_{\text{vol}} + \boldsymbol{\sigma}_{\text{iso}} = p \mathbf{I} + \mathbb{P} : \bar{\boldsymbol{\sigma}} = p \mathbf{I} + \mathbb{P} : \left[\frac{2}{J} \frac{\partial \Psi_{\text{iso}}(\bar{\mathbf{b}})}{\partial \bar{\mathbf{b}}} \bar{\mathbf{b}} \right] \quad (4.79)$$

4.5.6 Transversely Isotropic Hyperelastic Materials

A composite is a heterogeneous material composed of a matrix and one or more families of fibers. In these conditions, since properties are dependent on the material's direction, the material is considered anisotropic.

When a composite material is made up of only one family of fibers arranged along a specified direction, the stiffness is superior in the fibers' direction than it is in the orthogonal direction. This material is called transversely isotropic, because, in the orthogonal direction of the fibers, it is assumed to be isotropic.

In these materials, the stress in a point of the material configuration $\underline{\mathbf{X}}$ is function of both the deformation gradient \mathbf{F} and the fibers' orientation. Therefore, the unit vector field $\underline{\mathbf{N}}(\underline{\mathbf{X}})$, defining the local fibers' direction in the undeformed configuration, can be introduced. When motion is applied, $\underline{\mathbf{N}}(\underline{\mathbf{X}})$ deforms with the body. Under these conditions, the fibers' direction is defined by the unit vector field $\underline{\mathbf{n}}(\underline{\mathbf{x}}, t)$. While deforming, the fibers present a length change – fiber stretch λ – that can be obtained by the Equation (4.80).

$$\lambda \underline{\mathbf{n}} = \mathbf{F} \underline{\mathbf{N}} \quad (4.80)$$

From the definition, $\underline{\mathbf{n}}(\underline{\mathbf{x}}, t)$ is a unit vector ($\|\underline{\mathbf{n}}(\underline{\mathbf{x}}, t)\| = 1$). Thus, it is possible to establish the fibers' stretch as dependent on the undeformed fibers' direction $\underline{\mathbf{N}}$ and on the right Cauchy-Green deformation tensor \mathbf{C} – Equation (4.81).

$$\lambda^2 = \mathbf{F} \underline{\mathbf{N}} \mathbf{F} \underline{\mathbf{N}} = \underline{\mathbf{N}} \mathbf{F}^T \mathbf{F} \underline{\mathbf{N}} = \underline{\mathbf{N}} \mathbf{C} \underline{\mathbf{N}} \quad (4.81)$$

The strain energy function Ψ can be written as function of \mathbf{C} and the second order tensor $\underline{\mathbf{N}} \otimes \underline{\mathbf{N}}$:

$$\Psi = \Psi(\mathbf{C}, \underline{\mathbf{N}} \otimes \underline{\mathbf{N}}) \quad (4.82)$$

While an isotropic hyperelastic material can be defined by the invariants I_1 , I_2 and I_3 , the fully description of a transversely isotropic material requires the additional definition of the invariants I_4 and I_5 , which arise from the anisotropic behavior of the fibers' reinforcement – Equation (4.83) and (4.84).

$$I_4(\mathbf{C}, \mathbf{N}) = \underline{\mathbf{N}} \mathbf{C} \underline{\mathbf{N}} = \lambda^2 \quad (4.83)$$

$$I_5(\mathbf{C}, \mathbf{N}) = \underline{\mathbf{N}} \mathbf{C}^2 \underline{\mathbf{N}} \quad (4.84)$$

Therefore, for a transversely isotropic hyperelastic material, Ψ can be expressed as:

$$\Psi = \Psi(I_1(\mathbf{C}), I_2(\mathbf{C}), I_3(\mathbf{C}), I_4(\mathbf{C}, \mathbf{N}), I_5(\mathbf{C}, \mathbf{N})) \quad (4.85)$$

Finally, it is possible to obtain the second Piola-Kirchhoff and the Cauchy stress tensors:

$$\begin{aligned} \mathbf{S} &= 2 \sum_{i=1}^5 \frac{\partial \Psi(\mathbf{C}, \underline{\mathbf{N}} \otimes \underline{\mathbf{N}})}{\partial I_i} \frac{\partial I_i}{\partial \mathbf{C}} \\ &= 2 \left[\left[\frac{\partial \Psi}{\partial I_1} + I_1 \frac{\partial \Psi}{\partial I_2} \right] \mathbf{I} - \frac{\partial \Psi}{\partial I_2} \mathbf{C} + I_3 \frac{\partial \Psi}{\partial I_3} \mathbf{C}^{-1} + \frac{\partial \Psi}{\partial I_4} \underline{\mathbf{N}} \otimes \underline{\mathbf{N}} + \frac{\partial \Psi}{\partial I_5} (\underline{\mathbf{N}} \otimes \mathbf{C} \underline{\mathbf{N}} + \underline{\mathbf{N}} \mathbf{C} \otimes \underline{\mathbf{N}}) \right] \end{aligned} \quad (4.86)$$

$$\begin{aligned} \boldsymbol{\sigma} &= \frac{2}{J} \left[\left[\frac{\partial \Psi}{\partial I_1} + I_2 \frac{\partial \Psi}{\partial I_2} \right] \mathbf{b} - \frac{\partial \Psi}{\partial I_2} \mathbf{b}^2 + I_3 \frac{\partial \Psi}{\partial I_3} \mathbf{I} \right. \\ &\quad \left. + I_4 \left[\frac{\partial \Psi}{\partial I_4} \underline{\mathbf{N}} \otimes \underline{\mathbf{N}} + \frac{\partial \Psi}{\partial I_5} (\underline{\mathbf{N}} \otimes \mathbf{b} \underline{\mathbf{N}} + \underline{\mathbf{N}} \mathbf{b} \otimes \underline{\mathbf{N}}) \right] \right] \end{aligned} \quad (4.87)$$

4.6 Finite Element Method

The boundary-valued problem has the goal of finding the displacement that fulfills the Equation (4.88), subjected to a displacement and a traction boundary conditions defined in $\partial\Omega_{\underline{\mathbf{u}}}$ and $\partial\Omega_{\boldsymbol{\sigma}}$, respectively. These conditions state that displacements and tractions should be the prescribed values $\underline{\mathbf{u}}^*$ and $\underline{\mathbf{t}}^*$.

$$\begin{aligned} \operatorname{div}_{\underline{\mathbf{x}}} \boldsymbol{\sigma} + \underline{\mathbf{b}}_f &= 0, \quad \underline{\mathbf{x}} \in \Omega \\ \underline{\mathbf{u}} &= \underline{\mathbf{u}}^*, \quad \underline{\mathbf{x}} \in \partial\Omega_{\underline{\mathbf{u}}} \\ \boldsymbol{\sigma} \cdot \underline{\mathbf{n}} &= \underline{\mathbf{t}}^*, \quad \underline{\mathbf{x}} \in \partial\Omega_{\boldsymbol{\sigma}} \end{aligned} \quad (4.88)$$

As the Equation (4.88) should be met for every $\underline{\mathbf{x}} \in \Omega$, it is often called the strong formulation of the boundary-valued problem. The analytical solution of this problem can only be accomplished under very specific conditions, which clarifies the need for the implementation of numerical procedures, like the Finite Element Method.

The FEM is a numerical method used to analyze an equilibrium problem through a division of the problem's complex domain (Ω) into a set of smaller subdomains (Ω_e) – finite elements – connected by

nodes. The idea is that a linear combination of interpolation functions for each element may approximate a continuous function and, so, represent the solution to the problem (Reddy 2006).

4.6.1 Principle of Virtual Work

When an approximation is used for the displacement field $\underline{\mathbf{u}}_h$, a residual $\underline{\mathbf{R}}$ is introduced in the Equation (4.88) – Equation (4.89). This can tend to zero if multiplied by a weighting or test function $\underline{\boldsymbol{\eta}}$ and integrated over the domain Ω – Equation (4.90).

$$\operatorname{div}_{\underline{\mathbf{x}}} \underline{\boldsymbol{\sigma}} + \underline{\mathbf{b}}_f = \underline{\mathbf{R}} \quad (4.89)$$

$$\int_{\Omega} \underline{\mathbf{R}} \cdot \underline{\boldsymbol{\eta}} \, dv = 0 \implies \int_{\Omega} [\operatorname{div}_{\underline{\mathbf{x}}} \underline{\boldsymbol{\sigma}} + \underline{\mathbf{b}}_f] \cdot \underline{\boldsymbol{\eta}} \, dv = 0 \quad (4.90)$$

The Equation (4.91) can be obtained after applying the product rule to $\operatorname{div}_{\underline{\mathbf{x}}} \underline{\boldsymbol{\sigma}} \cdot \underline{\boldsymbol{\eta}}$ and using the divergence theorem.

$$\int_{\Omega} \underline{\boldsymbol{\sigma}} : \nabla_{\underline{\mathbf{x}}} \underline{\boldsymbol{\eta}} \, dv - \int_{\Omega} \underline{\mathbf{b}}_f \cdot \underline{\boldsymbol{\eta}} \, dv - \int_{\partial\Omega} \underline{\boldsymbol{\sigma}} \underline{\boldsymbol{\eta}} \cdot \underline{\mathbf{n}} \, ds = 0 \quad (4.91)$$

Knowing that $\underline{\boldsymbol{\eta}}$ must be zero at the displacement boundaries, the integral over the surface $\partial\Omega$ can be defined simply in $\partial\Omega_{\boldsymbol{\sigma}}$, and the weak or variational form of the boundary-valued problem is obtained – Equation (4.92). Consequently, the difference between natural and essential boundary conditions is set, as the former are defined in $\partial\Omega_{\boldsymbol{\sigma}}$ and the later in $\partial\Omega_{\underline{\mathbf{u}}}$.

$$\int_{\Omega} \underline{\boldsymbol{\sigma}} : \nabla_{\underline{\mathbf{x}}} \underline{\boldsymbol{\eta}} \, dv - \int_{\Omega} \underline{\mathbf{b}}_f \cdot \underline{\boldsymbol{\eta}} \, dv - \int_{\partial\Omega_{\boldsymbol{\sigma}}} \underline{\mathbf{t}} \cdot \underline{\boldsymbol{\eta}} \, ds = 0 \quad (4.92)$$

Considering the symmetry of $\underline{\boldsymbol{\sigma}}$ and the variation of the Euler-Almansi strain tensor $\delta \mathbf{e}$ (Equation (4.93)), it is possible to obtain the Principle of Virtual Work in the current configuration, if the virtual displacement field $\delta \underline{\mathbf{u}}$ is considered as weighting function – Equation (4.94).

$$\delta \mathbf{e} = \operatorname{sym} \left(\nabla_{\underline{\mathbf{x}}} \underline{\boldsymbol{\eta}} \right) = \frac{1}{2} \left[\nabla_{\underline{\mathbf{x}}} \underline{\boldsymbol{\eta}} + \left(\nabla_{\underline{\mathbf{x}}} \underline{\boldsymbol{\eta}} \right)^T \right] \quad (4.93)$$

$$\int_{\Omega} \underline{\boldsymbol{\sigma}} : \delta \mathbf{e} \, dv - \int_{\Omega} \underline{\mathbf{b}}_f \cdot \delta \underline{\mathbf{u}} \, dv - \int_{\partial\Omega_{\boldsymbol{\sigma}}} \underline{\mathbf{t}} \cdot \delta \underline{\mathbf{u}} \, ds = 0 \quad (4.94)$$

The Principle of Virtual Work is a variational principle which states that the virtual stress work (internal virtual work δW_{int}) is equal to the work done by the body and traction forces (external virtual work δW_{ext}).

$$\delta W_{\text{int}}(\underline{\mathbf{u}}, \delta \underline{\mathbf{u}}) = \int_{\Omega} \underline{\boldsymbol{\sigma}} : \delta \underline{\mathbf{e}} \, dv \quad (4.95)$$

$$\delta W_{\text{ext}}(\underline{\mathbf{u}}, \delta \underline{\mathbf{u}}) = \int_{\Omega} \underline{\mathbf{b}}_f \cdot \delta \underline{\mathbf{u}} \, dv + \int_{\partial \Omega_{\sigma}} \underline{\mathbf{t}} \cdot \delta \underline{\mathbf{u}} \, ds \quad (4.96)$$

4.6.2 Variational Principles and Incompressibility

When restrictions are applied to the body's deformation, as in incompressible hyperelastic materials, a single variational principle can lead to numerical difficulties, such as locking (system with over stiffening) and instability phenomena. To overcome these numerical problems, a mixed FEM should be used. This means it is preferable to apply a multi-field variational principle, where each field is handled as an independent variable.

To address the volumetric locking for incompressible hyperelasticity, it is possible to use a two-field variational principle. In this sense, the Lagrange multipliers method and the penalty methods are presented in this section.

The potential energy Π of a system in the material configuration is given by the sum of the internal Π_{int} and external Π_{ext} potential energy – Equation (4.97).

$$\Pi(\underline{\mathbf{u}}) = \Pi_{\text{int}}(\underline{\mathbf{u}}) + \Pi_{\text{ext}}(\underline{\mathbf{u}}) \quad (4.97)$$

$$\Pi_{\text{int}}(\underline{\mathbf{u}}) = \int_{\Omega_0} \Psi(\mathbf{C}) \, dV \quad (4.98)$$

$$\Pi_{\text{ext}}(\underline{\mathbf{u}}) = - \int_{\partial \Omega_{0\sigma}} \underline{\mathbf{t}} \cdot \underline{\mathbf{u}} \, dS - \int_{\Omega_0} \underline{\mathbf{b}}_f \cdot \underline{\mathbf{u}} \, dV \quad (4.99)$$

To obtain the state of equilibrium correspondent to a stationary position of the functional Π , the directional derivative of Π , in respect to the virtual displacement $\delta \underline{\mathbf{u}}$, should be zero. By computing this directional derivative, it is possible to establish the weak form for the equilibrium in the material configuration, which is equivalent to the Principle of Virtual Work – Equation (4.100).

$$D_{\delta \underline{\mathbf{u}}} \Pi(\underline{\mathbf{u}}) = \int_{\Omega_0} \underline{\mathbf{S}} : \delta \underline{\mathbf{E}} \, dV - \int_{\partial \Omega_{0\sigma}} \underline{\mathbf{t}} \cdot \delta \underline{\mathbf{u}} \, dS - \int_{\Omega_0} \underline{\mathbf{b}}_f \cdot \delta \underline{\mathbf{u}} \, dV = 0 \quad (4.100)$$

To enforce incompressibility, it is possible to add the Lagrange multiplier term to the functional $\Pi(\underline{\mathbf{u}})$. Through this approach, the strain energy Ψ is only a function of the volume-preserving $\bar{\mathbf{C}}$, which changes the notation to $\bar{\Pi}(\underline{\mathbf{u}})$. The considered variational $\Pi_L(\underline{\mathbf{u}}, p)$ is now given by the Equation (4.101), where the displacement field $\underline{\mathbf{u}}$ and the hydrostatic pressure p are independent field variables.

$$\begin{aligned}
\Pi_L(\underline{\mathbf{u}}, p) &= \bar{\Pi}(\underline{\mathbf{u}}) + \int_{\Omega_o} p(J - 1) dV \\
&= \int_{\Omega_o} \Psi(\underline{\mathbf{C}}) dV - \int_{\partial\Omega_o\sigma} \underline{\mathbf{t}} \cdot \delta\underline{\mathbf{u}} dS - \int_{\Omega_o} \underline{\mathbf{b}}_f \cdot \delta\underline{\mathbf{u}} dV + \int_{\Omega_o} p(J - 1) dV
\end{aligned} \tag{4.101}$$

Following the approach used to obtain the Equation (4.100), it is possible to find the stationary condition of $\Pi_L(\underline{\mathbf{u}}, p)$ with respect to p :

$$D_{\delta p} \Pi_L(\underline{\mathbf{u}}, p) = \int_{\Omega_o} \delta p (J - 1) dV = 0 \tag{4.102}$$

Another approach to deal with incompressibility is through the usage of penalty methods that allow the elimination of pressure as a problem's variable. The perturbed Lagrangian penalty method can be traduced in a functional $\Pi_P(\underline{\mathbf{u}}, p)$, which results from the addition of a penalty term to $\Pi_L(\underline{\mathbf{u}}, p)$. This penalty term, containing the penalty parameter κ as the bulk modulus, relaxes the incompressibility constrain. So, the Equation (4.103) represents a nearly incompressible material.

$$\Pi_P(\underline{\mathbf{u}}, p) = \Pi_L(\underline{\mathbf{u}}, p) - \int_{\Omega_o} \frac{1}{2\kappa} p^2 dV, \quad \Pi_P \rightarrow \Pi_L \text{ as } \kappa \rightarrow \infty \tag{4.103}$$

The stationary condition of $\Pi_P(\underline{\mathbf{u}}, p)$ with respect to p is given by:

$$D_{\delta p} \Pi_P(\underline{\mathbf{u}}, p) = \int_{\Omega_o} \delta p \left[(J - 1) - \frac{p}{\kappa} \right] dV = 0 \tag{4.104}$$

4.6.3 Linearization of the Principle of Virtual Work

As some problems lead to a nonlinear formulation of the equilibrium equations, the resolution of these equations should be based on an incremental/iterative solution. This allows to obtain approximate numerical solutions even with complex problems. One common method is the Newton-Raphson iterative solution, which, instead of solving the nonlinear problem, allows the determination of the solution by solving, in each iteration, a linear problem. So, in other words, to achieve the solution, the linearization (based on directional derivatives) of the equations is required.

The linearization of the Principle of Virtual Work of the Equation (4.94) in the direction of an increment $\Delta\underline{\mathbf{u}}$ can be achieved in the Equation (4.105), where $D_{\Delta\underline{\mathbf{u}}} \delta W(\underline{\mathbf{u}}, \delta\underline{\mathbf{u}})$ is the directional derivative of the virtual work δW with respect to $\Delta\underline{\mathbf{u}}$ – Equation (4.106).

$$\delta W(\underline{\mathbf{u}}, \delta\underline{\mathbf{u}}) + D_{\Delta\underline{\mathbf{u}}} \delta W(\underline{\mathbf{u}}, \delta\underline{\mathbf{u}}) = 0 \tag{4.105}$$

$$D_{\Delta\underline{\mathbf{u}}} \delta W(\underline{\mathbf{u}}, \delta\underline{\mathbf{u}}) = D_{\Delta\underline{\mathbf{u}}} \delta W_{\text{int}}(\underline{\mathbf{u}}, \delta\underline{\mathbf{u}}) + D_{\Delta\underline{\mathbf{u}}} \delta W_{\text{ext}}(\underline{\mathbf{u}}, \delta\underline{\mathbf{u}}) \tag{4.106}$$

The linearized internal virtual work in the spatial description can be obtained by the Equation (4.107). This formulation is often referred to as an updated Lagrangian formulation since the integrals are calculated over the spatial configuration. Contrarily, if the integrals were calculated over the material configuration, it would be called total Lagrangian formulation.

$$D_{\Delta \underline{\mathbf{u}}} \delta W_{\text{int}}(\underline{\mathbf{u}}, \delta \underline{\mathbf{u}}) = \int_{\Omega} [\nabla_{\underline{\mathbf{x}}} \delta \underline{\mathbf{u}} : \nabla_{\underline{\mathbf{x}}} \Delta \underline{\mathbf{u}} \boldsymbol{\sigma} + \nabla_{\underline{\mathbf{x}}} \delta \underline{\mathbf{u}} : \mathbf{c} : \nabla_{\underline{\mathbf{x}}} \Delta \underline{\mathbf{u}}] dv \quad (4.107)$$

With this incremental/iterative procedure, there are two contributions to be considered in the linearized formulation of the problem: the initial or geometrical stress contribution in each increment ($\nabla_{\underline{\mathbf{x}}} \delta \underline{\mathbf{u}} : \nabla_{\underline{\mathbf{x}}} \Delta \underline{\mathbf{u}} \boldsymbol{\sigma}$) and the material contribution ($\nabla_{\underline{\mathbf{x}}} \delta \underline{\mathbf{u}} : \mathbf{c} : \nabla_{\underline{\mathbf{x}}} \Delta \underline{\mathbf{u}}$).

In a purely static case analysis, the loads are independent from the body's deformation and the correspondent term to the linearization of the external virtual work disappears, leading to:

$$D_{\Delta \underline{\mathbf{u}}} \delta W(\underline{\mathbf{u}}, \delta \underline{\mathbf{u}}) = D_{\Delta \underline{\mathbf{u}}} \delta W_{\text{int}}(\underline{\mathbf{u}}, \delta \underline{\mathbf{u}}) \quad (4.108)$$

4.6.4 Discretization

To apply the FEM, the continuum must be divided into a set of smaller domains – finite elements. Therefore, it is necessary to discretize the kinematic measures and governing equations that describe the body.

In the material configuration, the position vector $\underline{\mathbf{X}}$ can be obtained using shape functions N_a defined for each of the n element nodes and the initial position of these nodes $\underline{\mathbf{X}}_a$ – Equation (4.109). When motion is applied, the position vector of a particle $\underline{\mathbf{x}}$ is defined by the current position of the nodes $\underline{\mathbf{x}}_a$ – Equation (4.110).

$$\underline{\mathbf{X}} = \sum_{a=1}^n N_a \underline{\mathbf{X}}_a \quad (4.109)$$

$$\underline{\mathbf{x}} = \sum_{a=1}^n N_a \underline{\mathbf{x}}_a(t) \quad (4.110)$$

Considering an analysis based on isoparametric elements, the functions used to interpolate the elements geometry $\underline{\mathbf{x}}$ and its displacement field $\underline{\mathbf{u}}$ are the same. Therefore, the displacement field can be obtained in the Equation (4.111), where $\underline{\mathbf{u}}_a$ represents the nodal displacement field. The same approach can be applied for the virtual displacement field in the Equation (4.112).

$$\underline{\mathbf{u}} = \sum_{a=1}^n N_a \underline{\mathbf{u}}_a \quad (4.111)$$

$$\delta \underline{\mathbf{u}} = \sum_{a=1}^n N_a \delta \underline{\mathbf{u}}_a \quad (4.112)$$

Moreover, the deformation gradient \mathbf{F} and the strain measures \mathbf{C} and \mathbf{b} are discretized as:

$$\mathbf{F} = \sum_{a=1}^n \underline{\mathbf{x}}_a \otimes \nabla_{\underline{\mathbf{x}}} N_a \quad (4.113)$$

$$\mathbf{C} = \sum_{a,b}^n (\underline{\mathbf{x}}_a \cdot \underline{\mathbf{x}}_b) \nabla_{\underline{\mathbf{x}}} N_a \otimes \nabla_{\underline{\mathbf{x}}} N_b \quad (4.114)$$

$$\mathbf{b} = \sum_{a,b}^n (\nabla_{\underline{\mathbf{x}}} N_a \otimes \nabla_{\underline{\mathbf{x}}} N_b) \underline{\mathbf{x}}_a \otimes \underline{\mathbf{x}}_b \quad (4.115)$$

Evoking the Equation (4.94), where the virtual work expression was presented, it is now possible to apply a discretization process to the kinematic measures $\delta \mathbf{e}$ and $\delta \underline{\mathbf{u}}$. The virtual work per element (e) and per node a ($\delta W^{(e)}$) can be obtained by:

$$\delta W^{(e)} = \int_{\Omega^{(e)}} \boldsymbol{\sigma} : (\delta \underline{\mathbf{u}}_a \otimes \nabla_{\underline{\mathbf{x}}} N_a) dv - \int_{\Omega^{(e)}} \underline{\mathbf{b}}_f \cdot (N_a \delta \underline{\mathbf{u}}_a) dv - \int_{\partial \Omega_{\sigma}^{(e)}} \underline{\mathbf{t}} \cdot (N_a \delta \underline{\mathbf{u}}_a) ds \quad (4.116)$$

Since the virtual displacement field is independent from the integration, it is possible to rearrange the Equation (4.116) and have $\delta W^{(e)}$ written as a function of the equivalent nodal forces – Equation (4.117). The internal $\underline{\mathbf{F}}_{\text{int}_a}^{(e)}$ and external $\underline{\mathbf{F}}_{\text{ext}_a}^{(e)}$ equivalent nodal forces can be given by the Equations (4.118) and (4.119).

$$\delta W^{(e)} = \delta \underline{\mathbf{u}}_a \left[\int_{\Omega^{(e)}} \boldsymbol{\sigma} \nabla_{\underline{\mathbf{x}}} N_a dv - \int_{\Omega^{(e)}} \underline{\mathbf{b}}_f N_a dv - \int_{\partial \Omega_{\sigma}^{(e)}} \underline{\mathbf{t}} N_a ds \right] = \delta \underline{\mathbf{u}}_a \left[\underline{\mathbf{F}}_{\text{int}_a} - \underline{\mathbf{F}}_{\text{ext}_a} \right]^{(e)} \quad (4.117)$$

$$\underline{\mathbf{F}}_{\text{int}_a}^{(e)} = \int_{\Omega^{(e)}} \boldsymbol{\sigma} \nabla_{\underline{\mathbf{x}}} N_a dv \quad (4.118)$$

$$\underline{\mathbf{F}}_{\text{ext}_a}^{(e)} = \int_{\Omega^{(e)}} \underline{\mathbf{b}}_f N_a dv + \int_{\partial \Omega_{\sigma}^{(e)}} \underline{\mathbf{t}} N_a ds \quad (4.119)$$

Performing the assembly, the equivalent nodal forces $\underline{\mathbf{F}}_{\text{int}_a}$ and $\underline{\mathbf{F}}_{\text{ext}_a}$ are obtained by considering all the elements which contain the node a. The virtual work in a finite element mesh δW can be achieved by considering the contribution of its n nodes.

$$\delta W = \sum_{a=1}^n \delta \underline{\mathbf{u}}_a \cdot \left[\underline{\mathbf{F}}_{\text{int}_a} - \underline{\mathbf{F}}_{\text{ext}_a} \right] = 0 \quad (4.120)$$

As the Equation (4.120) must be satisfied for any arbitrary virtual nodal displacement $\delta \underline{\mathbf{u}}_a$, the nodal residual force $\underline{\mathbf{R}}_a$ in a node a should be zero and it is given by the Equation (4.121).

$$\underline{\mathbf{R}}_a = \underline{\mathbf{F}}_{\text{int}_a} - \underline{\mathbf{F}}_{\text{ext}_a} = 0 \quad (4.121)$$

The equilibrium equations for a nonlinear problem can be given by the Equation (4.122) where $\underline{\mathbf{R}}$, $\underline{\mathbf{F}}_{\text{int}}$ and $\underline{\mathbf{F}}_{\text{ext}}$ are the assembled residual, internal and external forces.

$$\underline{\mathbf{R}} = [\underline{\mathbf{F}}_{\text{int}} - \underline{\mathbf{F}}_{\text{ext}}] = 0 \quad (4.122)$$

The Equation (4.122) can be linearized using the expression present in the Equation (4.105), and it is transformed into:

$$\delta W(\underline{\mathbf{u}}, \delta \underline{\mathbf{u}}) + D_{\Delta \underline{\mathbf{u}}} \delta W(\underline{\mathbf{u}}, \delta \underline{\mathbf{u}}) = \delta \underline{\mathbf{u}}^T \underline{\mathbf{R}} + \delta \underline{\mathbf{u}}^T \underline{\mathbf{K}} \underline{\mathbf{u}} = 0 \quad (4.123)$$

The assembled stiffness matrix $\underline{\mathbf{K}}$ is obtained by performing the assembly of the nodal components. This can be divided into an initial stress component $\underline{\mathbf{K}}_{\sigma,ab}$, a material component $\underline{\mathbf{K}}_{c,ab}$ and an external force component $\underline{\mathbf{K}}_{p,ab}$.

$$\underline{\mathbf{K}} = \frac{\partial \Delta \underline{\boldsymbol{\sigma}}}{\partial \Delta \underline{\boldsymbol{\varepsilon}}} = \underline{\mathbf{K}}_{\sigma,ab} + \underline{\mathbf{K}}_{c,ab} - \underline{\mathbf{K}}_{p,ab} \quad (4.124)$$

The Newton-Raphson algorithm can be summarized in the Figure 4.4 and it follows the Equation (4.125).

$$\underline{\mathbf{K}} \underline{\mathbf{u}} = -\underline{\mathbf{R}}(\underline{\mathbf{x}}_k); \quad \underline{\mathbf{x}}_{k+1} = \underline{\mathbf{x}}_k + \underline{\mathbf{u}} \quad (4.125)$$

```

INPUT geometry and material properties
SET tolerance = tol and max_interactions = max
INITIALIZE  $\underline{\mathbf{x}} = \underline{\mathbf{X}}$ ,  $\underline{\mathbf{F}}_{\text{ext}} = \underline{\mathbf{0}}$ ,  $\underline{\mathbf{R}} = \underline{\mathbf{0}}$ ,  $k = 1$ 
LOOP over load increments
FIND  $\Delta \underline{\mathbf{F}}_{\text{ext}}$  – Equation (4.119)
SET  $\underline{\mathbf{F}}_{\text{ext}} = \underline{\mathbf{F}}_{\text{ext}} + \Delta \underline{\mathbf{F}}_{\text{ext}}$ 
SET  $\underline{\mathbf{R}} = \underline{\mathbf{R}} - \Delta \underline{\mathbf{F}}_{\text{ext}}$ 
DO WHILE  $\left( \frac{\|\underline{\mathbf{R}}\|}{\|\underline{\mathbf{F}}_{\text{ext}}\|} > \textit{tol} \text{ AND } k > \textit{max} \right)$ 
FIND  $\underline{\mathbf{K}}$  – Equation (4.124)
SOLVE  $\underline{\mathbf{K}} \underline{\mathbf{u}} = -\underline{\mathbf{R}}$  – Equation (4.125)
UPDATE  $\underline{\mathbf{x}} = \underline{\mathbf{x}} + \underline{\mathbf{u}}$  – Equation (4.125)
FIND  $\underline{\mathbf{F}}^{(e)}$ ,  $\underline{\mathbf{b}}^{(e)}$ ,  $\underline{\boldsymbol{\sigma}}^{(e)}$  – Equation (4.113) and (4.115)
FIND  $\underline{\mathbf{F}}_{\text{int}}$  – Equation (4.118)
FIND  $\underline{\mathbf{R}}$  – Equation (4.122)
SET  $k = k + 1$ 

```

Figure 4.4. Newton-Raphson algorithm (Bonet and Wood 2008).

CHAPTER 5

MODELLING THE SMALL INTESTINE RESPONSE

In this work, a modified version of the incompressible transversely isotropic hyperelastic model, proposed by Humphrey and Yin (1987), for the passive behavior of the cardiac tissue, is used to model the small intestine mechanical response. This was firstly introduced by the work of Martins et al. (1998) regarding the description of the active and passive behavior of skeletal muscles. The constitutive model is based on the one dimensional muscle model proposed by Hill (1938).

5.1 Hill Model

For a better understanding of the skeletal muscle's activation process, Hill (1938) proposed a one-dimensional (1D) model composed of a contractile element, an in-series elastic element and an in-parallel elastic element – Figure 5.1.

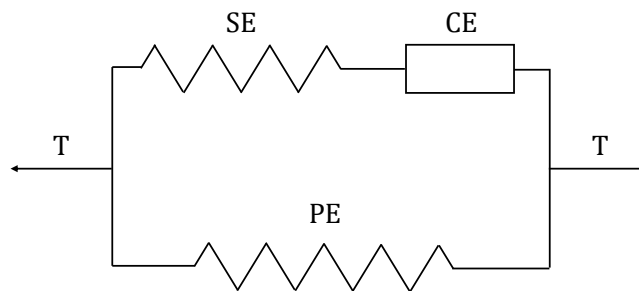


Figure 5.1. Hill's muscle model with the contractile (CE), series (SE) and parallel (PE) elements [inspired in (Martins et al. 2006)].

Analyzing the model in detail, the contractile element (CE) describes the muscle's activation (active part). In this element, the length may increase, but shorten during chemical stimulation. Regarding the two elastic elements, these are nonlinear springs. The series element (SE) is responsible for storing energy and for allowing a state change from inactive to active. The parallel element (PE) is responsible

for the passive behavior of the stretched muscle when the contractile element is deactivated (Martins et al. 2006).

From the Figure 5.1, it is possible to define the muscle force F^M and length L^M , using the force (F^{CE} , F^{SE} , F^{PE}) and length (L^{CE} , L^{SE} , L^{PE}) of each of its constituents.

$$F^M = F^{PE} + F^{SE}, \quad F^{CE} = F^{SE} \quad (5.1)$$

$$L^M = L^{CE} + L^{SE}, \quad L^M = L^{PE} \quad (5.2)$$

When the muscle is fully activated with a constant length of L_0^M (rest/optimal length of the muscle), a force F_0^M (peak isometric muscle force) is induced – maximum force developed by the muscle in an isometric contraction.

If the muscle is non-activated ($F^{CE} = F^{SE} = 0$), a force F^{PE} , which is dependent on the muscle stretch λ^M , is induced in the parallel element. However, this force is null for a compressed muscle.

$$F^{PE} = \begin{cases} F_0^M f_{PE}(\lambda^M) & \lambda^M > 1 \text{ (stretched muscle)} \\ 0 & \lambda^M \leq 1 \text{ (compressed muscle)} \end{cases} \quad (5.3)$$

$$\lambda^M = \frac{L^M}{L_0^M} \quad (5.4)$$

When activated, the muscle develops a force in the contractile element ($F^{CE} = F^{SE}$), dependent on the muscle stretch λ^M and on activation level α (varying from 0 to 1). The velocity of deformation of the contractile element also has an influence in F^{SE} , but it is not considered for the purpose of this work.

$$F^{SE} = F_0^M f_{SE}(\lambda^M, \alpha) \quad (5.5)$$

The function $f_{SE}(\lambda^M, \alpha)$ is equal to a non-zero value if $0.5 < \lambda^M < 1.5$ and it is equal to a zero value if otherwise. This means that no energy is produced by the muscle outside of these limits.

$$f_{SE}(\lambda^M, \alpha) = \alpha \begin{cases} 1 - 4(\lambda^M - 1)^2 & \text{for } 0.5 < \lambda^M < 1.5 \\ 0 & \text{otherwise} \end{cases} \quad (5.6)$$

Dividing the forces F^{PE} and F^{SE} by the muscle's physiological cross-sectional area A_0 , the nonlinear relations for the longitudinal first order Piola-Kirchhoff stresses are given by the Equations (5.7) and (5.8). The parameter T_0^M is the muscle peak stress at isometric conditions and it differs from the studied muscle (Martins et al. 1998).

$$T^{PE} = \frac{F_0^M}{A_0} f_{PE}(\lambda^M) = T_0^M f_{PE}(\lambda^M) \quad (5.7)$$

$$T^{SE} = \frac{F_0^M}{A_0} f_{SE}(\lambda^M, \alpha) = T_0^M f_{SE}(\lambda^M, \alpha) \quad (5.8)$$

5.2 Constitutive Model for the Passive and Active Muscle's Behavior

The Martins model, presented in the works of Martins et al. (1998), Martins et al. (2006) and Parente et al. (2009), considers the strain energy function Ψ divided into a volumetric contribution $\Psi_{\text{vol}}(J)$, an isotropic contribution $\Psi_{\text{mat}}(\bar{\mathbf{I}}_1)$, which represents the energy stored in the matrix, and an anisotropic contribution, describing the energy stored in the fibers $\Psi_{\text{fib}}(\bar{\lambda}_f, \alpha)$ – Equation (5.9).

$$\Psi = \Psi_{\text{vol}}(J) + \Psi_{\text{mat}}(\bar{\mathbf{I}}_1) + \Psi_{\text{fib}}(\bar{\lambda}_f, \alpha) \quad (5.9)$$

The volumetric contribution used to impose the incompressible constrain by a penalty method $\Psi_{\text{vol}}(J)$ can be given by the Equation (5.10) (Parente et al. 2009) or (5.11) (Ferreira et al. 2017). The constant D_1 is related to the bulk modulus as $D_1 = \frac{2}{\kappa}$.

$$\Psi_{\text{vol}}(J) = \frac{1}{D_1} (J - 1)^2 \quad (5.10)$$

$$\Psi_{\text{vol}}(J) = \frac{1}{2D_1} (J^2 - 1 - 2 \ln J) \quad (5.11)$$

The isotropic contribution of the matrix Ψ_{mat} follows an exponential form and depends on the first invariant $\bar{\mathbf{I}}_1$ of the isochoric right Cauchy-Green tensor $\bar{\mathbf{C}}$.

$$\Psi_{\text{mat}}(\bar{\mathbf{I}}_1) = c \left[e^{b(\bar{\mathbf{I}}_1 - 3)} - 1 \right] \quad (5.12)$$

The isochoric contribution of the energy stored in the fibers can be split into a passive contribution Ψ_{PE} and into an active contribution Ψ_{CE} .

$$\Psi_{\text{fib}} = \Psi_{\text{PE}} + \Psi_{\text{CE}} \quad (5.13)$$

Considering a family of fibers along the non-deformed direction $\underline{\mathbf{N}}$, the passive component Ψ_{PE} is given by the exponential function in the Equation (5.14), where (A, a) are the material parameters of the fiber's layer and $\bar{\lambda}_f$ is the fiber's stretch along the non-deformed direction $\underline{\mathbf{N}}$.

$$\Psi_{\text{PE}} = A \left[e^{a(\bar{\lambda}_f - 1)^2} - 1 \right] \quad (5.14)$$

The strain energy function for the contractile behavior Ψ_{CE} is dependent on the fiber's stretch ratio in the direction of the non-deformed fiber $\bar{\lambda}_f$ and on the activation level α .

$$\Psi_{\text{CE}}(\bar{\lambda}_f, \alpha) = T_0^M \int_1^{\bar{\lambda}_f} f_{\text{SE}}(\lambda^M, \alpha) d\lambda^M \quad (5.15)$$

The second Piola-Kirchhoff stress tensor can be obtained by deriving the strain energy Ψ to \mathbf{C} , according to the Equation (4.43). Each contribution can be further developed by applying the chain rule.

$$\mathbf{S} = 2 \frac{\partial \Psi}{\partial \mathbf{C}} = \frac{\partial \Psi}{\partial \mathbf{E}} = \frac{\partial \Psi_{\text{vol}}}{\partial \mathbf{E}} + \frac{\partial \Psi_{\text{mat}}}{\partial \mathbf{E}} + \frac{\partial \Psi_{\text{fib}}}{\partial \mathbf{E}} = \frac{\partial \Psi_{\text{vol}}}{\partial J} \frac{\partial J}{\partial \mathbf{E}} + \frac{\partial \Psi_{\text{mat}}}{\partial \bar{I}_1} \frac{\partial \bar{I}_1}{\partial \mathbf{E}} + \frac{\partial \Psi_{\text{fib}}}{\partial \bar{\lambda}_f} \frac{\partial \bar{\lambda}_f}{\partial \mathbf{E}} \quad (5.16)$$

In the Equations (5.17), (5.18) and (5.19), the first derivatives of Ψ_{vol} , Ψ_{mat} and Ψ_{fib} in order to J , \bar{I}_1 and $\bar{\lambda}_f$, respectively, are presented.

$$\frac{\partial \Psi_{\text{vol}}}{\partial J} = \frac{2}{D_1} (J - 1) \quad (5.17)$$

$$\frac{\partial \Psi_{\text{mat}}}{\partial \bar{I}_1} = bc \left[e^{b(\bar{I}_1 - 3)} \right] \quad (5.18)$$

$$\frac{\partial \Psi_{\text{fib}}}{\partial \bar{\lambda}_f} = 2a(\bar{\lambda}_f - 1)A \left[e^{a(\bar{\lambda}_f - 1)^2} \right] + T_0^M f_{SE}(\bar{\lambda}_f, \alpha) \quad (5.19)$$

The first derivatives of J , \bar{I}_1 and $\bar{\lambda}_f$ to \mathbf{E} are obtained in the Equations (5.20), (5.21) and (5.22).

$$\frac{\partial J}{\partial \mathbf{E}} = J\mathbf{C}^{-1} \quad (5.20)$$

$$\frac{\partial \bar{I}_1}{\partial \mathbf{E}} = 2J^{-\frac{2}{3}} \mathbf{I} - \frac{2}{3} \frac{1}{J} \bar{I}_1 \frac{\partial J}{\partial \mathbf{E}} \quad (5.21)$$

$$\frac{\partial \bar{\lambda}_f}{\partial \mathbf{E}} = J^{-\frac{2}{3}} \frac{1}{\bar{\lambda}_f} (\mathbf{N} \otimes \mathbf{N}) - \frac{1}{3} \frac{\bar{\lambda}_f}{J} \frac{\partial J}{\partial \mathbf{E}} \quad (5.22)$$

The Cauchy stress tensor can be obtained by applying a push-forward operation to the Equation (5.16).

$$\boldsymbol{\sigma} = \frac{1}{J} \left[\mathbf{F} \frac{\partial \Psi_{\text{vol}}}{\partial J} \frac{\partial J}{\partial \mathbf{E}} \mathbf{F}^T + \mathbf{F} \frac{\partial \Psi_{\text{mat}}}{\partial \bar{I}_1} \frac{\partial \bar{I}_1}{\partial \mathbf{E}} \mathbf{F}^T + \mathbf{F} \frac{\partial \Psi_{\text{fib}}}{\partial \bar{\lambda}_f} \frac{\partial \bar{\lambda}_f}{\partial \mathbf{E}} \mathbf{F}^T \right] \quad (5.23)$$

Recalling the Equation (4.46), the material stiffness matrix \mathbb{C} is given by the Equation (5.24). A detailed development of each contribution of \mathbb{C} is performed in the APPENDIX A.

$$\mathbb{C} = \frac{\partial \mathbf{S}}{\partial \mathbf{E}} = \frac{\partial}{\partial \mathbf{E}} \left[\frac{\partial \Psi_{\text{vol}}}{\partial \mathbf{E}} + \frac{\partial \Psi_{\text{mat}}}{\partial \mathbf{E}} + \frac{\partial \Psi_{\text{fib}}}{\partial \mathbf{E}} \right] = \frac{\partial}{\partial \mathbf{E}} \left[\frac{\partial \Psi_{\text{vol}}}{\partial J} \frac{\partial J}{\partial \mathbf{E}} + \frac{\partial \Psi_{\text{mat}}}{\partial \bar{I}_1} \frac{\partial \bar{I}_1}{\partial \mathbf{E}} + \frac{\partial \Psi_{\text{fib}}}{\partial \bar{\lambda}_f} \frac{\partial \bar{\lambda}_f}{\partial \mathbf{E}} \right] \quad (5.24)$$

5.3 Constitutive Modelling the Small Intestine's Wall with the Martins Model

Even though the small intestine's wall presents a multilayered structure (Chapter 3), Egorov et al. (2002). showed that the external loads applied to it are largely supported by the submucosa and muscularis externa. Therefore, having this into consideration, a decoupled form for the strain energy function can be used as motivated by the microstructure of the wall. In their work, Ciarletta et al. (2009) considered the mechanical behavior of the large intestine wall divided into an isotropic matrix and into an anisotropic fiber-reinforcement composed by collagen fibers in the submucosa and by muscle fibers

in the smooth muscle layers. Bearing this in mind and recalling the incompressible nonlinear behavior of the small intestine also present in the Chapter 3, the Martins model for incompressible transversely isotropic hyperelastic materials can be applied to the small intestine by disregarding the influence of collagen fibers.

Considering two families of muscle fibers along the longitudinal and circumferential directions, the second Piola-Kirchhoff stress tensor and the material elasticity tensor can be obtained by the Equations (5.25) and (5.26), where the variables $\bar{\lambda}_1$ and $\bar{\lambda}_c$ are the stretches along the longitudinal and circumferential directions.

$$\mathbf{S} = 2 \frac{\partial \Psi_{\text{vol}}}{\partial J} \frac{\partial J}{\partial \mathbf{C}} + 2 \frac{\partial \Psi_{\text{mat}}}{\partial \bar{I}_1} \frac{\partial \bar{I}_1}{\partial \mathbf{C}} + 2 \frac{\partial \Psi_{\text{fib}}}{\partial \bar{\lambda}_1} \frac{\partial \bar{\lambda}_1}{\partial \mathbf{C}} + 2 \frac{\partial \Psi_{\text{fib}}}{\partial \bar{\lambda}_c} \frac{\partial \bar{\lambda}_c}{\partial \mathbf{C}} \quad (5.25)$$

$$\mathbb{C} = 2 \frac{\partial \mathbf{S}}{\partial \mathbf{C}} = 2 \frac{\partial}{\partial \mathbf{C}} \left(2 \frac{\partial \Psi_{\text{vol}}}{\partial \mathbf{C}} + 2 \frac{\partial \Psi_{\text{mat}}}{\partial \bar{I}_1} \frac{\partial \bar{I}_1}{\partial \mathbf{C}} + 2 \frac{\partial \Psi_{\text{fib}}}{\partial \bar{\lambda}_1} \frac{\partial \bar{\lambda}_1}{\partial \mathbf{C}} + 2 \frac{\partial \Psi_{\text{fib}}}{\partial \bar{\lambda}_c} \frac{\partial \bar{\lambda}_c}{\partial \mathbf{C}} \right) \quad (5.26)$$

5.4 Benchmark Examples

The numerical simulations presented in this work (Chapter 7) were developed using the finite element software ABAQUS. This software models real engineering problems and analyzes the corresponding results. ABAQUS is widely employed due to a substantial range of materials. However, the constitutive models commonly used to model biological tissues are not integrated in the material database. Therefore, the ABAQUS ability to be tailored by user-defined subroutines written in a FORTRAN language is essential to model such materials.

The presented Martins constitutive model, used to model biological tissues, can be integrated in a user-defined material subroutine UMAT where the stress-strain relationship is defined. The basis for the present work departs from an UMAT subroutine previously developed by Ferreira et al. (2017) for the Martins model. The organization of the UMAT subroutine and its link to the ABAQUS flowchart follow the diagram of the Figure 5.2.

To implement the constitutive model in the ABAQUS UMAT subroutine, the Cauchy stress tensor (STRESS) and the stiffness matrix (DDSDDE) should be defined. In this software, the definition of the DDSDDE implies the use of the Jaumann rate of the Kirchhoff stress to ensure quadratic or nearly quadratic convergent in nonlinear problems. As $\boldsymbol{\sigma} = \boldsymbol{\tau}/J$, the stiffness matrix DDSDDE can be obtained by adding the Jaumann rate of the Kirchhoff stress, written in terms of the Cauchy stress tensor, to the spatial elasticity tensor \mathbb{c} – Equation (5.27) (Stein and Sagar 2008).

$$\text{DDSDDE} = \mathbb{c} + \frac{1}{2} [\mathbf{I} \otimes \boldsymbol{\sigma} + \boldsymbol{\sigma} \otimes \mathbf{I} + \mathbf{I} \otimes \boldsymbol{\sigma} + \boldsymbol{\sigma} \otimes \mathbf{I}] \quad (5.27)$$

In this subsection, the validation of this UMAT for the passive behavior and active isometric contraction is presented. This step is imperative to verify that the results obtained with the UMAT were equal to the analytical or literature solutions.

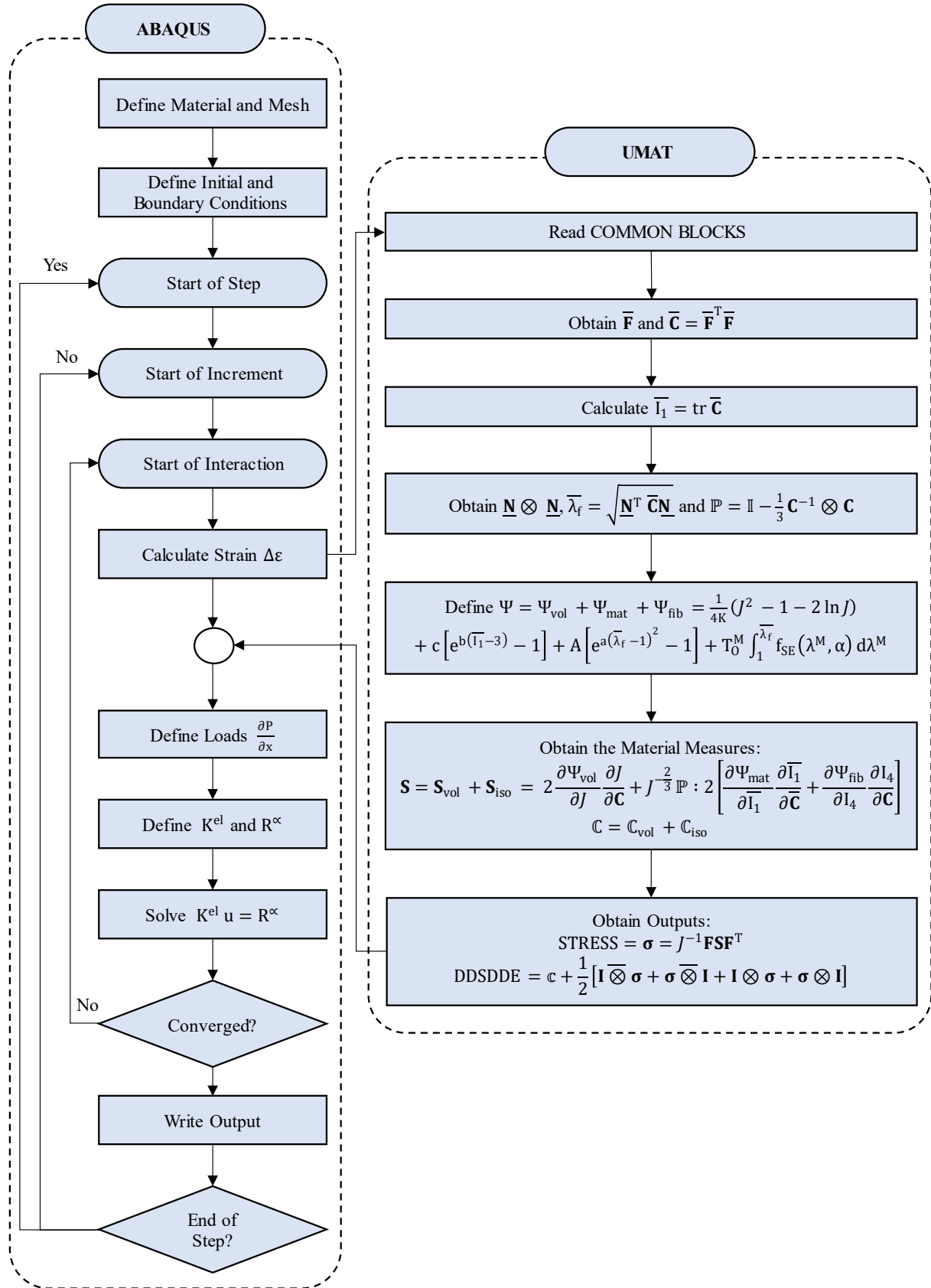
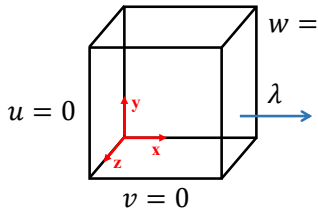
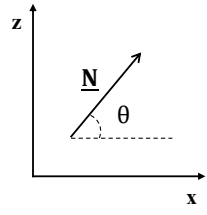
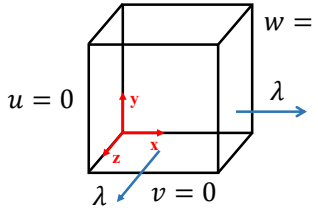
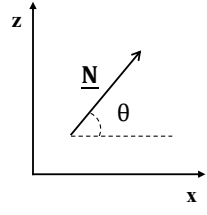
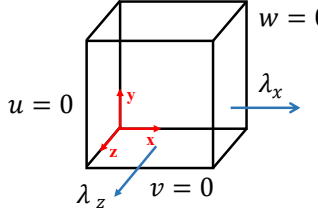
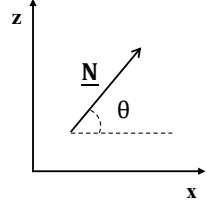
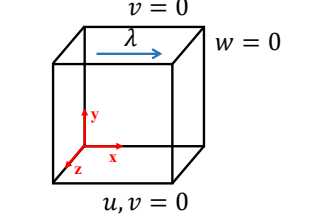
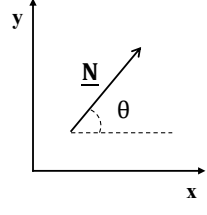


Figure 5.2. ABAQUS flowchart and link to the UMAT subroutine for the Martins constitutive model.

5.4.1 UMAT Validation for the Passive Behavior

The UMAT's validation for the passive behavior of an incompressible transversely isotropic material was performed based on the comparison between the analytical solution, and the solution obtained by the analysis of a C3D8H finite element (single 8-node linear brick hybrid, with constant pressure) in the software ABAQUS. This analysis was developed for the isochoric uniaxial, equibiaxial, biaxial and simple shear deformations. In the Table 5.1, the deformation gradient \mathbf{F} (Holzapfel 2000) and the respective deformation and boundary conditions in an unitary cube are presented for each of the cases. The boundary conditions for the uniaxial, equibiaxial and biaxial deformations set null nodal displacements according to the conditions: $u(x = 0, y, z) = 0$, $v(x, y = 0, z) = 0$ and $w(x, y, z = 0) = 0$. For the simple shear deformation, the boundary conditions are set in the nodes as: $u(x, y = 0, z) = 0$, $v(x, y = 1, z) = 0$ and $w(x, y, z = 0) = 0$.

Table 5.1. Deformation gradient, respective deformation and direction of a family of fibers in the unitary undeformed cube for the uniaxial, equibiaxial, biaxial and simple shear stress states.

Stress State	Deformation Gradient \mathbf{F}	Unitary Undeformed Cube	Undeformed Fiber's Direction $\underline{\mathbf{N}}$
Uniaxial	$\begin{bmatrix} \lambda & 0 & 0 \\ 0 & \frac{1}{\sqrt{\lambda}} & 0 \\ 0 & 0 & \frac{1}{\sqrt{\lambda}} \end{bmatrix}$		 $\underline{\mathbf{N}} = \begin{Bmatrix} \cos \theta \\ 0 \\ \sin \theta \end{Bmatrix}$
Equibiaxial	$\begin{bmatrix} \lambda & 0 & 0 \\ 0 & \frac{1}{\lambda^2} & 0 \\ 0 & 0 & \lambda \end{bmatrix}$		 $\underline{\mathbf{N}} = \begin{Bmatrix} \cos \theta \\ 0 \\ \sin \theta \end{Bmatrix}$
Biaxial	$\begin{bmatrix} \lambda_x & 0 & 0 \\ 0 & \frac{1}{(\lambda_x \lambda_z)} & 0 \\ 0 & 0 & \lambda_z \end{bmatrix}$		 $\underline{\mathbf{N}} = \begin{Bmatrix} \cos \theta \\ 0 \\ \sin \theta \end{Bmatrix}$
Simple Shear	$\begin{bmatrix} 1 & \lambda & 0 \\ 0 & 1 & 0 \\ 0 & 0 & 1 \end{bmatrix}$		 $\underline{\mathbf{N}} = \begin{Bmatrix} \cos \theta \\ \sin \theta \\ 0 \end{Bmatrix}$

A family of fibers is considered in the unitary cube. The undeformed direction of the fibers $\underline{\mathbf{N}}$ is defined by an orientation angle θ positively defined in the Oxz plane for the uniaxial, equibiaxial and biaxial deformations and in the Oxy plane for the simple shear deformation – Table 5.1. To verify the evolution of the Cauchy stress with different orientations of the fibers, two sets of angles θ were defined: $\{0^\circ, 90^\circ\}$ for the uniaxial deformation and $\{0^\circ, 30^\circ, 45^\circ, 60^\circ, 90^\circ\}$ for the others.

To establish the comparison between the analytical and numerical results, a test material was used with the passive properties of the Table 5.2.

Table 5.2. Material parameters selected for validation of the passive behavior with the mechanical properties defined in the UMAT subroutine.

Material Parameters	c (MPa)	b	A (MPa)	a
Values	1.0	0.1	1000.0	0.01

The incompressible restraint in the ABAQUS unitary cube was ensured by setting a high value for the bulk modulus κ . For the uniaxial stress state, a bulk modulus of 1E6 MPa was required to maintain a unitary Jacobian determinant, while in the other cases $\kappa = 1000$ MPa was sufficient. In the analytical formulation, the Lagrange multiplier method was used with the strain energy function of the Equation (5.28).

$$\Psi = c \left\{ e^{b(\bar{I}_1 - 3)} - 1 \right\} + A \left[e^{a(\bar{\lambda}_r - 1)^2} - 1 \right] - p(J - 1) \quad (5.28)$$

The undeformed and deformed configurations for each of the load cases is present in the Figure 5.3.

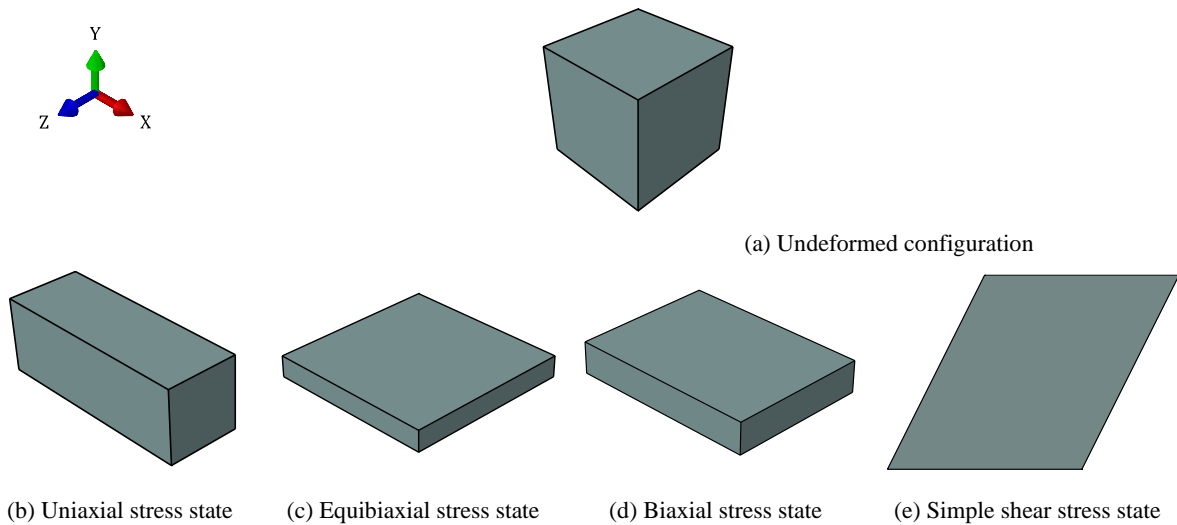


Figure 5.3. Geometrical configuration of the unitary cube subjected to different load cases.

The evolution of the Cauchy stress, in the directions xx (σ_{xx}), zz (σ_{zz}) and xy (σ_{xy}) (depending on the deformation case), with the applied stretch shows agreement between the analytical and the finite element solution (obtained with the material defined by the UMAT subroutine). The results drawn in the Figure 5.4, Figure 5.5, Figure 5.6 and Figure 5.7 allow the validation of the UMAT subroutine for the passive behavior.

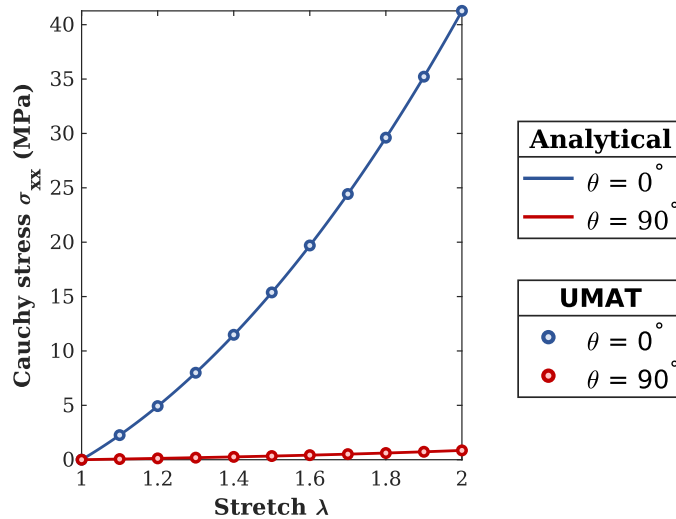


Figure 5.4. Cauchy stress as a function of stretch for a C3D8H finite element with a family of fibers aligned along the directions 0° or 90° subjected to a uniaxial deformation.

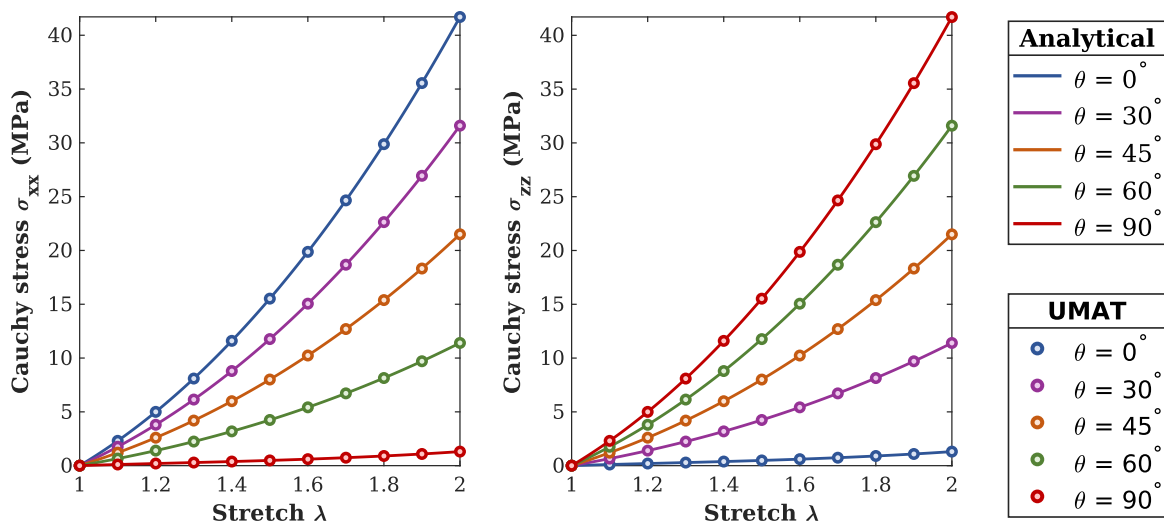


Figure 5.5. Cauchy stress as a function of stretch for a C3D8H finite element with a family of fibers aligned along the directions 0° , 30° , 45° , 60° or 90° subjected to an equibiaxial deformation.

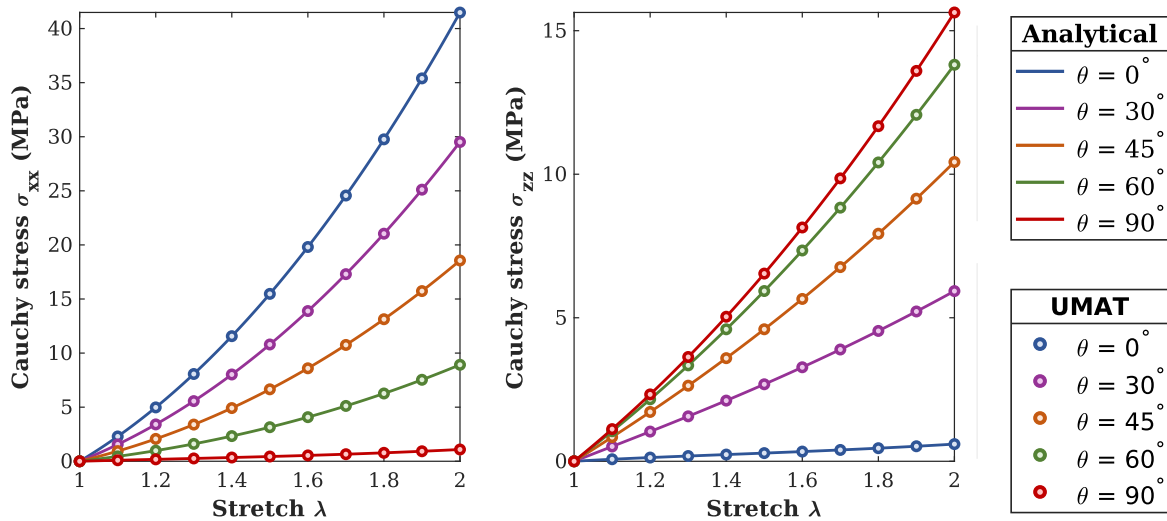


Figure 5.6. Cauchy stress as a function of stretch (λ_x) for a C3D8H finite element with a family of fibers aligned along the directions 0° , 30° , 45° , 60° or 90° subjected to a biaxial deformation with $\lambda_z = \lambda_{x_{\min}} + \frac{\lambda_x - \lambda_{x_{\min}}}{2}$.

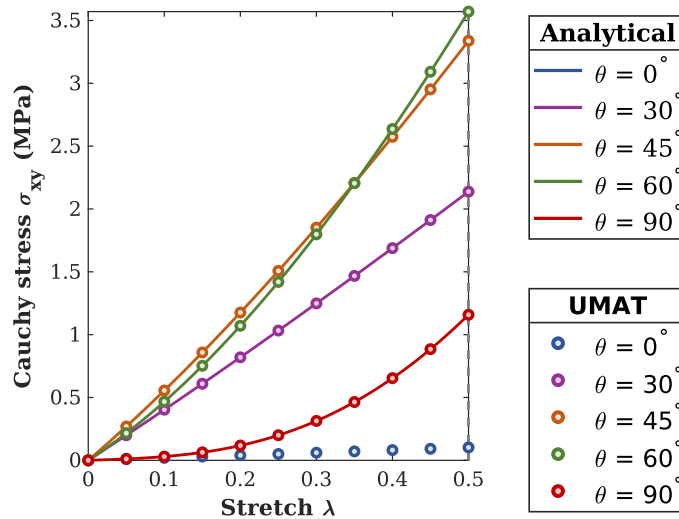


Figure 5.7. Cauchy stress as a function of stretch for a C3D8H finite element with a family of fibers aligned along the directions 0° , 30° , 45° , 60° or 90° subjected to simple shear.

5.4.2 UMAT Validation for the Active Behavior

To validate the results obtained by the UMAT for the active behavior of an isometric contraction, a literature example was used (Martins et al. 2006). This example consists of a square membrane of 10 mm with a thickness of 1 mm, discretized by 14x14 C3D8 elements, with its fibers aligned in the direction xx – Figure 5.8. The square membrane is subjected to null nodal displacements, along the directions xx and yy , and to the activation function of the Figure 5.9.

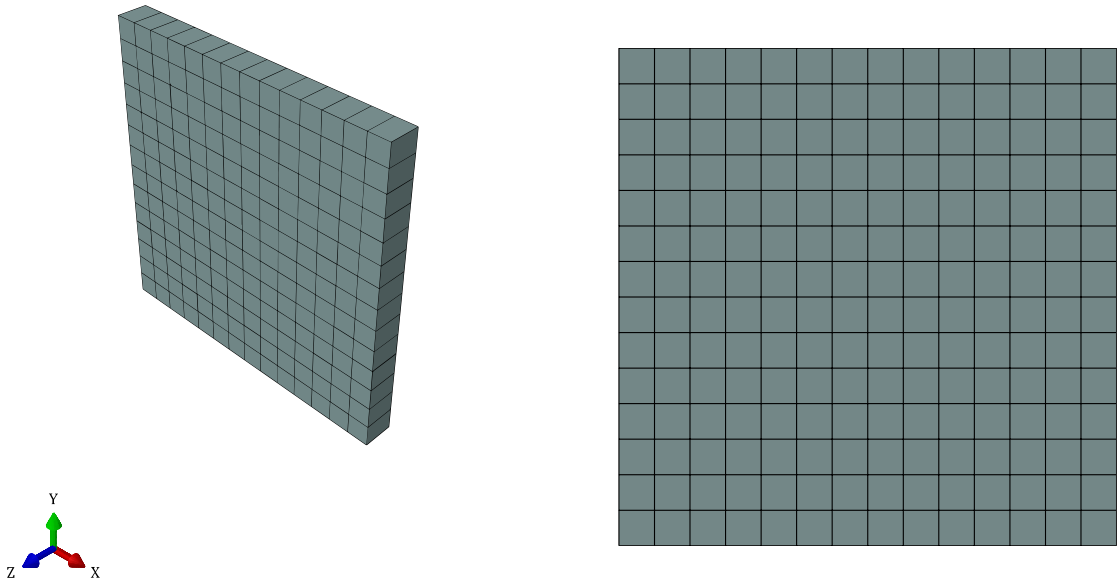


Figure 5.8. Square membrane used for the UMAT validation for active behavior in an isometric contraction (Martins et al. 2006).

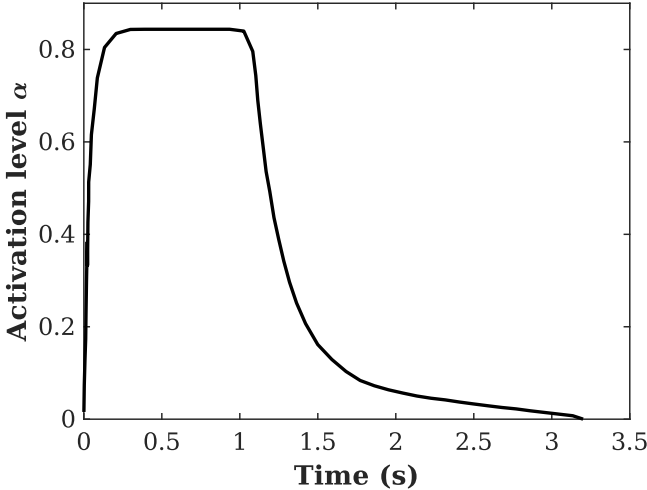


Figure 5.9. Activation function for an isometric contraction (Martins et al. 2006).

The material parameters used in the literature example (Martins et al. 2006) were obtained from (Humphrey and Yin 1987) – Table 5.3.

Table 5.3. Material parameters selected for validation of the active behavior for an isometric contraction with the mechanical properties defined in the UMAT subroutine (Humphrey and Yin 1987).

Material Parameters	κ (MPa)	c (MPa)	b	A (MPa)	a	T_0^M (MPa)
Values	2E7	3.87E-4	23.46	5.84E-4	12.43	0.682

Looking into the results shown in the Figure 5.10, the validation of the UMAT for an isometric contraction is obtained. Moreover, it was possible to see that the evolution of the Cauchy stress along the fiber’s direction follows the shape of the activation function, due to an unchanged length of the membrane (Martins et al. 2006).

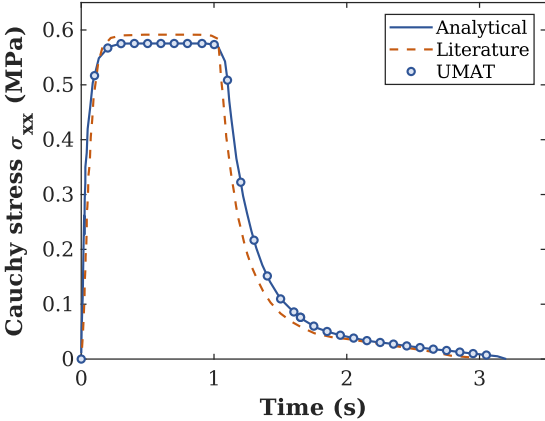


Figure 5.10. Cauchy stress along the direction xx (σ_{xx}) as a function of time in the membrane subjected to an isometric contraction (Martins et al. 2006).

CHAPTER 6

EXPERIMENTAL TENSILE TESTS OF THE SMALL INTESTINE

The mechanical properties of the small intestine's passive behavior were obtained during uniaxial tensile tests of the porcine duodenum and ileum, both along the circumferential (transverse) and longitudinal directions. The porcine small intestine was chosen for the analysis as it closely resembles the human intestine (Hoeg et al. 2000). In an adult porcine, the small intestine's length ranges between 16 and 21 m, where 0.70 to 0.95 cm corresponds to the duodenum, 14 to 19 m to the jejunum and 0.70 to 1 m to the ileum (Masri et al. 2015). The results were compared with similar tests reported in the literature. By doing a statistical evaluation of the obtained results, it was possible to access the resemblance/disparity between mechanical properties and geometric dimensions (thickness) of the two sections/directions analyzed. A nonlinear least square fitting was used to find the passive constitutive parameters for the Martins model in the duodenum and ileum.

6.1 Experimental Procedure

6.1.1 Sample Preparation

The small intestine of a female porcine was cleaned with running water after harvest and, then, frozen for latter uniaxial testing. The unfreezing procedure was carried out during a 24-hour-period in a Styrofoam box placed in a fresh environment to preserve the tissue's integrity and mechanical properties.

During the specimens' preparation, localized zones of the tissue were found perforated or with ice burns resultant from the cleaning and freezing processes. These areas were considered unsuited for testing – Figure 6.1-a. Hence, extreme caution was paid while cutting 20 cm length portions of the tube to avoid these areas – Figure 6.1-b. In total, 6 tubular sections were cut: 4 from the initial portion of the intestine (duodenum) and 2 from its ending portion (ileum).



Figure 6.1. Small intestine tubular section (b) with the ice burned parts discarded (a).

The tube was opened in the longitudinal direction with scissors and residual stresses were observed in the intestine – Figure 6.2. These can be identified by an undulation at the rectangular borders of the tissue section.

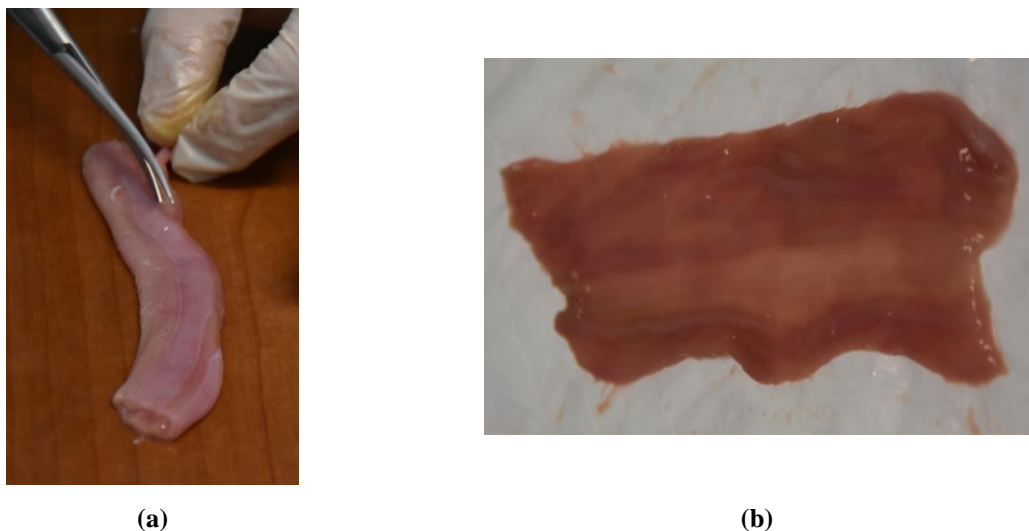


Figure 6.2. Small intestine tube cut along the longitudinal (a) and straightened (b). The undulated edges in the straightened rectangular section are visible in (b).

After being straightened, each rectangular portion was sectioned into 6 specimens: 3 along the longitudinal direction (L) and 3 along the transversal direction (T) (which corresponds to the circumferential direction of the small intestine's tube) – Figure 6.3-a. A vertical technique for cutting the samples with the bistoury was used to reduce the tissue deformation (Ciarletta et al. 2009) – Figure 6.3-b. The specimens were prepared to ensure that the central region would be located away from the edges, so that they could be generally assumed as homogeneous (Ciarletta et al. 2009). Once the cutting procedure was finished, the specimens were placed in towels, hydrated with physiological serum (to avoid dehydration), and saved into labeled containers.

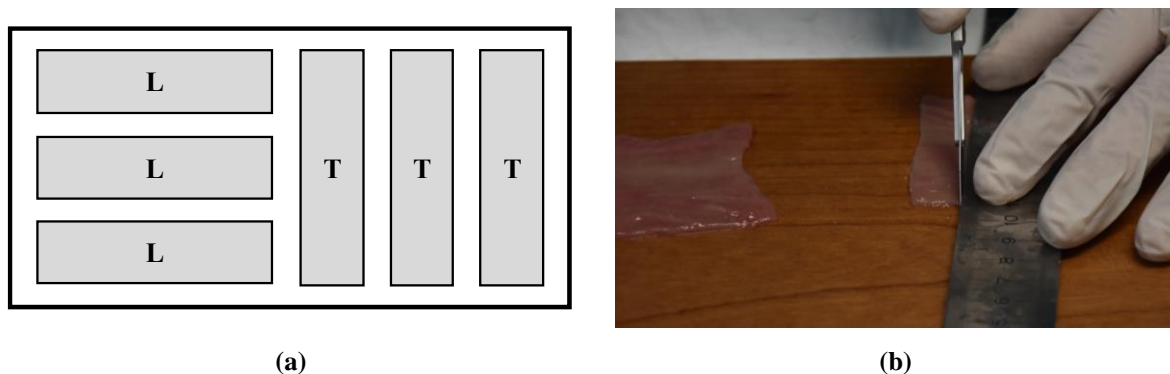


Figure 6.3. Specimens' configuration in the rectangular section (a) and cutting procedure (b).

6.1.2 Uniaxial Tensile Tests

The experimental setup for the uniaxial test was set. A load cell Mecmesin 100 N with 0.02 N of resolution was placed in the upper movable crosshead of a Multitest 2.5 machine to measure the applied force. This was connected to the software Vector Pro 2.1.0.0 used for data recording. A video camera was adjusted to be parallel to the setup, which allowed the measurement of the specimens' width and length between clamps.

The specimens were fixed in the machine with the help of tweezers. First, the sample was fixed in the upper clamp, and then in the lower clamp – Figure 6.4-a. Once the clamps enclosed the specimen, no adjustments could be performed. So, this process was executed with extreme attention to avoid tissue superposition and the specimen's detachment from the machine.

The crosshead was regulated until a small pre-load of 0.04 N. At this point, the displacement was considered null and the thickness of the specimen was measured (3 measurements) with a caliper. The uniaxial test was performed at a velocity of 10 mm/min until the specimen's rupture – Figure 6.4-b.

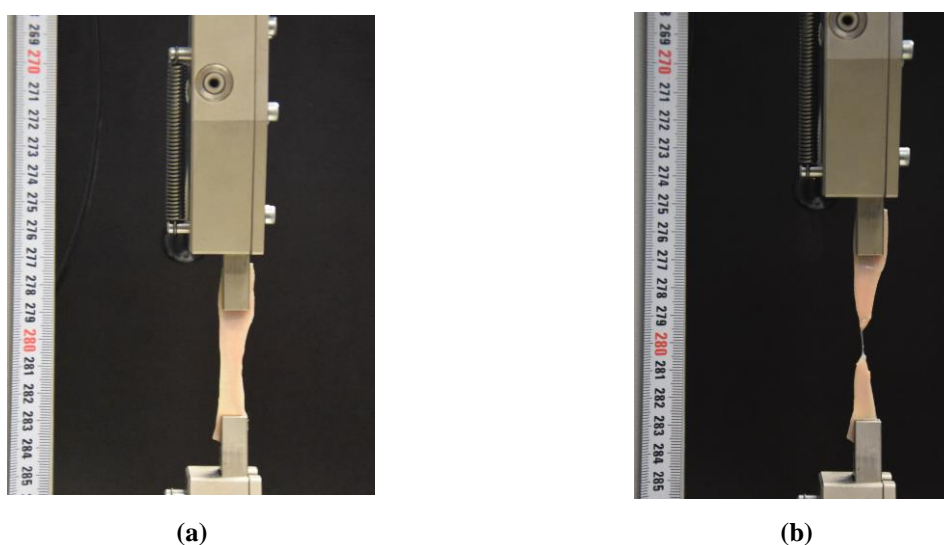


Figure 6.4. Fixation of the sample in the testing machine: initial (a) and deformed configurations (b).

6.2 Results

For a simpler analysis of the results, each specimen was given a code: DX_1LX_2 or ILX_2 for the duodenum D or ileum I samples cut in the longitudinal direction L, and DX_1TX_2 or ITX_2 for the duodenum D or ileum I samples cut in the transverse direction T. The index X_1 represents the proximity of the duodenum samples to the stomach ($X_1 = 1$ is closer to the stomach than $X_1 = 2$) and the index X_2 represents the sample number.

Firstly, the specimens' initial thickness t_0 , width w_0 and length between clamps l_0 is presented. Then, the results are plotted with the first Piola-Kirchhoff stress P (which represents the force per unit area of the reference configuration, as indicated in the Section 4.3) as a function of the stretch λ . This is obtained by converting the displacement Δy versus force f results – Equations (6.1) and (6.2).

$$\lambda = \frac{l}{l_0} = \frac{l_0 + \Delta y}{l_0} \quad (6.1)$$

$$P = \frac{f}{w_0 t_0} \quad (6.2)$$

6.2.1 Duodenum

The Table 6.1 and Table 6.2 show the geometrical parameters (thickness, width and length) of the porcine duodenum specimens.

Table 6.1. Geometrical parameters for the porcine duodenum samples D1 (values in mm).

D1	L1	L2	L3	L4	L5	L6	T1	T2	T3	T4	T5
t_0	1.50	1.66	1.70	2.38	1.56	1.74	2.23	1.73	2.16	1.42	1.74
w_0	12.00	12.67	11.67	12.67	12.67	11.00	14.00	13.33	12.33	12.00	12.67
l_0	34	57	39	63	38	44	33	36	49	48	54

Table 6.2. Geometrical parameters for the porcine duodenum samples D2 (values in mm).

D2	L1	L2	L3	L4	L5	L6	T1	T2	T3	T4	T5	T6
t_0	1.24	1.39	1.04	1.44	1.21	1.32	1.72	1.60	1.33	1.84	1.57	1.58
w_0	9.00	12.67	9.33	8.67	10.00	9.67	8.67	10.33	9.00	11.67	12.00	11.33
l_0	56	43	39	40	46	39	41	42	42	35	41	47

In the Figure 6.5, the first Piola-Kirchhoff stresses P_{11} (obtained from tensile tests of the longitudinal samples) and P_{22} (obtained from tensile tests of the transverse samples) are plotted against the stretch for each sample. For the matter of this report, only the elastic regime was considered. For modelling purposes, the data (Figure 6.5-a and Figure 6.5-b) was limited to a maximum stretch of 1.2 in the longitudinal direction and to a maximum of 1.4 in the transverse direction – Figure 6.5-c and

Figure 6.5-d. This consideration was taken since damage evaluation is out of the scope of this work. This strain limitation ensures that the tested samples would not likely endure damage within this range (Ciarletta et al. 2009). Lastly, the average curve for each direction was represented in the Figure 6.5-c and Figure 6.5-d.

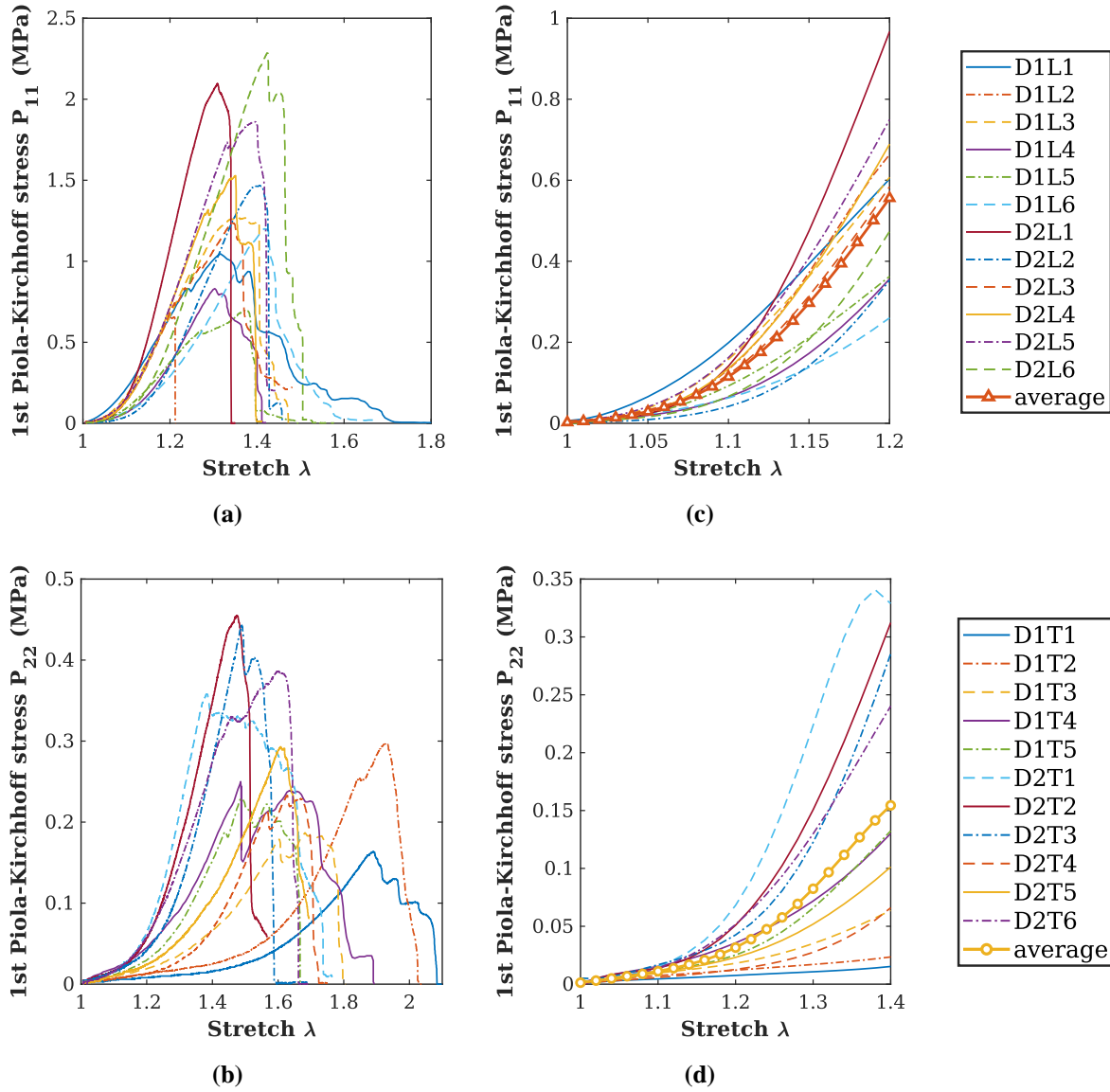


Figure 6.5. Stress-stretch data for the porcine duodenum in the longitudinal (a, c) and transverse directions (b, d). In (c) and (d), the curves were limited by an upper stretch to avoid mechanical damage and the average curves were drawn.

6.2.2 Ileum

The Table 6.3 shows the initial geometrical parameters of the tested specimens of the porcine ileum.

Table 6.3. Geometrical parameters for the porcine ileum samples (values in mm).

I	L1	L2	L3	L4	L5	T1	T2	T3	T4	T5	T6
t_0	0.90	0.68	1.07	0.78	0.80	0.81	0.76	1.02	0.96	0.93	0.84
w_0	8.00	8.67	8.33	8.00	9.33	9.00	9.67	9.00	7.67	10.67	10.00
l_0	40	49	37	59	40	49	49	49	50	46	50

In the Figure 6.6, the curves stretch versus first Piola-Kirchhoff stresses P_{11} and P_{22} are presented for the ileum portion. Once more, these curves were limited by a maximum stretch of 1.2 in the longitudinal direction and to a maximum of 1.4 in the transverse direction. In the Figure 6.6-c and Figure 6.6-d, the averaged curves were plotted.

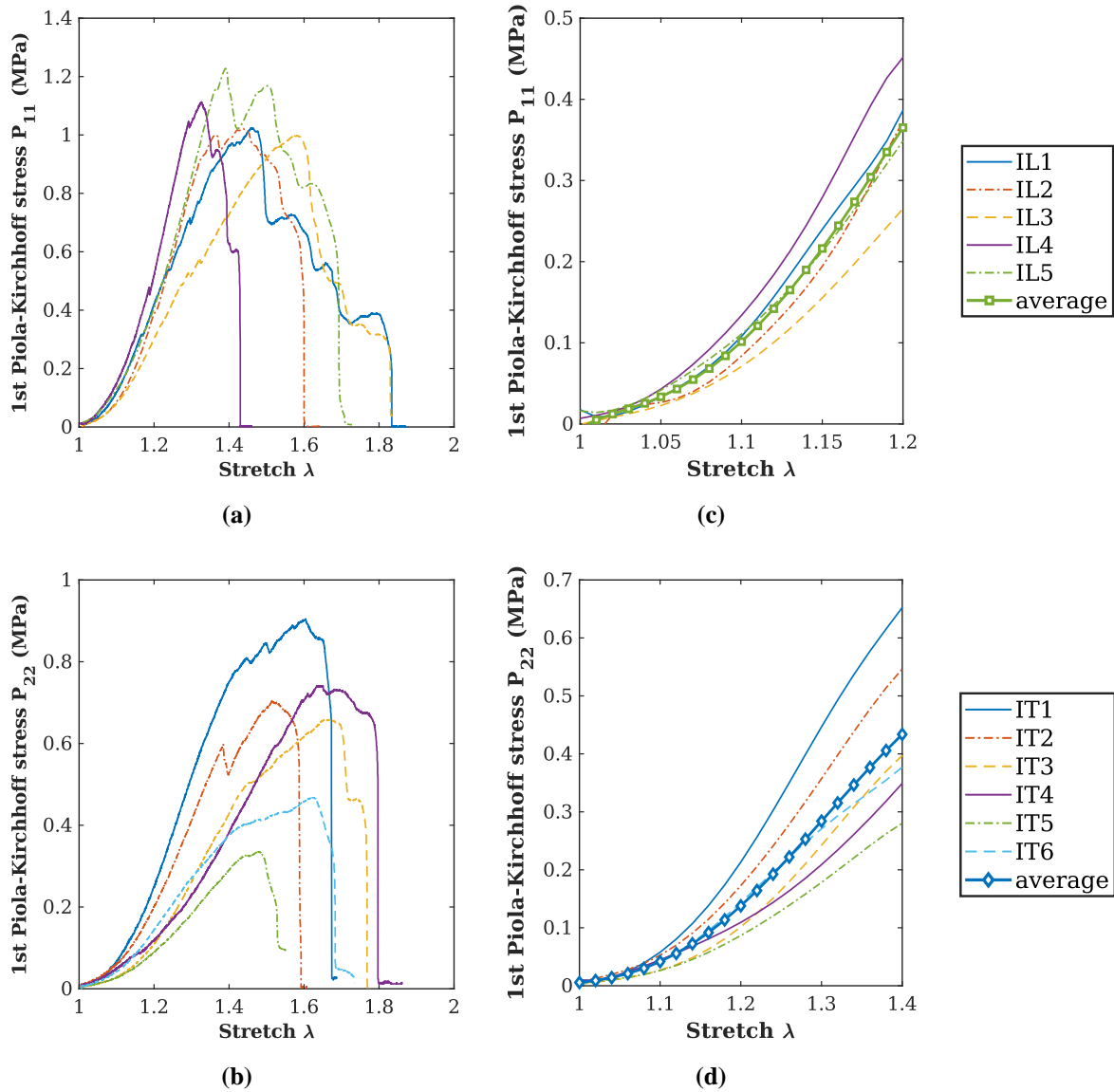


Figure 6.6. Stress-stretch data for the porcine ileum in the longitudinal (a, c) and transverse directions (b, d). In (c) and (d), the curves were limited by an upper stretch to avoid mechanical damage and the average curves were drawn.

6.3 Statistical Analysis

For the statistical analysis, t-tests for samples with different sizes were performed to compare the thickness and mechanical properties in the duodenum and ileum, as well as the mechanical properties in the longitudinal and transverse directions.

Departing from a null hypothesis of equality of the evaluated parameter's mean in the two independent samples and an alternative hypothesis of having different means, the t-test can be applied for different ($\text{var}_x > 2\text{var}_y$ or $\text{var}_y > 2\text{var}_x$) or similar ($0.5 < \text{var}_x/\text{var}_y < 2$) variances. A p-value lower than 0.05 was considered an indicator of statistically significant difference.

6.3.1 Thickness

From the t-test for different sample sizes and different variances with the null hypothesis of equal thicknesses between the duodenum and ileum, it was possible to conclude that the thickness between portions is indeed different – Table 6.4 and Figure 6.7.

Table 6.4. Mean thickness and respective standard deviations for the duodenum and ileum.

	$t_0 \pm \text{SDV (mm)}$	Number of Specimens
Duodenum	1.61 ± 0.32	23
Ileum	0.87 ± 0.12	11

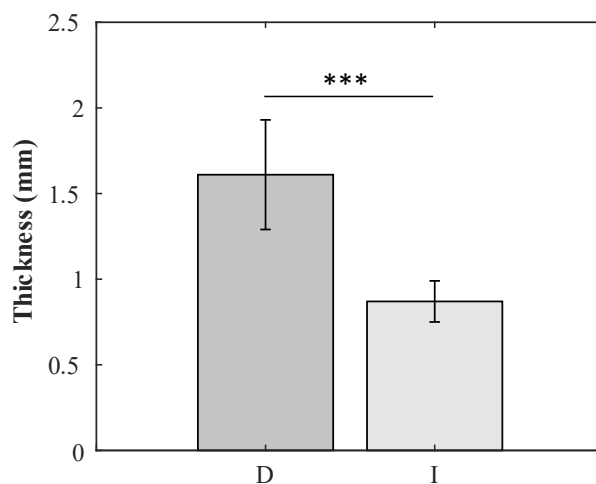


Figure 6.7. Bar plot indicating the statistically significant difference between the duodenum and ileum thicknesses ($p^{***} < 0.0005$).

6.3.2 First Piola-Kirchhoff Stress

In the Figure 6.8, the average first Piola-Kirchhoff stress versus stretch curves and respective standard deviations for the longitudinal and transverse directions in the duodenum and ileum are plotted.

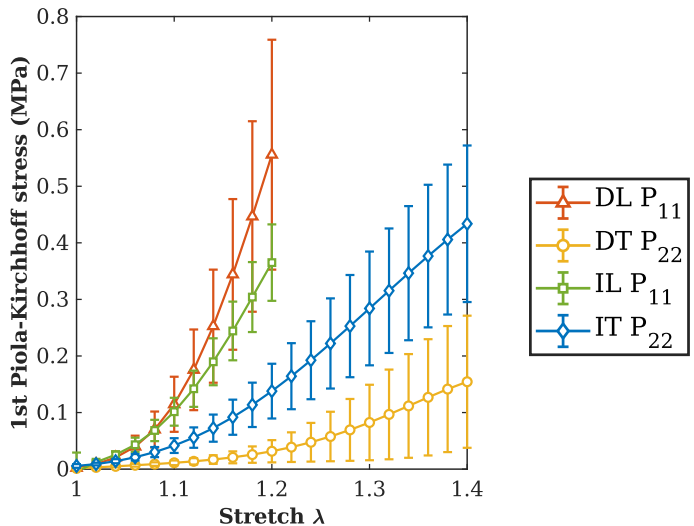


Figure 6.8. Averaged stress-stretch curves for the porcine duodenum and ileum in the longitudinal and transverse directions with respective standard deviations.

As a way to compare the mechanical properties of the small intestine, each sample’s curve was fitted to a bilinear regression (with slopes $E1$ and $E2$) and the comparison was performed based on the slope of each of the lines. The point I , separating the bilinear regimes, corresponds to the point where the local slope is 50% of the maximum – Figure 6.9.

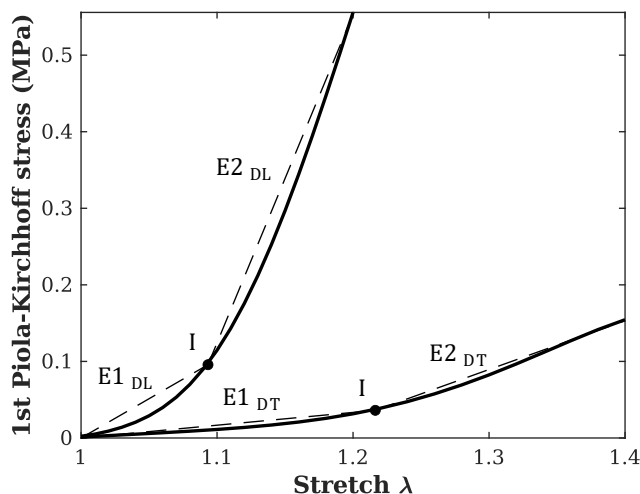


Figure 6.9. Bilinear regression of the stress-stretch curves with the slopes $E1$ and $E2$.

The t-tests were performed to compare the E1 and E2 slopes to determine if either different directions of the small intestine (longitudinal and transverse) or different portions of the small intestine (duodenum and ileum) had equal or non-equal properties. The results are drawn in the Figure 6.10 and the statistically difference was represented by * ($p < 0.05$), ** ($p < 0.005$) or *** ($p < 0.0005$).

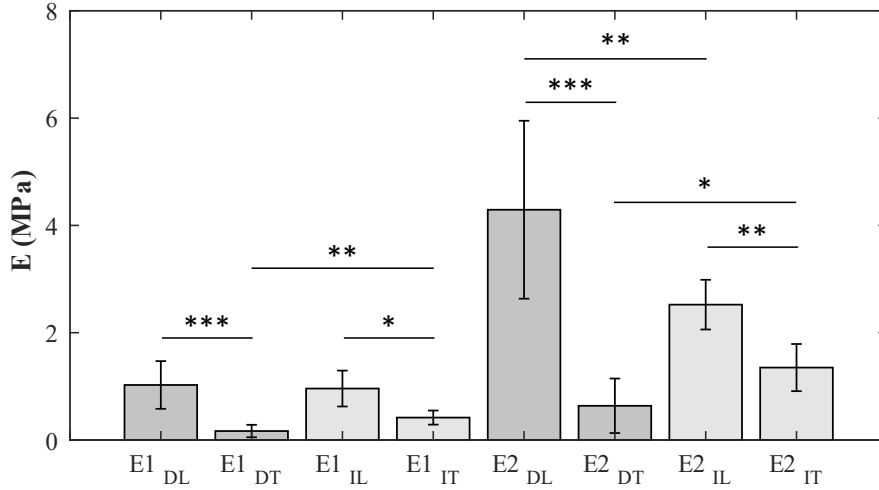


Figure 6.10. Bar plot indicating the statistically significant difference between the longitudinal and transverse directions and between the duodenum and ileum for the slopes E1 and E2 ($p^* < 0.05$, $p^{**} < 0.005$, $p^{***} < 0.0005$).

6.4 Passive Properties of the Small Intestine

To derive the parameters of the material model (Martins model) from the experimental data, the first Piola-Kirchhoff, along the longitudinal and transverse directions, was obtained by the Equation (6.3), where $\bar{\lambda}_{f_1}$ and $\bar{\lambda}_{f_c}$ are the fibers' stretch along the non-deformed directions $\underline{\mathbf{N}}_1 = [1 \ 0 \ 0]^T$ (longitudinal muscle layer) and $\underline{\mathbf{N}}_c = [0 \ 1 \ 0]^T$ (circular muscle layer).

$$\mathbf{P} = \mathbf{F} \frac{\partial \Psi_{\text{vol}}}{\partial J} \frac{\partial J}{\partial \mathbf{E}} + \mathbf{F} \frac{\partial \Psi_{\text{mat}}}{\partial \bar{I}_1} \frac{\partial \bar{I}_1}{\partial \mathbf{E}} + \mathbf{F} \frac{\partial \Psi_{\text{fib}}}{\partial \bar{\lambda}_{f_1}} \frac{\partial \bar{\lambda}_{f_1}}{\partial \mathbf{E}} + \mathbf{F} \frac{\partial \Psi_{\text{fib}}}{\partial \bar{\lambda}_{f_c}} \frac{\partial \bar{\lambda}_{f_c}}{\partial \mathbf{E}} \quad (6.3)$$

For the interpolation of the results, the nonlinear least square method was used and the root mean-squared error RMSE was gathered to validate the model's accuracy (Ciarletta et al. 2009).

6.4.1 Duodenum

The experimental results were fitted by the average stretch versus first Piola-Kirchhoff curves of the uniaxial test in the material described by the Martins model. The fitted parameters are presented in the Table 6.5. The quality of the fit is characterized by a RSME close to 0, which is attained as $\text{RMSE}_{\text{max}} = 0.0261$ – Figure 6.11.

Table 6.5. Fitted values for the constitutive parameters of the Martins Model for uniaxial traction in the porcine duodenum.

Parameters	c (kPa)	b	A_{LM} (kPa)	a_{LM}	A_{CM} (kPa)	a_{CM}
Fitted values	1.000	0.500	30.692	20.000	10.099	6.818

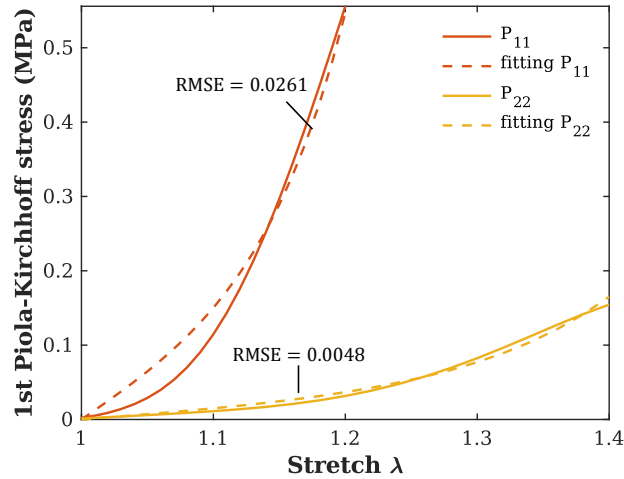


Figure 6.11. Fitting comparison of the first Piola-Kirchhoff stress for the uniaxial tests in the longitudinal and circumferential directions in the porcine duodenum.

6.4.2 Ileum

The constitutive parameters obtained for the ileum are displayed in the Table 6.6. The model’s accuracy is validated by $RMSE_{max} = 0.0160$ – Figure 6.12.

Table 6.6. Fitted values for the constitutive parameters of the Martins Model for uniaxial traction in the porcine ileum.

Parameters	c (kPa)	b	A_{LM} (kPa)	a_{LM}	A_{CM} (kPa)	a_{CM}
Fitted values	1.000	0.505	22.638	19.418	79.880	3.873

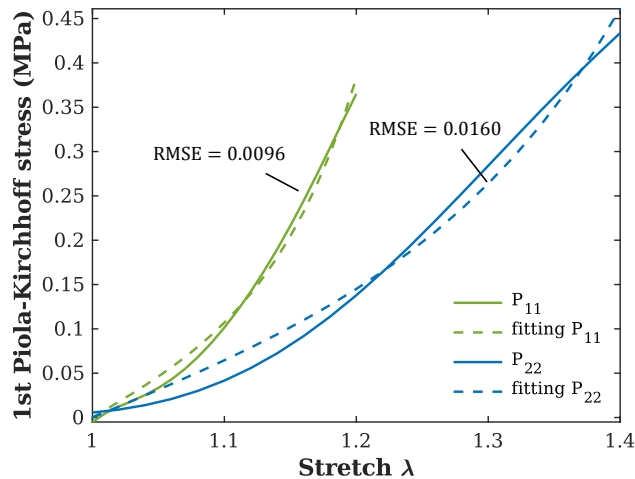


Figure 6.12. Fitting comparison of the first Piola-Kirchhoff stress for the uniaxial tests in the longitudinal and circumferential directions in the porcine ileum.

6.5 Discussion

The small intestine's thickness has been reported to decrease in the distal direction in rats (Dou et al. 2003). The same tendency was found in the human small intestine, where the wall's thickness of several healthy patients was measured via ultrasound. In the latter study, it was observed that the wall's thickness in the duodenum was greater, with mean and standard deviation values of 1.6 ± 0.3 mm, contrasting with $0.9 - 1.2 \pm 0.3$ mm, obtained from the jejunum until the sigmoid colon (Nylund et al. 2012).

In the present study, the wall's thickness was also found dependent on the axial direction, as the average thickness was different in the duodenum and ileum ($p < 0.0005$). The obtained mean thickness and standard deviations of 1.61 ± 0.32 mm in the duodenum and of 0.87 ± 0.16 mm in the ileum are close to the findings of Nylund et al. (2012). The decrescent thickness along the tract was initially felt to the touch during the cutting process and it became a major issue while fixing the specimens in the tensile machine. This happened because the ileum specimens were significantly thinner. Even though it was paid extreme caution to maintain the specimens hydrated, it is important to bear in mind that some dehydration may have influenced the thickness measurements. The ileum specimens might have been the most affected by this since they were the last to be tested. This problem could have been solved if a measurement of the thickness had also been performed during the sample preparation/cutting. This would result in a more accurate average of the wall's thickness. Additionally, it would also allow the removal of dehydrated specimens from the analysis by comparing both measured thicknesses.

In uniaxial tensile tests performed in the human small intestine by Egorov et al. (2002), the mechanical properties have been reported to vary with the circumferential and longitudinal directions, the latter being the stiffer. In the rat's small intestine, the longitudinal direction was also found stiffer than the circumferential (Dou et al. 2003). However, in biaxial tests performed in the porcine small intestine in the work of Bellini et al. (2011), this difference was not consistent, as some samples presented a stiffer longitudinal direction while others presented a stiffer circumferential direction.

The obtained experimental results for the uniaxial tests on the small porcine of the Figure 6.8 show that the longitudinal direction is stiffer than the circumferential in both tested sections. However, the specimens' rupture was, in average, most likely to occur at a lower stretch level in the longitudinal direction. The statistical t-test analysis was able to reject the null hypothesis of equality between the tube's directions, which led to the assumption of different mechanical behavior in the longitudinal and circumferential directions.

In the rat's small intestine, a significant axial gradient has also been reported for its mechanical properties. This gradient has been linked to the functions of each portion of the small intestine: the stiffer duodenum is subjected to the gastric emptying, acting as a capacitative resistor; and the ileum acts as a reservoir. The authors have indicated that the reduction of the transit distally may be explained by different chyme's viscosities and by an increasingly compliant wall (Dou et al. 2003).

When comparing the stress-stretch curves obtained in the uniaxial tests between the duodenum and the ileum sections, this differentiation is not as clear as in the previously referred study. Even though they are stiffer than the ileum in the longitudinal direction, the duodenum specimens harvested along the circumferential direction have presented themselves as more compliant. Moreover, looking into the statistical t-test analysis, this has indicated statistically different ($p < 0.05$) slopes E1 and E2 between the duodenum and the ileum, both in the longitudinal and circumferential directions. However, as an exception, this was not the case for the longitudinal direction of the duodenum and ileum for small stretch levels. These findings lead to the conclusion that the small intestine sections under analysis are, in fact, different, so it is justified to perform an individual fitting procedure for the duodenum and ileum stress-stretch curves. Nevertheless, in inflation tests performed in the rat's small intestine by Sokolis (2017), it was found that the mechanical properties of each individual section vary along the axial position. Therefore, the attribution of mechanical properties to the entire duodenum, jejunum and ileum is a mere simplification of the biomechanical behavior of the small intestine.

Even though a thorough methodology was employed for the uniaxial tensile tests analysis, some problems might have affected the obtained results. Thus, it is important to look at these conclusions as the results of an experimental method that could be greatly improved.

In the tensile tests of the porcine large intestine, reported by Ciarletta et al. (2009), a width/thickness ratio near to 10 ensured plane stress state in the sample's center and a mechanical response less receptive to the thickness variation. Yet, in the present work, this was not precisely followed, as ratios between 5 and 13 were accepted to generate the average curves. Additionally, the gripping procedure was dependent on the force generated by the spring controlling the gramps closure. This proved to be a source of stress concentration, which led to the rupture of several specimens near their ends. The latter problem was not as critical as it could be expected, since an analysis localized merely in the elastic regime was employed. To improve the results' accuracy, disposable polymeric holders could have been used to fix the samples in between the clamps, like in the work of Ciarletta et al. (2009).

The analysis of the fitted constitutive parameters (to the Martins model), related to the fibers' behavior, supported the already-mentioned comparison between the duodenum and ileum in the longitudinal and circumferential directions. Moreover, it is possible to see that the fitted matrix stiffness was the same in the duodenum and in the ileum. Comparing the matrix stiffness to the work of Ciarletta et al. (2009) for the large intestine, this was of the same order (1 kPa), though a different strain energy function has been employed.

CHAPTER 7

SIMULATION ON THE ACTIVE CONTRACTION OF SMALL INTESTINE

A biomechanical model of the small intestine was developed to study the chyme's propulsion during a peristaltic event, resultant only from the contraction of the circumferential muscle fibers. Several preliminary cases were analyzed to evaluate the influence of the small intestine's mechanical properties and boundary conditions, the activation method and the propulsive resistance. This allowed the establishment of the model under analysis. Finally, the propulsive capability of the small intestine was compared (i) between the duodenum and the ileum; (ii) between different chyme stiffnesses; and, (iii) between healthy patients and the ones with gastrointestinal limitations, such as SS or ulcers.

7.1 Model

To simulate the chyme's propulsion in the small intestine, a model was developed using the finite element software ABAQUS. In this study, the virtual segment of the small intestine was considered as a quarter of a 100 mm long cylinder with an internal radius of 10 mm and a thickness of 2 mm – Figure 7.1. This geometry is similar to other cylindrical models of the small intestine reported in the works of Bellini et al. (2017) and Sinnott et al. (2017). Even though the small intestine was considered for this analysis with a circumferential profile, its empty lumen may constitute an ellipsoidal transverse configuration (Tobergte and Curtis 2013).

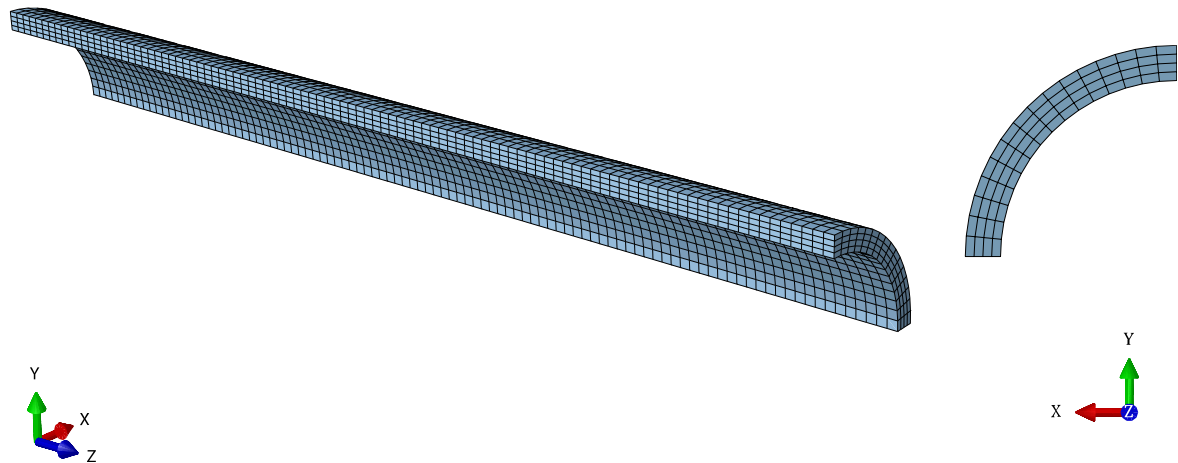


Figure 7.1. Biomechanical model of the small intestine as a quarter of a deformable cylinder.

To ensure the incompressible behavior, the cylinder was meshed by C3D8H finite elements (8-node linear brick hybrid elements with constant pressure) with active degrees of freedom U1, U2 and U3. A structured mesh of 6400 elements was used and this was kept constant throughout the different simulations.

In other works, the chyme has been modelled as a fluid. In the work of Sinnott et al. (2017), the duodenal luminal contents were considered as a stationary Newtonian fluid with the density of water (1000 kg/m^3) and viscosity of 0.01 Pa s . This seems like a reasonable approach, as the chyme consists of a mixture of partially digested food with the gastrointestinal secretions (Sinnott et al. 2017), which ends up granting it a semifluid appearance (Guyton and Hall 2006). However, as this work aims to establish a comparison between the propulsive behavior instead of carefully looking into the flow behavior of the chyme, it was simplified as a spherical body.

For the presented model, two approaches were considered to model the chyme. It was assumed either as an analytical rigid sphere (Figure 7.2-a) or as a quarter of a deformable sphere (Figure 7.2-b) with a radius of 11 mm. The chyme's radius was chosen in such a way that the contact would induce a small distension of the muscle fibers of the small intestine's wall, as the fiber's stretch leads to the initiation of the peristaltic activity (Koeppen and Stanton 2018).

Another model was considered, with axial springs connected from built-in nodes placed along the cylinder's axis to the reference point of the analytical rigid sphere. This intended to represent the chyme's continuity along the tract and the resistance associated with it – Figure 7.2-c.

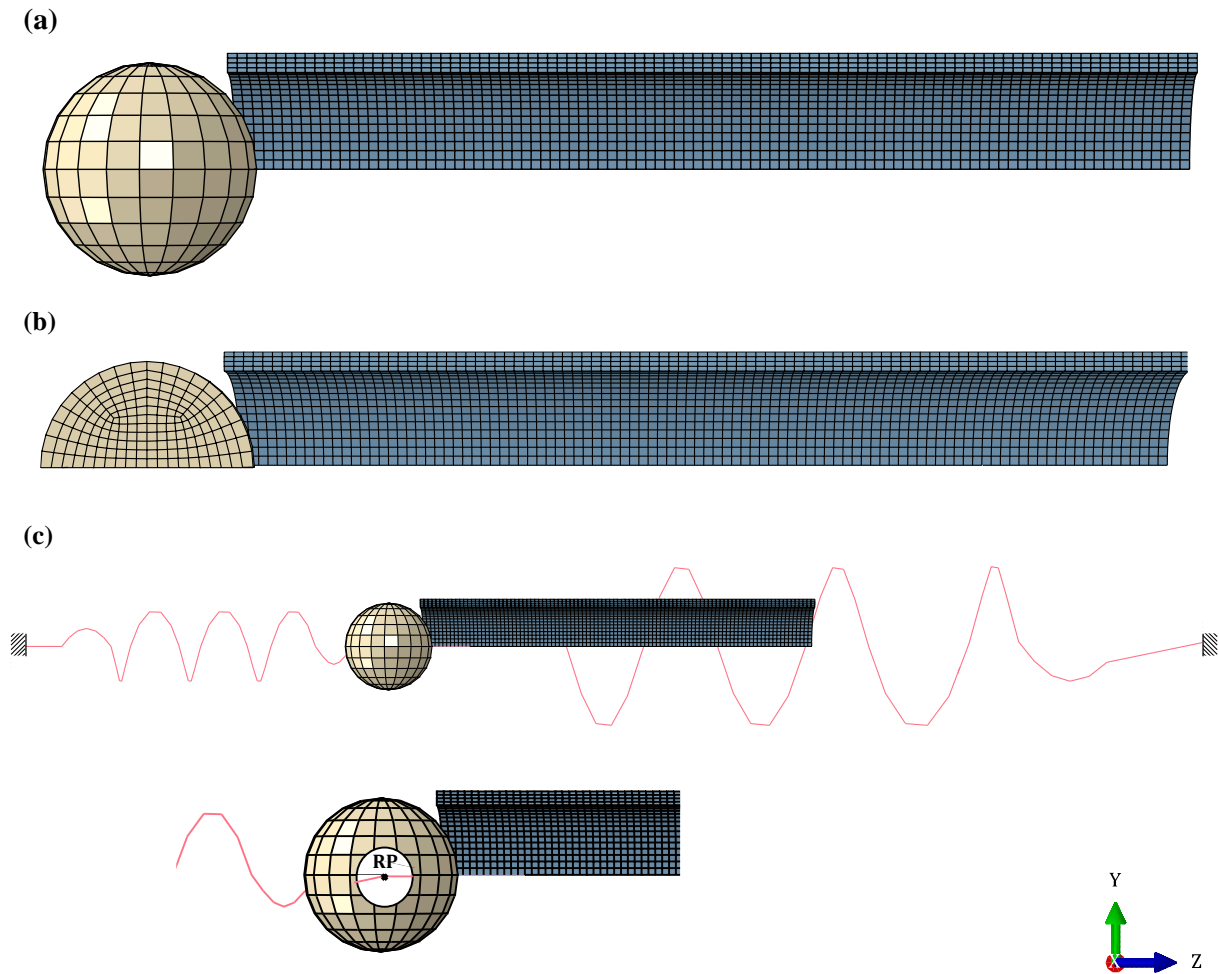


Figure 7.2. Biomechanical model for the chyme propulsion in the small intestine with the chyme modelled as an analytical rigid sphere (a), as a quarter of a deformable sphere (b) and as an analytical rigid sphere connected by springs in its reference point (RP) to built-in points in the axial axis of the cylinder (c).

The model was defined so that the initial contact (discretized by a node to surface approach) between the small intestine (slave surface) and the chyme (master surface) was established by an imposed axial displacement of the chyme. This node to surface approach was used because it tolerates some penetration of the master surface in the slave, but not the opposite way around. Besides this, it also defines the contact direction by the normal to the master surface. For the tracking algorithm, the finite-sliding was used as it allows relative separation, sliding and rotation between the contact surfaces (Smith 2009).

The normal behavior of the contact interaction between the outer surface of the chyme and the inner surface of the small intestine is constrained, for non-penetration of the slave nodes in the master surface, by a penalty method with a hard pressure-overclosure. This tolerates a slight penetration degree with the contact force proportional to the penetration distance, which does not influence the results of the simulation since the stiffness of the small intestine's wall is much smaller than the one considered for the chyme. Additionally, by implementing the penalty method, no Lagrange multipliers are used. So, with this approach, the decreased number of degrees of freedom and the loose in the non-penetration

constrain lead to faster running times of the simulation. Regarding the frictional behavior, a uniform friction coefficient was used and the penalty method was employed as it allows some relative motion between the surfaces.

In the static's steps definition, the geometric nonlinearities were considered by including the large-displacements effect. Moreover, some instabilities were expected to occur in the model due to the contact algorithm, nonlinear behavior of the material and localized increase of the stiffness caused by the contraction of circumferential fibers. These made impossible to obtain a converged solution. To overcome such instabilities, automatic stabilization was included in the expected unstable increments. The automatic stabilization consists of adding artificial viscous forces to the static equilibrium of the Equation (4.122) to reduce the motion resultant from considerable stiffness changes. In the Equation (7.1), the artificial viscous forces are represented by $\zeta \mathbf{M}^* \underline{\mathbf{v}}$ (where ζ is the damping factor, \mathbf{M}^* the artificial mass matrix and $\underline{\mathbf{v}}$ the vector of the nodal velocities).

$$\underline{\mathbf{R}} = \underline{\mathbf{F}}_{\text{ext}} - \underline{\mathbf{F}}_{\text{int}} - \zeta \mathbf{M}^* \underline{\mathbf{v}} \quad (7.1)$$

In this work, a small constant damping factor of 1E-7 Ns/mm was used. Even though the introduction of these artificial viscous forces changes the stiffness matrix of the boundary-value problem, it largely speeds up the obtainment of a converged solution. The introduced error was verified by comparing the stabilization energy (ALLSD) with the total strain energy (ALLIE) of the model, as it is recommended to keep the ALLSD lower than 5% of the ALLIE (Smith 2009).

7.2 Mechanical Properties of the Small Intestine

The incompressible behavior of the small intestine was ensured throughout the simulations by a bulk modulus of 1000 MPa. This was enough to have a unitary Jacobian determinant.

As previously mentioned, the small intestine has two layers of smooth muscle cells, each aligned longitudinally or circumferentially. Since the smooth muscle cells usually have a main contractile direction (Kroon 2009), two families of fibers with passive and active mechanical response were considered along these directions. To represent the model's anisotropy in the UMAT subroutine (Ferreira et al. 2017), previously presented in the Figure 5.2 of the Section 5.4, the fibers' direction in each finite element was determined. A geometrical procedure was carried out to obtain the fibers' orientation by following the longitudinal and circumferential directions of a cylinder – Figure 7.3.

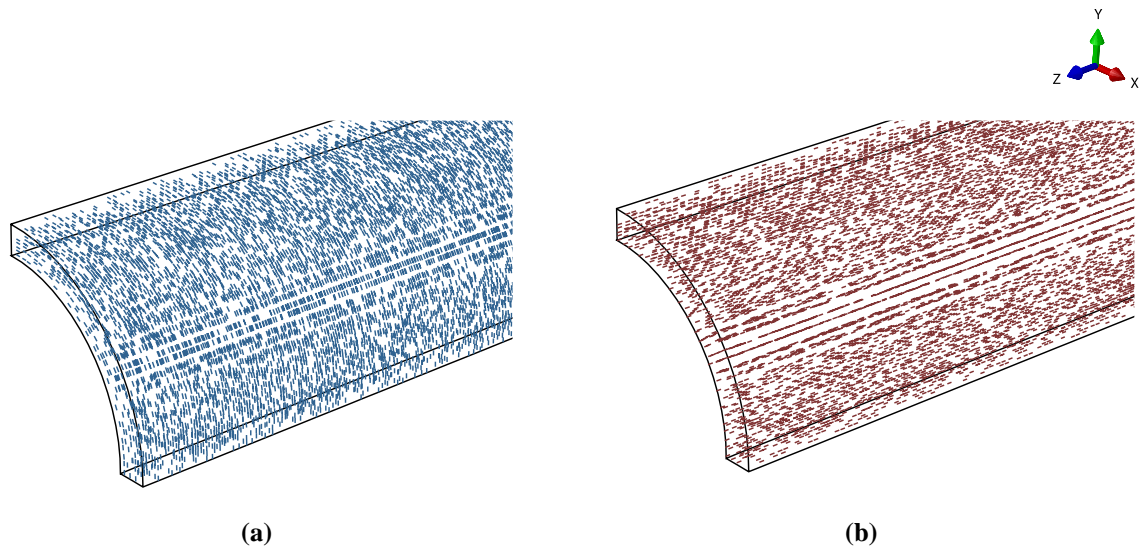


Figure 7.3. Fibers aligned in the circumferential (a) and longitudinal (b) directions.

Considering only the passive behavior of the small intestine, the constitutive parameters ($c, b, A_{CM}, a_{CM}, A_{LM}, a_{LM}$) obtained in the Section 6.4 for the porcine duodenum and ileum were used – Table 6.5 and Table 6.6. For the active properties, these were obtained from force-velocity curves in the work of Gregersen et al. (2007), for both healthy and SS patients. With these considerations, the muscle peak stress was obtained as $T_0^M = 76.2$ kPa, for normal patients, and $T_0^M = 31.7$ kPa, for SS patients.

To test the influence of an ulcer and its size in the chyme’s propulsion, two different ulcers with 5 and 10 mm were considered in the inner surface of the small intestine– Figure 7.4. In the biomechanical models, these elements were set without contractile activity – $\alpha = 0$.

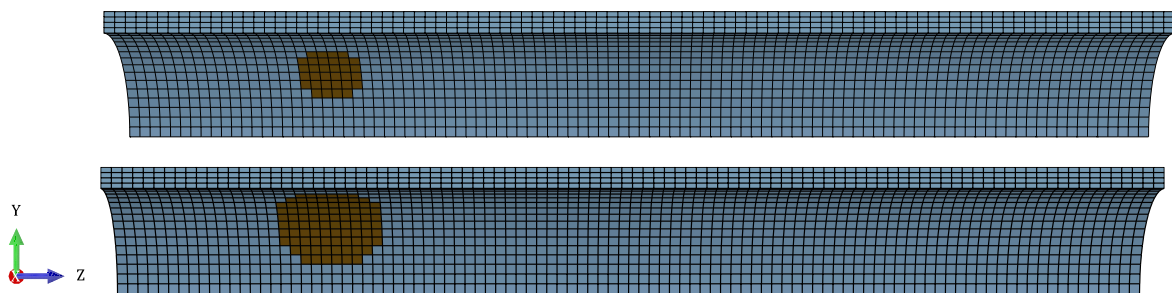


Figure 7.4. Small intestine ulcers with 5 (top) and 10 mm (bottom) in the inner surface.

The direction of the fibers and the ulcer elements (elements not activated) were read in the beginning of the analysis in an UEXTERNALDB subroutine and passed into the UMAT as a COMMON BLOCK variable (Smith 2009) – Figure 7.5.

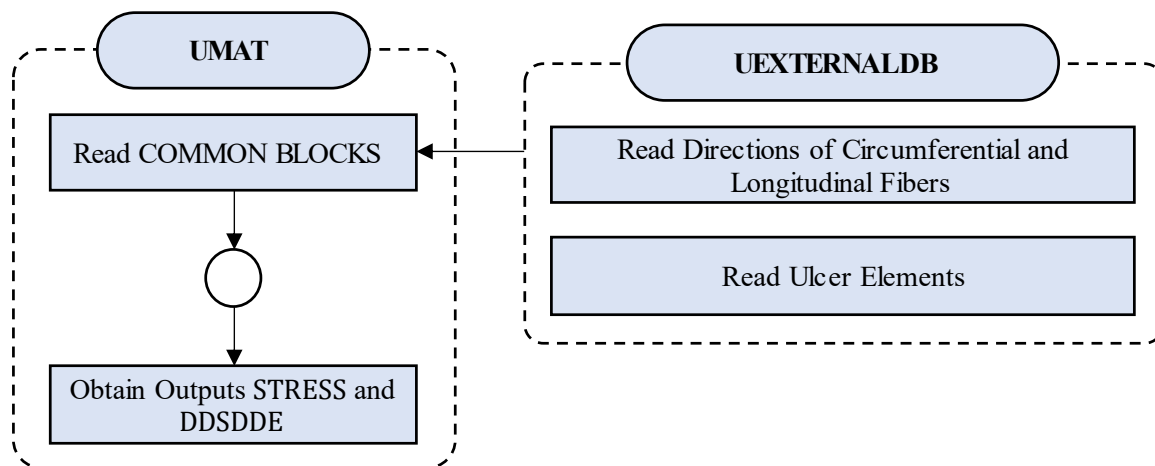


Figure 7.5. Connection between the UEXTERNALDB where the fibers direction and ulcer elements are identified and the UMAT subroutine.

7.2.1 Influence of the Mechanical Properties Diameter Reduction of the Constriction

The influence of the constitutive parameters of the matrix, of the passive behavior of longitudinal fibers and of the active parameter – muscle peak stress –, in the occlusion level produced by the contraction of the circumferential fibers, was investigated.

To test this influence, a sustained contraction of the circumferential fibers at half-length of the cylinder was accomplished. The cylinder was considered simply supported along the axial direction in the surfaces Z0 and Z100, and with symmetry along the planes Oyz and Oxz. The detailed description of the implemented activation function is described in the Section 7.3.

The method used was to vary the matrix properties (c, b), the passive properties of the longitudinal fibers (A_{LM}, a_{LM}) and the active properties of the circumferential fibers (T_0^M) around constitutive parameters found for the normal duodenum.

The matrix stiffness was found to have a great influence in the reduction of the inner diameter (Figure 7.6-a). This means that a stiffer matrix inhibits the deformation of the cylinder due to the contraction of the circumferential fibers. The same effect of decreasing the reduction of the inner diameter was found with stronger longitudinal fibers – Figure 7.6-b. Additionally, the stronger longitudinal fibers induced a smoother constriction along the cylinder, with the relative inner diameter being smaller than 100% at the cylinder's ends. In opposition to the previously analyzed cases, rising the muscle peak stress of the circumferential fibers leads to greater occlusion – Figure 7.6-c.

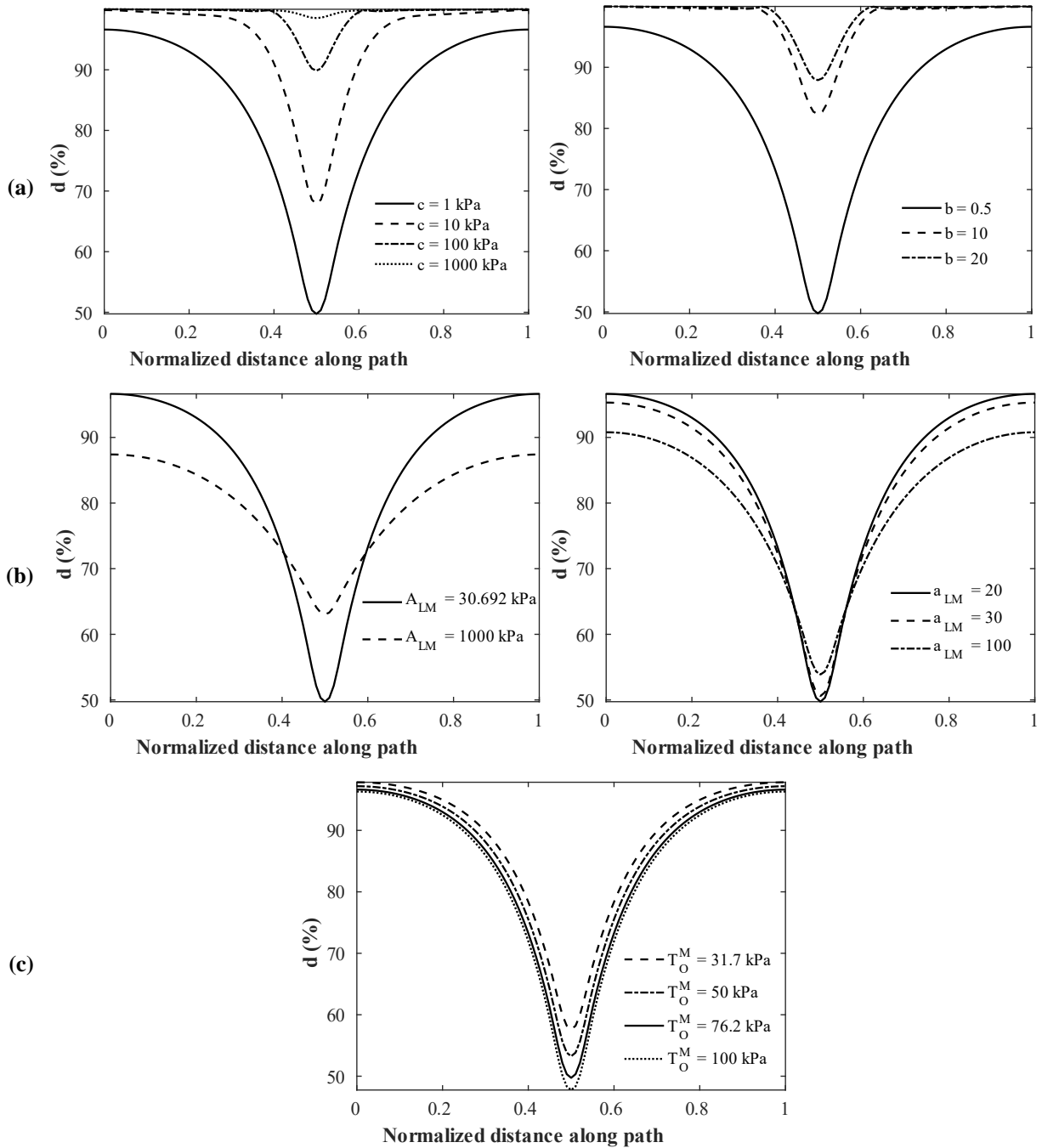


Figure 7.6. Influence of the matrix properties (a), passive properties of the longitudinal fibers (b) and active properties of the circumferential fibers (c) in the variation of the lumen relative diameter along the normalized distance of a longitudinal path of the inner surface.

This test was quite relevant as it helped understand how these constitutive parameters influence the constriction ring configuration before restricting the analysis to the mechanical properties found for the small intestine.

7.3 Activation

The activation of the muscular fibers was set as a space and time-dependent variable. To represent this intrinsic property, it was used an ABAQUS USDFLD subroutine, which allows to define field variables as functions of time or material quantities. At each time increment, the activation follows a function similar to the Figure 7.7. The USDFLD routine is linked to the UMAT using COMMON BLOCKS that are called at the beginning of each increment for each finite element’s integration points.

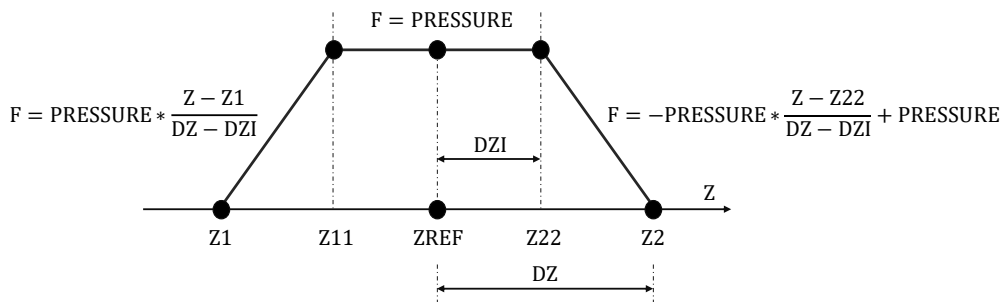


Figure 7.7. Activation function in each time increment.

Two methods of applying the activation were used while writing the USDFLD subroutine: position dependent USDFLD and element dependent USDFLD. In the first approach, the finite element would be activated only if the spatial coordinates of its integration points were within the limits [Z1, Z2]. By setting a speed for the activation propagation W, the reference position ZREF would move all through the cylinder. The flowchart for the position dependent USDFLD and its link to the UMAT subroutine is presented in the Figure 7.8.

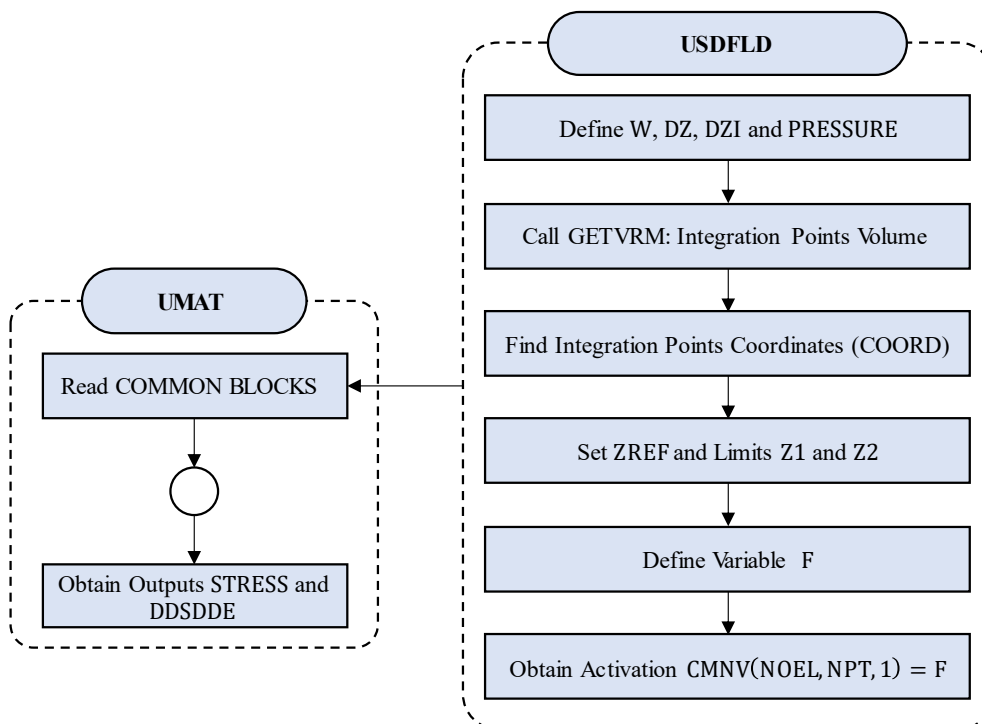


Figure 7.8. Flowchart of the position dependent USDFLD and its link to the UMAT subroutine.

The element dependent USDFLD defines the activation level based on the finite elements' mesh. By using a structured mesh with a defined number of elements along the radial (NESP), circumferential (NCIRC), and longitudinal (NLRAD/NESP) directions, it was possible to identify a set of elements in each increment to be activated around a reference position defined by ZREF. The activation function followed the same shape as before – Figure 7.7. However, as it is now applied directly to the element's integration points, the central constant activation (DZI) is followed by a linear decrease (dependent on the number of finite elements' columns ($NEL = DZ - DZI$)) until the activation's limits. The flowchart for the element dependent USDFLD and its link to the UMAT subroutine is presented in the Figure 7.9.

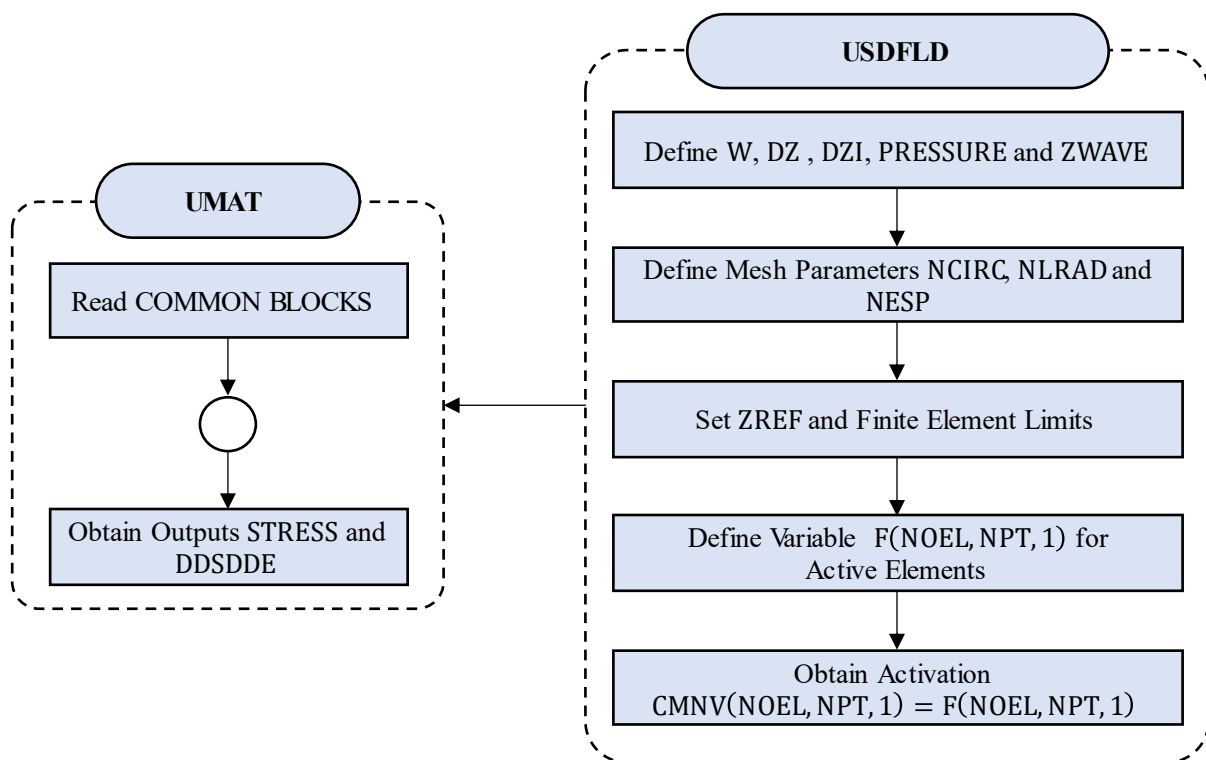


Figure 7.9. Flowchart of the element dependent USDFLD and its link to the UMAT subroutine.

7.3.1 Influence of the Activation Level Along the Cylinder's Thickness

A test was performed to evaluate the variation of the activation level, defined by the previously presented USDFLD subroutines, in several node paths within the cylinder's thickness – Figure 7.10. In order to allow free contraction of the circumferential fibers, the material (properties found for the normal duodenum) was considered an isotropic matrix embedded with circumferential fibers. The maximum activation level was set to $\alpha_{max} = 0.2$.

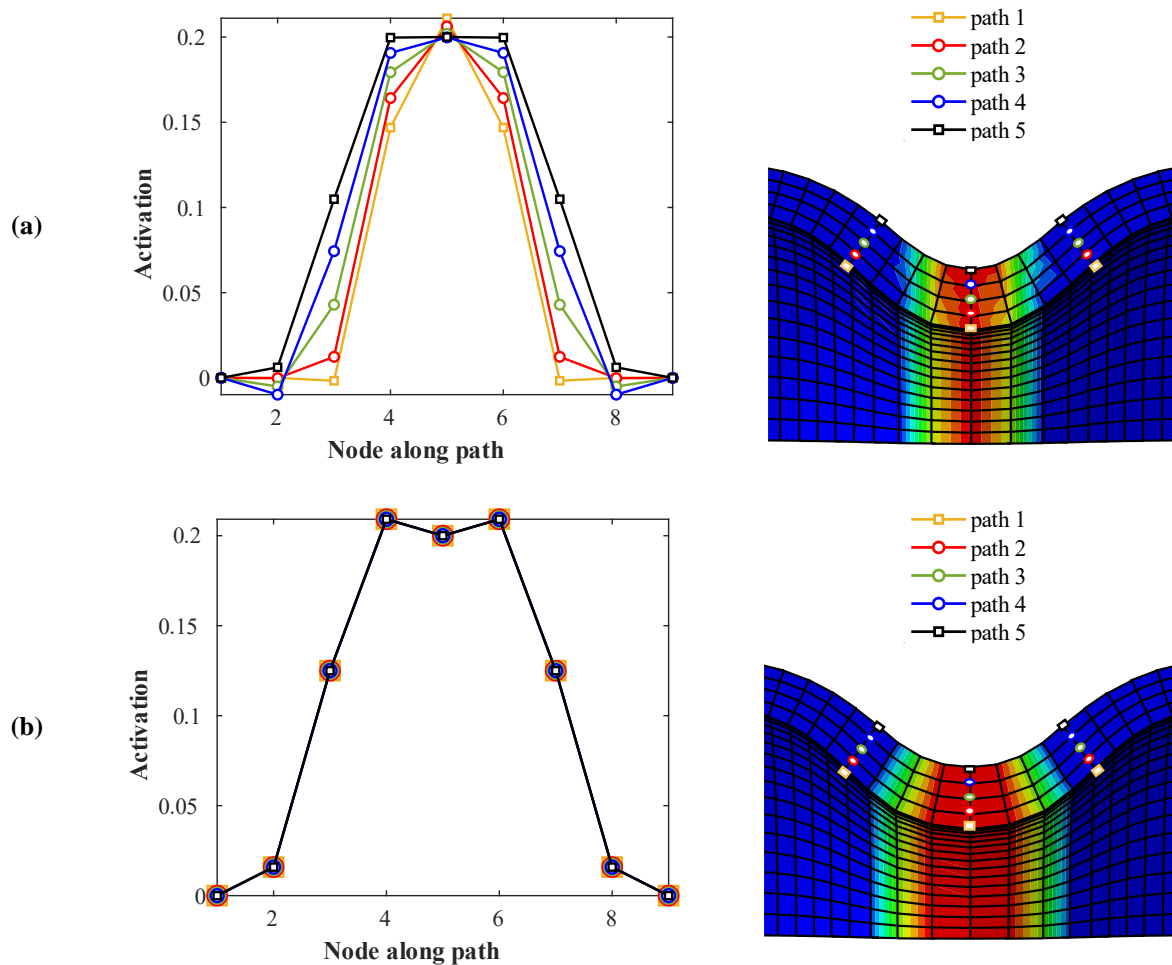


Figure 7.10. Evaluation of the activation level along different paths of the cylinder's thickness applied with the position dependent USDFLD (a) and with the element dependent USDFLD (b).

Even though it is a reasonable approach to define the activation level, the position dependent USDFLD can bring some difficulties when conjugated with large displacements and rotations. Firstly, having the fixed limits $[Z1, Z2]$ defined along the longitudinal direction of the cylinder leads to an irregular distribution of the activation level between the finite element layers – Figure 7.10-a. This problem is caused by the disregard of the variation of the limits $[Z1, Z2]$ along the thickness when the rotation of the elements is induced by the fibers' contraction. Moreover, by having the limits $[Z1, Z2]$ fixed until the activation reaches its maximum value, variations of the cylinder's length are not feasible. In this case, the coordinates of the integration points of the desired elements for activation could be placed outside the limits $[Z1, Z2]$. Otherwise, the coordinates of the integration points of the undesired elements for activation could be placed inside the limits $[Z1, Z2]$. Taking this into account, the position dependent USDFLD approach is only recommended for materials operating in the small deformations' regime to define, for instance, running loads.

Looking now at the Figure 7.10-b, where the element dependent USDFLD was used, it is possible to attain that the limitations found in the former approach were surpassed. In fact, the activation level was found constant along the layers of finite elements. Furthermore, any variation in the cylinder's

length would not influence the distribution of the activation as this is dependent on the finite element instead of the axial position. While being the most logical method for defining the activation level in this case, it has some limitations of its own, like being highly dependent on the finite element's mesh and on the orientation of the integration points within the element. Even though the subroutine is developed to allow a variation of the number of finite elements along the radial, circumferential, and longitudinal directions, any changes in the mesh stack orientation or in the orientation of the finite elements would require adjustments in the developed FORTRAN code. However, the multiple simulations performed in this work have held the mesh constant. So, this was not considered a critical drawback and the element dependent USDFLD was used to define the activation level of the circumferential fiber.

7.3.2 Implementation of the Peristaltic Wave in the Element Dependent USDFLD

A peristaltic wave like the one depicted in the Figure 3.2 (Wood 2004a), which considers the contraction of the circumferential (constriction ring) and longitudinal (lumen's enlargement) fibers, was initially considered. However, because of the properties found for the small intestine (longitudinal fibers stronger than the circumferential) and of the incompressibility constrain, the lumen's enlargement effect was unable to be obtained. Although the longitudinal fibers' contraction led to a stronger shortening of the small intestine, a localized increased of the thickness occurred in both radial directions. These findings resulted in the overlook of the contribution of longitudinal fibers to the peristaltic event. So, the work developed contemplates only the propelling constriction ring.

The characterization of the activation level for a peristaltic wave, in the element dependent USDFLD, considers three steps, similarly to the Figure 3.3 (where the visual parameters applied for the constriction ring were defined). Firstly, a fixed contraction, resultant from the linear increase of the activation level of the circumferential fibers (t_c), starts at the initial reference's position. Then, the chyme's propulsion occurs, as it is subjected to the movable constriction of the small intestine (t_p) along the propagation length of the wave ($Z_{WAVE} = 30$ mm). Finally, the activation level of the circumferential fibers drops linearly (t_r) – Figure 7.11. In the present analysis, the total time of the peristaltic wave (t_{wave}) was equally distributed among the previously mentioned steps and the wave time was represented by the dimensionless quantity t^* (indicating the wave time normalized between 0 and 1) – Equation (7.2). The evolution of the reference's position during a peristaltic contraction is drawn in the Figure 7.11 and detailed by the Equation (7.2). The reference position Z_{REF} remains constant during t_c and t_r . During the wave's propagation (t_p), Z_{REF} depends on the step time in the beginning of the increment t_0^{inc} and on the time increment Δt .

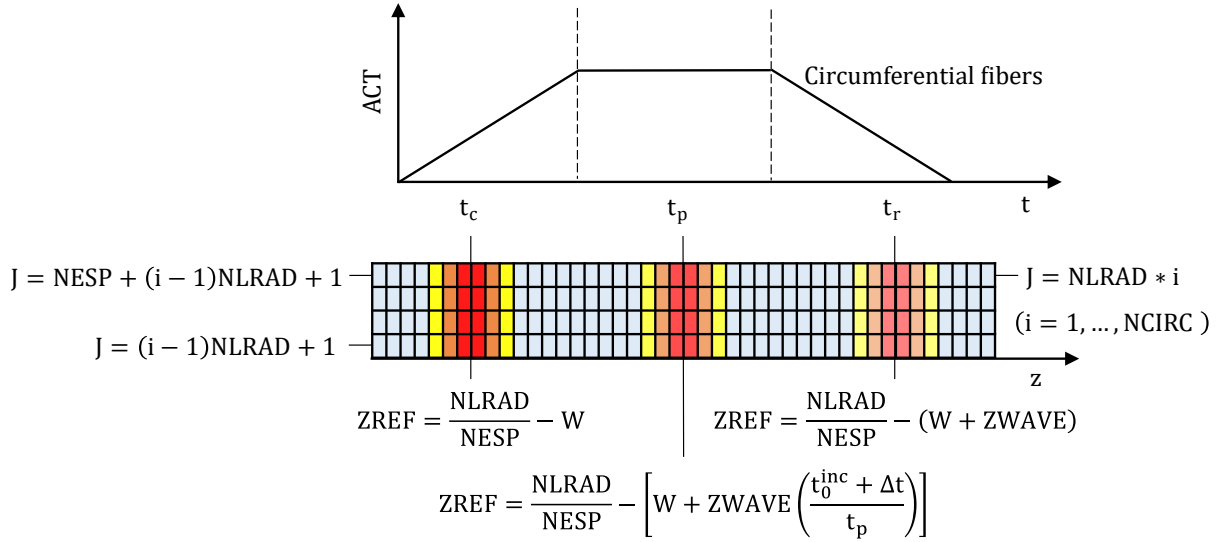


Figure 7.11. Evolution of the activation level (ACT) of the circumferential fibers and reference position (ZREF) during a peristaltic contraction with the time t . The evolution of the ZREF was represented for a cylindrical wedge i ($i = 1, \dots, \text{NCIRC}$), containing a NLRAD number of finite elements, each identified by a number J ranging between $(i - 1) \text{NLRAD} + 1$ and $\text{NLRAD} * i$.

$$ZREF = \begin{cases} \frac{\text{NLRAD}}{\text{NESP}} - W, & 0 < t^* \leq \frac{1}{3} \\ \frac{\text{NLRAD}}{\text{NESP}} - \left[W + ZWAVE \left(\frac{t_0^{\text{inc}} + \Delta t}{t_p} \right) \right], & \frac{1}{3} < t^* \leq \frac{2}{3}, \quad t_0^{\text{inc}} \in [0, t_p[\\ \frac{\text{NLRAD}}{\text{NESP}} - [W + ZWAVE], & \frac{2}{3} < t^* \leq 1 \end{cases} \quad (7.2)$$

$$\text{with } t^* = \frac{t [\text{ms}]}{t_{\text{wave}} [\text{ms}]}, \quad t_{\text{wave}} = t_c + t_p + t_r, \quad t_c = t_p = t_r$$

The evaluated simulations of the chyme's propulsion start with an enforced axial displacement of the chyme (45 mm) towards the entrance of the virtual small intestine's section (which can be viewed as resultant from the emptying of the stomach in the duodenum). This stretches the muscular fibers of the intestine's wall, inducing the described peristaltic event.

The boundary conditions applied to the chyme, specifically the ones applied along the axial displacement (U3), vary with the wave normalized time. The chyme is blocked during the development of the contractile ring and released in the remaining steps, as the sphere is supposed to be dragged along the tube. If the springs are connected to the chyme, the axial displacement of the last step is null to prevent the oral movement of the chyme due to the springs' force. The degrees of freedom left (1,2,4,5,6 for the analytical rigid sphere and 1,2 for the deformable sphere) stay fixed and constant over time – Equation (7.3).

$$\begin{cases} U1 \\ U2 \\ U3 \\ \theta1 \\ \theta2 \\ \theta3 \end{cases} = \begin{cases} 0 \\ 0 \\ U3(x,y,z,t) \\ 0 \\ 0 \\ 0 \end{cases}, \quad U3(x,y,z,t) = \begin{cases} 0, & 0 < t^* \leq \frac{1}{3} \\ \text{free}, & \frac{1}{3} < t^* \leq \frac{2}{3} \\ \text{free or } 0, & \frac{2}{3} < t^* \leq 1 \end{cases} \quad (7.3)$$

7.4 Selecting Initial and Boundary Conditions for the Small Intestine

An analysis of the boundary conditions imposed to the small intestinal portion was performed since the occlusion level depends upon these. The same model used in the Section 7.2.1 and Section 7.3.1 was employed, with a maximum activation level of $\alpha_{\max} = 1$. Three boundary condition cases were considered for this preliminary analysis (Figure 7.12): both ends fixed along the longitudinal direction (Z00); surface Z0 fixed along the longitudinal direction and surface Z100 free (Z0F); and, finally, surface Z0 fixed along the longitudinal direction and surface Z100 fixed to the ground, using springs with a stiffness of 1E-5 N/mm (Z0S).

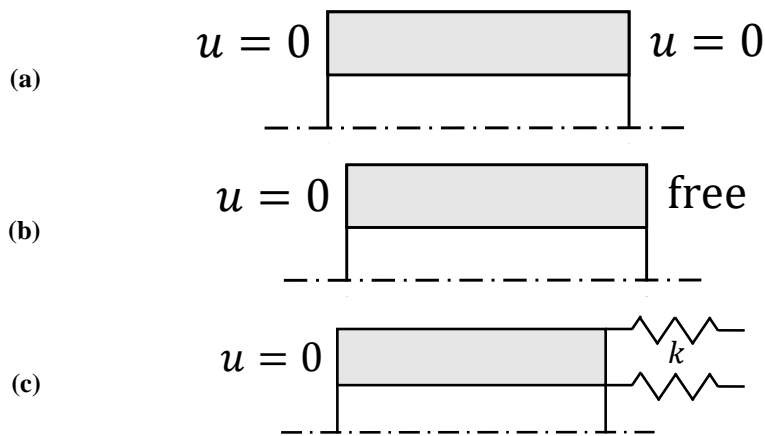


Figure 7.12. Boundary conditions applied to the small intestine's ends: fixed-fixed Z00 (a), fixed-free Z0F (b) and fixed-springs Z0S (c).

The variation of the lumen's relative diameter along the normalized distance of a longitudinal path of the inner surface is drawn in the Figure 7.13 for each of the cases.

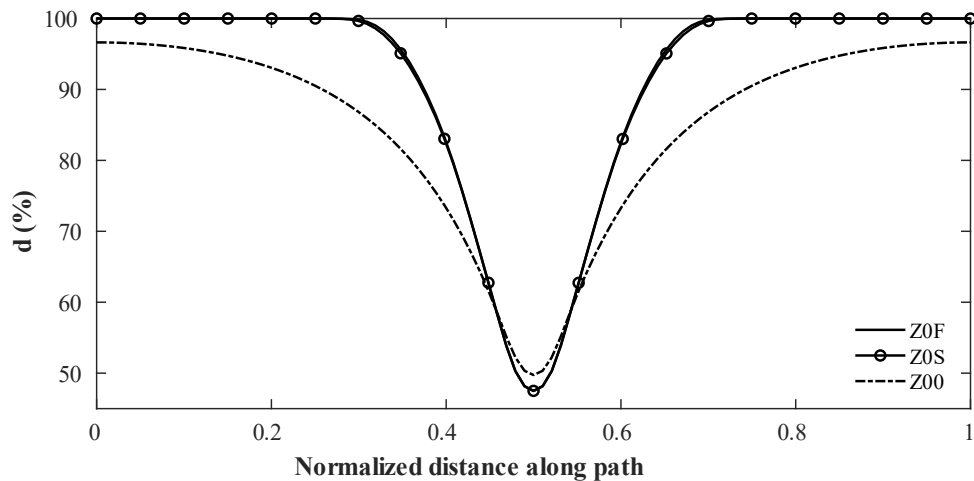


Figure 7.13. Variation of the lumen relative diameter along the normalized distance of a longitudinal path of the inner surface for three sets of boundary conditions applied to the small intestine's ends: fixed-free (Z0F), fixed-springs (Z0S) and fixed-fixed (Z00).

Firstly, the ends were considered fixed along the axial direction (Z00). This is consistent with an *ex vivo* lab preparation of the intestine for evaluation of the peristaltic reflex. Usually, in these experimental procedures, the ends are tied and fixed along the longitudinal direction (Sinnott et al. 2017). As already pointed out in the Section 3.2, the fixed ends diminish the ability of the small intestine to reduce its diameter during the activation of the circumferential fibers (Tobergte and Curtis 2013). From the Figure 7.13, it is possible to conclude that the smaller internal diameter's reduction (50.26%) was obtained with the Z00 boundary conditions. Additionally, this resulted in a smoother constriction ring and in a continuous reduction of the internal diameter along the entire path, which is caused by the longitudinal fibers.

Then, a second set of boundary conditions was used with the surface Z100 free. This would allow free lengthening of the tube and a greater level of occlusion. This situation is closer to the *in vivo* behavior of the small intestine (Tobergte and Curtis 2013). In fact, from the Figure 7.13, it is possible to observe a diameter reduction of 52.52%, which corresponds to a slight increase. Furthermore, as the length is free to shorten, the diameter reduction is localized. This is far different from the distributed diameter reduction found with fixed-fixed ends.

Even though the shape of the constriction ring was similar to the expected, another approach was used to define the boundary conditions of the small intestine. The last attempt considered the surface Z100 connected to the ground by springs associated with the longitudinal displacement. This showed a slight level of resistance to the small intestine's shortening, because the *in vivo* Z100 surface was supposed to be connected to the remaining small intestine. However, the stiffness of the springs was set with a small value of $1E-5$ N/mm, in order to allow the same free shortening level as if the surface Z100 was merely free.

Finally, the cylinder's boundary conditions can be described by the Z0S case – Figure 7.14. In order to assure radial symmetry, all nodes in the planes Oyz and Oxz were fixed in the circumferential direction.

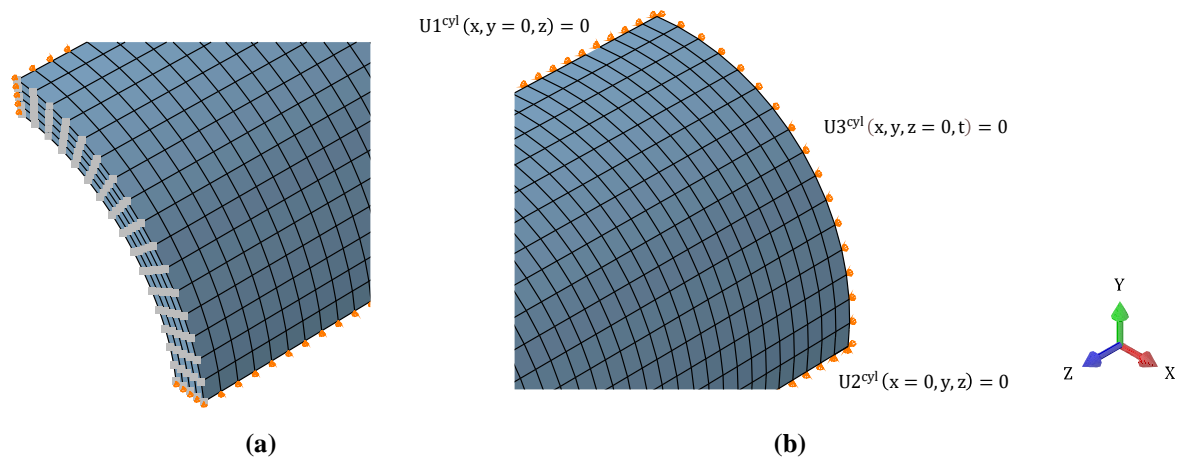


Figure 7.14. Cylinder's boundary conditions: fixed with springs along the longitudinal direction to the ground in the surface $Z=100$ (a); simply supported along the longitudinal direction in the surface $Z=0$ (b); symmetry along the planes Oyz and Oxz (a) and (b).

7.5 Selecting Propulsive Resistance

To select the propulsive resistance described in the model by the friction coefficient and by the stiffness of the springs connected to the chyme, an analysis of these parameters was accomplished.

The lubrication mechanism of the internal layer (mucus secretion) of the small intestine has a large impact in the propulsive capability and in protecting the wall from possible injuries (Yoshida et al. 2003). The friction coefficient depends on the amount of water of the surface, being reduced with a higher percentage of water in the inner layers (Yoshida et al. 2003).

Therefore, the friction coefficient was set variable to evaluate its influence in the chyme's propulsion. The analysis was performed using the springless model of the Figure 7.2-a for the normal duodenum, using four different values for the friction coefficient, varying from the frictionless case to a friction coefficient of 0.1. In the Figure 7.15, it is possible to see that the chyme's propagation decreases largely due to higher friction values. The larger friction coefficient values can be interpreted both as the result of: dehydration of the small intestinal wall; or the interaction of the small intestine's surface with medical devices, like capsule endoscopes ($\mu = 0.08 - 0.2$) (Guo et al. 2020). Taking this into consideration, the friction coefficient of 0.001 was chosen to be used in the following simulations, as it would not negatively influence the chyme's propulsion.

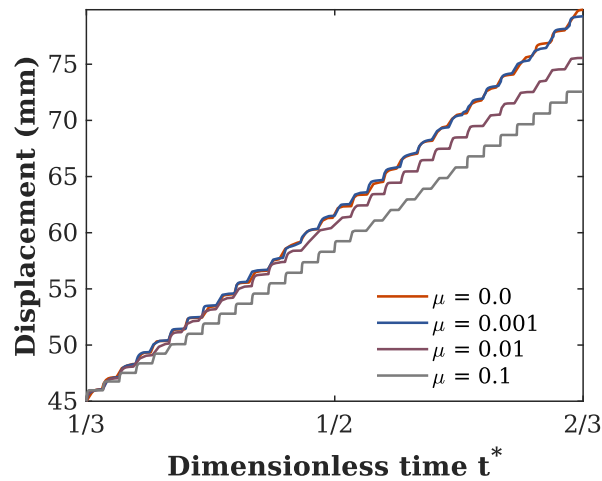


Figure 7.15. Displacement induced in the chyme by the contraction of the circumferential muscle fibers with variable friction coefficient.

The second parameter which defines the propulsive resistance, also chosen based on the normal duodenum, is the stiffness of the springs connected to the chyme – Figure 7.2-c. This was selected in a way that would have a slight influence over the chyme’s propulsion, but that would not induce the tract’s obstruction or the chyme’s free passage towards the oral direction. From Figure 7.16, the springs stiffness was chosen as 0.01 N/m.

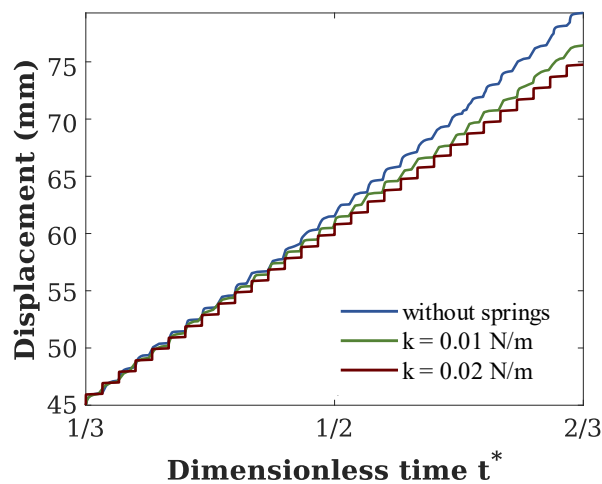


Figure 7.16. Displacement induced in the chyme by the contraction of the circumferential muscle fibers with variable spring’s stiffness.

7.6 Variation of the Propulsive Capability with the Distal Direction

In the Chapter 6, the mechanical properties of the small intestine were found to vary along the axial direction. Therefore, two sets of constitutive parameters were used to differentiate the duodenum and the ileum. In this section, these constitutive parameters were incorporated into the model of the Figure 7.2-c and the propulsive behavior was compared.

The evolution of the chyme's displacement, resultant from the peristaltic event, drawn in the Figure 7.17, indicates a slim decrease in the propulsive capability. This is consistent with the already described functions for each section. By propelling the chyme faster over higher distances, the duodenum helps the gastric emptying, while the slower and shorter transit in the ileum helps the digestion and absorption of nutrients (Dou et al. 2003).

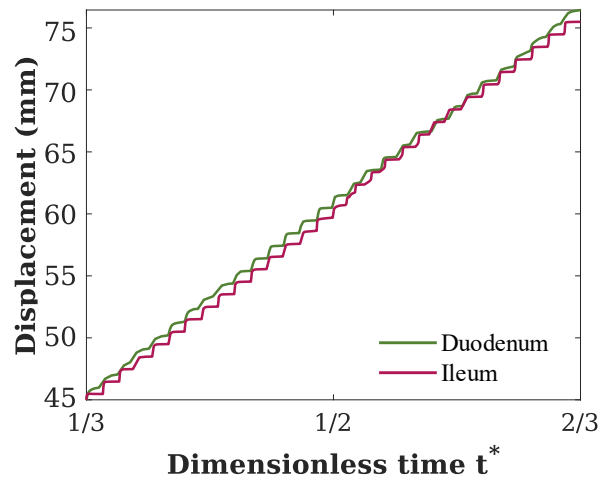


Figure 7.17. Displacement induced in the chyme by the contraction of the circumferential muscle fibers considering an axial variation of the mechanical properties of the small intestine in the duodenum and ileum.

In the Figure 7.18, the absolute value for the axial reaction in the chyme (measured in the reference point) is plotted for the second step of the analysis. As the Z100 surface is free to shorten, the reaction in the chyme results from the equilibrium between the force generated by the contraction of the circumferential fibers (F_{cont}), the force generated by springs connected to the chyme and the force induced in the sphere by the small intestine's shortening (F_{short}) (opposite direction to the movement). By performing the comparison between the duodenum and the ileum, it is possible to verify that the reaction force in the duodenum's simulation is higher and the force F_{cont} overweighs the F_{short} quicker than in the ileum's. This higher force should allow the mixture and propagation of the larger volume of intake luminal contents from the stomach.

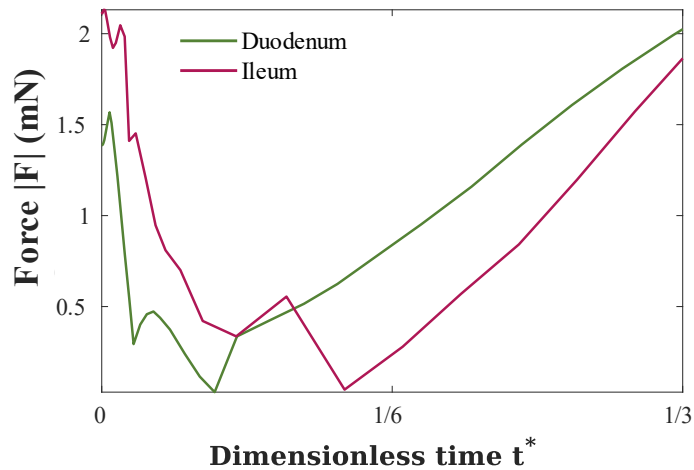


Figure 7.18. Axial reaction force (absolute value) in the chyme measured in the reference point during a contraction of the circumferential muscle fibers considering an axial variation of the mechanical properties of the small intestine in the duodenum and ileum.

Finally, the distribution of the maximum principal stress along a longitudinal normalized path in the inner surface for $t^* = \frac{1}{3}$ (after full fixed contraction of the circumferential fibers) was plotted in the Figure 7.19. The first peak of the maximum principal stress matches the contraction of the circumferential fibers. Even though the circumferential fibers are stiffer than in the duodenum (Figure 6.8), the biomechanical model for the ileum section showed a smaller principal stress in the occluding segment. This is related, not to the influence of the circumferential fibers, but, instead, to the influence of its more compliant longitudinal fibers. The second peak results from the passive stretching of the muscle fibers within the wall by the chyme. Here, the stronger circumferential fibers may be held responsible for the maximum peak present in the ileum.

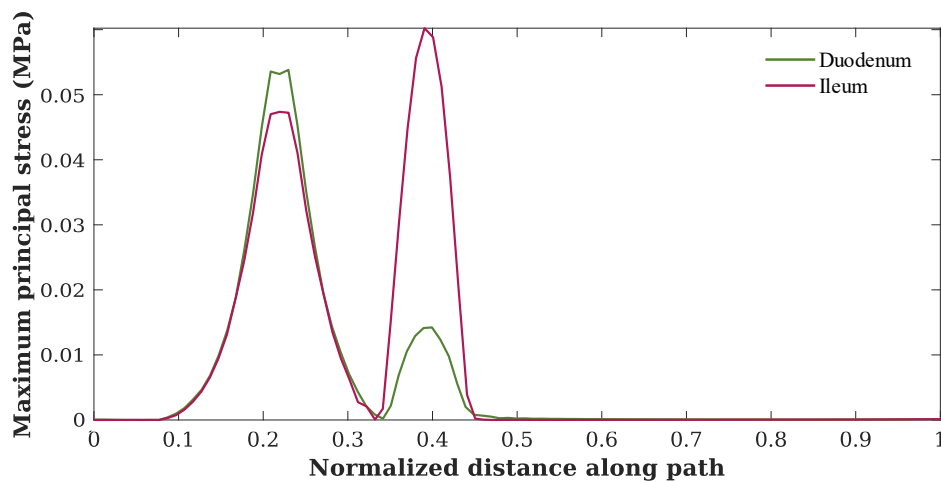


Figure 7.19. Distribution of the maximum principal stress in a normalized axial path on the inner surface of the small intestine considering an axial variation of the mechanical properties of the small intestine in the duodenum and ileum for $t^* = \frac{1}{3}$.

7.7 Influence of Chyme Stiffness in Propulsion

Up until now, the influence of the chyme’s stiffness was disregarded, and the simulations were performed with an analytical rigid sphere to model the chyme. However, the influence of the chyme’s stiffness in the propulsive capability of the small intestine is relevant because the contraction of the small intestine’s wall may induce deformation in the luminal content.

Consequently, the model of the Figure 7.2-b, for the springless normal duodenum, was used with the chyme casted as an incompressible hyperelastic neo-Hookean material with $C_{10} = 1$ kPa. The value for the material parameter C_{10} was chosen to be of the same order of the small intestine’s matrix stiffness. The axial movement of the chyme, generated by the active contraction of the circumferential fibers of the wall for the rigid and soft cases, is outlined in the Figure 7.20.

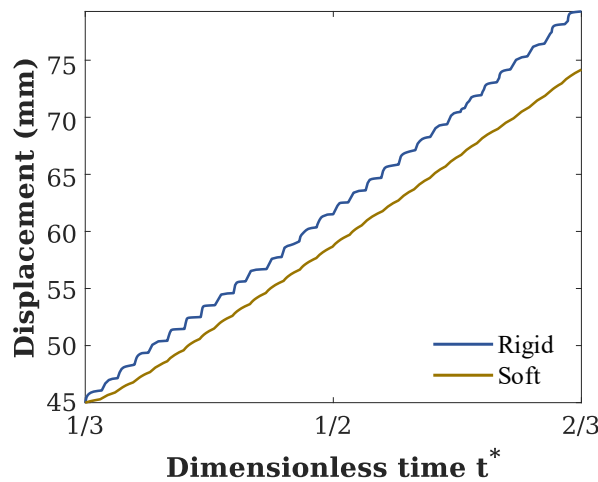


Figure 7.20. Displacement induced in the chyme by the contraction of the circumferential muscle fibers with variable chyme’s stiffness.

The Figure 7.20 reveals that, when analyzing the same peristaltic wave, a softer chyme is propelled along a shorter distance than a more rigid one. In fact, the reason behind this reduced propulsive capability is associated to the chyme’s deformation by the small intestine wall (Figure 7.21). Since a part of the energy generated by the peristaltic contraction is used to deform the chyme, the conversion into kinetic energy is reduced.

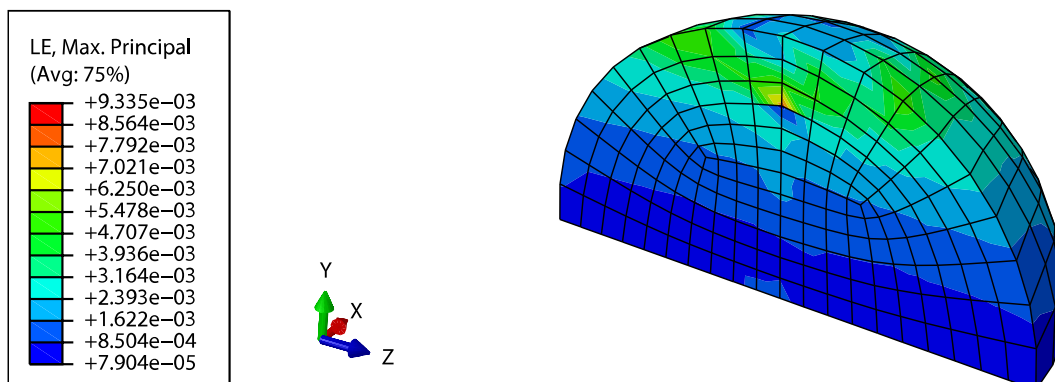


Figure 7.21. Distribution of the maximum principal logarithmic strain on the model of the chyme for $t^* = 1$.

7.8 Influence of Gastrointestinal Limitations in the Chyme Propulsion

To evaluate the influence of gastrointestinal limitations in the chyme propulsion, the duodenum of a healthy patient was compared to the duodenum of a SS patient and an individual with an ulcer of variable size (Figure 7.4). The results for the propulsive displacement of the sphere and axial reaction force (absolute value) measured in the reference point of the chyme are presented in the Figure 7.22.

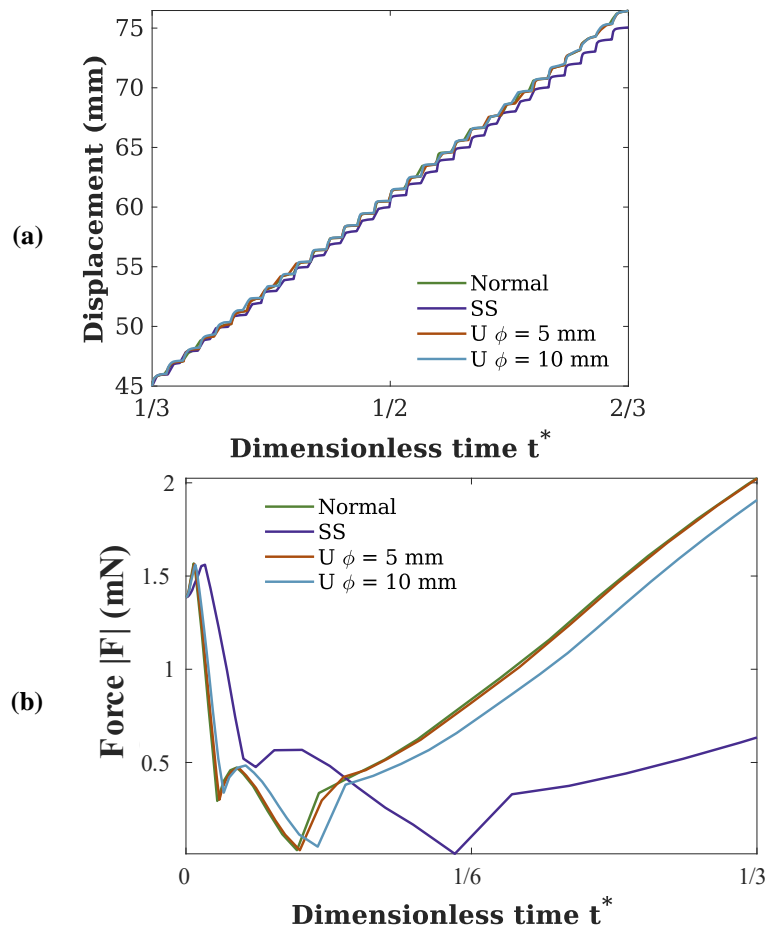


Figure 7.22. Displacement (a) and axial reaction force (absolute value) (b) in the chyme measured in the reference point during a contraction of the circumferential muscle fibers in a normal patient, a SS patient and a patient with an ulcer of variable size.

While comparing the propulsive behavior in each of these cases – Figure 7.22 –, it is possible to observe that, due to the muscular atrophy (Gregersen et al. 2007), the SS small intestine is unable to generate the same force as a healthy intestine, during the circumferential fibers contraction. Consequently, this leads to the propulsion of the chyme over shorter distances. Furthermore, the energy generated by the wall is much smaller in a SS patient, which is easily understood by the Figure 7.23.

Looking now into the behavior of a portion of the small intestine with an ulcer without active capability in its surface, it is possible to see that the size of the damaged area may have a considerable influence in the force generated for the chyme's propulsion – Figure 7.22. In fact, in the light of these results, it is most likely that patients with larger (and perhaps with more) ulcers in the small intestine's

surface will experience a decreased propulsive capability. These assumptions follow both the results found for the force generated during the contraction and the results found for the energy produced by the organ – Figure 7.23. The ulcer introduces a localized variation of the energy produced by the wall, which can be seen between $t^* \in [0, \frac{1}{3}]$. This variation decreases the energy induced and it is as big as the ulcer’s size. Though differences have not been found in the distance travelled by the chyme, it is possible to hypothesize that, if the damaged area of the mucosa was located within the propagation length of the peristaltic wave, the propulsive behavior could be impaired.

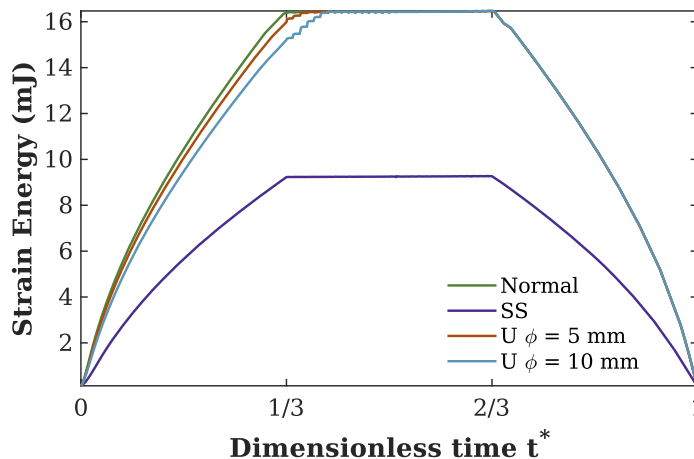


Figure 7.23. Temporal variation of the strain energy in the duodenum for a normal patient, a SS patient and a patient with an ulcer of variable size.

Finally, by analyzing the distribution of the maximum principal stress in a longitudinal normalized path of the intestine inner surface (Figure 7.24), it is possible to see that the maximum peak resultant from the contraction of the circumferential fibers occurred at lower tension in the SS duodenum. This is, once more, an indicator of the muscular atrophy. The presence of the ulcer also lowered the peak, especially for larger diameters of the injury.

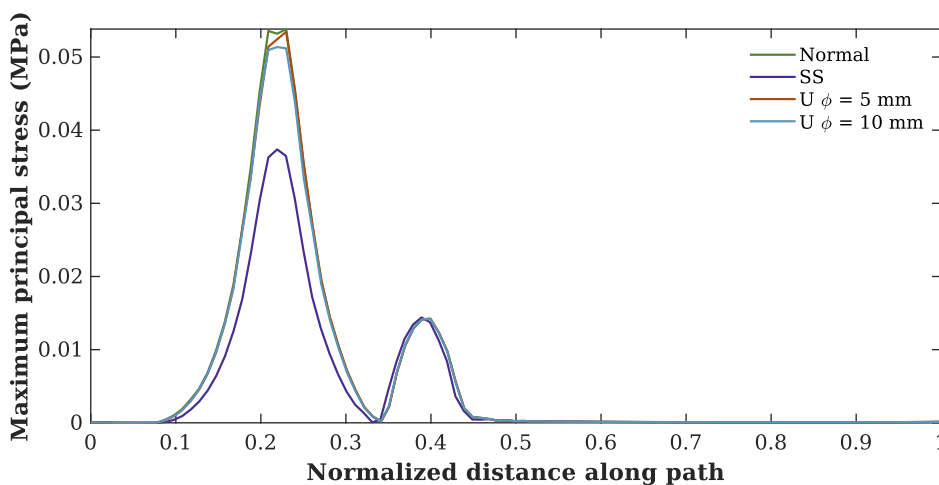


Figure 7.24. Distribution of the maximum principal stress in a normalized axial path on the inner surface of the small intestine duodenum for a normal patient, a SS patient and a patient with an ulcer of variable size for $t^* = \frac{1}{3}$.

7.9 Final Remarks

In this chapter, the small intestine was simplified as a quarter of a deformable cylinder with two families of muscle fibers along the longitudinal and circumferential directions. Instead of looking into the flow patterns of the chyme in the small intestine, this work focused on the comparison of the chyme's propulsion in patients with gastrointestinal limitations. For such purpose, the chyme was simplified as a spherical body.

The chyme's propulsion in the small intestine is promoted by peristaltic contractions, which, in this work, overlook the contribution of the longitudinal fibers contraction in front of the chyme. This resulted from the failure in promoting the lumen's enlargement, probably due to the incompressible restraint, the chosen boundary conditions and the mechanical properties of the wall (as the longitudinal fibers are much stronger than the circumferential). The peristaltic wave was defined only by a constriction ring resultant from the contraction of the circumferential fibers in the oral side of the chyme. Their activation signal was set by a space and time dependent variable in a USDFLD subroutine.

The small intestine was considered with a free end connected by longitudinal springs of small stiffness to the ground to enable the free shortening of the tube, while considering a slim resistance level (which represents the physiological range of the small intestine's shortening). Furthermore, a propulsive resistance was considered. This was represented by (i) the friction level in the contact between the small intestine and the chyme (which depends on the water percentage in the inner layers of the organ); and by (ii) springs connected to the chyme to represent the chyme's continuity along the tract.

The mechanical properties found in the uniaxial test for the duodenum and ileum were used in the simulations. It was possible to find smaller propulsive capability, as well as smaller propulsive force, developed by the wall in the distal direction. This corroborates with the biological functions of each section of the intestine, as the duodenum must propel the chyme further and develop higher forces to propagate the large volume intake resultant from the stomach emptying, and the ileum should enhance the absorption of nutrients.

The propulsive capability with a variable chyme's stiffness was also evaluated. It was verified that softer luminal contents are subjected to higher deformations, which lower the propelled distance.

Finally, the comparison between healthy individuals and patients with gastrointestinal limitations, like systemic sclerosis and peptic ulcers, was established. It was found that the force generated by the peristaltic contraction would be decreased in these patients and that the propulsive distance could also be reduced.

CHAPTER 8

CONCLUSIONS AND FUTURE WORK

8.1 Conclusions

In this work, a detailed study of the peristaltic movements in the small intestine was performed, in order to develop the contractile ring responsible for the chyme's propulsion.

The small intestine was treated as an incompressible transversely isotropic hyperelastic material according to the Martins Model (Martins et al. 1998) and its mechanical behavior was described by an ABAQUS UMAT subroutine (Ferreira et al. 2017). A similar constitutive model, considering the decoupling of the mechanical behavior of the intestinal wall based on microstructure considerations, has been employed previously in the work of Ciarletta et al. (2009) for the large intestine.

To obtain the constitutive parameters for the analysis, uniaxial tests were performed in the longitudinal and circumferential directions of the small intestine. From these tests, it was found that the mechanical behavior of the small intestine varies both distally (along the sections of the tract – duodenum, jejunum, ileum) and with the considered direction (longitudinal and circumferential).

The constitutive parameters were included into a biomechanical model in the software ABAQUS, with the purpose of testing the propulsive behavior of the small intestine during a peristaltic contraction. The peristaltic contraction was defined by a space and time dependent activation level of the circumferential fibers, later integrated into a USDFLD subroutine.

The peristaltic activity in the small intestine is quite complex and, even with the multiple studies of the peristaltic reflex *in vitro*, the response of the small intestine to this contractile mechanism *in vivo* is still not completely clear (Tobergte and Curtis 2013). Therefore, it is important to outline that the results obtained in this work are valid within the scope of the simplifications employed for the shape and propagation of the peristaltic contraction, for the geometry and boundary conditions of the small intestine and for the material and shape of the chyme.

Regardless, this research allowed the evaluation of the small intestine's propulsion capability and the comparison between healthy individuals and patients with gastrointestinal limitations. It was found that the force generated by the peristaltic contraction would be decreased in these patients and that the

propulsive distance could also be reduced. In ulcer patients, the latter remains a hypothesis based on the work developed. Additionally, the influence of the mechanical properties of the small intestine's wall (by comparing the propulsive behavior along the tract) and the mechanical properties of the chyme (by considering variable stiffness for the luminal contents) were also investigated.

8.2 Future Work

Even though reasonable stress-stretch curves were found in the Chapter 6 to describe the small intestine's behavior, as these were similar to the findings of Egorov et al. (2002) and Ciarletta et al.(2009), the present analysis could be improved if at least 5 different small intestines had been subjected to uniaxial tests. Apart from the improvements already mentioned in the Section 6.5 (thickness measurement after cutting to avoid dehydrated specimens and polymeric holders for fixation), to complement the uniaxial tests, two shear tests along the circumferential and longitudinal directions could be additionally performed like in Ciarletta et al. (2009).

In this work, the viscoelastic behavior of the small intestinal wall, though recognized, was disregarded. Future improvements could be presented by adding viscoelasticity to the model. Also, as the smooth muscle contraction is a complex interdisciplinary phenomenon, using a constitutive model which represents both the mechanical and chemical processes engaged in the activation of the muscular fibers could benefit the analysis (Kroon 2009).

Enhancements in the definition of the model could also add value to the analysis, such as considering the chyme as a fluid or changing the boundary conditions applied to the small intestine by adding the mesentery. As the mesentery attaches the intestine to the posterior abdominal wall, considering a free small intestine only connected along the longitudinal direction to the mesentery would likely allow the *in vivo* free shortening.

The friction coefficient was set constant for the entire contact length between the chyme and the small intestine. However, the mucus secretion by the mucosa cells could be considered localized and different friction coefficients could be set within the small intestine's length. Specifically, a lower friction could be added in front of the chyme to enhance the propulsion.

By implementing some of the described changes in the future, this model can become a powerful tool to evaluate the effects of gastrointestinal limitations in the chyme's propulsion and the influence of the peristaltic contractions in the movement of capsule endoscopes.

REFERENCES

- Al-Shboul, Othman A. 2013. "The Importance of Interstitial Cells of Cajal in the Gastrointestinal Tract." *Saudi Journal of Gastroenterology : Official Journal of the Saudi Gastroenterology Association* 19 (1): 3–15. <https://doi.org/10.4103/1319-3767.105909>.
- Almeida, N., J. M. Romãozinho, M. M. Donato, C. Luxo, O. Cardoso, M. A. Cipriano, C. Marinho, A. Fernandes, C. Calhau, and C. Sofia. 2014. "Helicobacter Pylori Antimicrobial Resistance Rates in the Central Region of Portugal." *Clinical Microbiology and Infection* 20 (11): 1127–33. <https://doi.org/10.1111/1469-0691.12701>.
- Avvari, Ravi Kant. 2019. "Effect of Local Longitudinal Shortening on the Transport of Luminal Contents through Small Intestine." *Acta Mechanica Sinica/Lixue Xuebao* 35 (1): 45–60. <https://doi.org/10.1007/s10409-018-0809-5>.
- Bellini, Chiara, Paul Glass, and Elena S. Di Martino. 2017. "Constitutive Modeling of the Small Intestine." In *Biomechanics of Living Organs: Hyperelastic Constitutive Laws for Finite Element Modeling*, 287–305. Elsevier Inc. <https://doi.org/10.1016/B978-0-12-804009-6.00013-4>.
- Bellini, Chiara, Paul Glass, Metin Sitti, and Elena S. Di Martino. 2011. "Biaxial Mechanical Modeling of the Small Intestine." *Journal of the Mechanical Behavior of Biomedical Materials* 4 (8): 1727–40. <https://doi.org/10.1016/j.jmbbm.2011.05.030>.
- Bergamasco, Aurore, Nadine Hartmann, Laura Wallace, and Patrice Verpillat. 2019. "Epidemiology of Systemic Sclerosis and Systemic Sclerosis-Associated Interstitial Lung Disease." <https://doi.org/10.2147/CLEP.S191418>.
- Bonet, Javier, and Richard D. Wood. 2008. *Nonlinear Continuum Mechanics for Finite Element Analysis, 2nd Edition*. *Nonlinear Continuum Mechanics for Finite Element Analysis, 2nd Edition*. Vol. 9780521838. <https://doi.org/10.1017/CBO9780511755446>.
- Calvo, Jose Luis. 2020a. "First Portion of the Duodenum Showing the Brunner Glands Located on the Submucosa on the Circular Folds or Kerckring Valves. Here, the Intestinal Villi Are Not Very Long and Have a Lamina Shape." Shutterstock. 2020. <https://www.shutterstock.com/pt/image-photo/first-portion-duodenum-showing-brunner-glands-743928883>.
- Calvo, Jose Luis. 2020b. "Very Low Magnification Micrograph Showing a Cross Sectioned Duodenum Showing the Brunner Glands Located on the Submucosa on the Circular Folds or Kerckring

- Valves.” Shutterstock. 2020. <https://www.shutterstock.com/pt/image-photo/very-low-magnification-micrograph-showing-cross-1692153217>.
- Ciarletta, P., P. Dario, F. Tendick, and S. Micera. 2009. “Hyperelastic Model of Anisotropic Fiber Reinforcements within Intestinal Walls for Applications in Medical Robotics.” *International Journal of Robotics Research* 28 (10): 1279–88. <https://doi.org/10.1177/0278364909101190>.
- Dou, Yanling, Jingbo Zhao, and Hans Gregersen. 2003. “Morphology and Stress-Strain Properties along the Small Intestine in the Rat.” *Journal of Biomechanical Engineering* 125 (2): 266–73. <https://doi.org/10.1115/1.1560140>.
- Egorov, Viacheslav I., Ilia V. Schastlivtsev, Edward V. Prut, Andrey O. Baranov, and Robert A. Turusov. 2002. “Mechanical Properties of the Human Gastrointestinal Tract.” *Journal of Biomechanics* 35 (10): 1417–25. [https://doi.org/10.1016/S0021-9290\(02\)00084-2](https://doi.org/10.1016/S0021-9290(02)00084-2).
- Feldman, Mark, Lawrence Friedman, and Lawrence Brandt. 2010. *Gastrointestinal and Liver Disease*. <https://www.elsevier.com/books/sleisenger-and-fordtrans-gastrointestinal-and-liver-disease-2-volume-set/feldman/978-1-4160-6189-2>.
- Fernandez-Urien, Ignacio, Cristina Carretero, Erika Borobio, Ana Borda, Emilio Estevez, Sara Galter, Begoña Gonzalez-Suarez, et al. 2014. “Capsule Endoscopy Capture Rate: Has 4 Frames-per-Second Any Impact over 2 Frames-per-Second?” *World Journal of Gastroenterology* 20 (39): 14472–78. <https://doi.org/10.3748/wjg.v20.i39.14472>.
- Ferreira, J. P. S., M. P. L. Parente, M. Jabareen, and R. M. Natal Jorge. 2017. “A General Framework for the Numerical Implementation of Anisotropic Hyperelastic Material Models Including Non-Local Damage.” *Biomechanics and Modeling in Mechanobiology* 16 (4): 1119–40. <https://doi.org/10.1007/s10237-017-0875-9>.
- Gao, F., D. Liao, A. M. Drewes, and H. Gregersen. 2009. “Modelling the Elastin, Collagen and Smooth Muscle Contribution to the Duodenal Mechanical Behaviour in Patients with Systemic Sclerosis.” *Neurogastroenterology and Motility* 21 (9). <https://doi.org/10.1111/j.1365-2982.2009.01314.x>.
- Ghoshal, Uday C. 2019. “Small Intestinal Motility Disorders.” In *Clinical and Basic Neurogastroenterology and Motility*, 319–29. Elsevier. <https://doi.org/10.1016/B978-0-12-813037-7.00022-4>.
- Gilchrist, M. D., J. G. Murphy, W. Parnell, and B. Pierrat. 2014. “Modelling the Slight Compressibility of Anisotropic Soft Tissue.” *International Journal of Solids and Structures* 51 (23–24): 3857–65. <https://doi.org/10.1016/j.ijsolstr.2014.06.018>.
- Gregersen, H. 2003. *Biomechanics of the Gastrointestinal Tract: New Perspectives in Motility Research and Diagnostics*. Springer. [https://doi.org/10.1016/s1590-8658\(03\)00463-8](https://doi.org/10.1016/s1590-8658(03)00463-8).
- Gregersen, H., D. Liao, J. Pedersen, and A. M. Drewes. 2007. “A New Method for Evaluation of Intestinal Muscle Contraction Properties: Studies in Normal Subjects and in Patients with Systemic Sclerosis.” *Neurogastroenterology and Motility* 19 (1): 11–19. <https://doi.org/10.1111/j.1365-2982.2006.00837.x>.

- Guo, Bingyong, Ellis Ley, Jiyuan Tian, Jiajia Zhang, Yang Liu, and Shyam Prasad. 2020. “Experimental and Numerical Studies of Intestinal Frictions for Propulsive Force Optimisation of a Vibro-Impact Capsule System.” *Nonlinear Dynamics* 101 (1): 65–83. <https://doi.org/10.1007/s11071-020-05767-4>.
- Guyton, Arthur C., and John E. Hall. 2006. *Textbook of Medical Physiology. Physiology*. 11th ed. Philadelphia: Elsevier Saunders.
- Hasler, William L. 2004. “Duodenal Motility.” In *Encyclopedia of Gastroenterology*, 636–41. Elsevier. <https://doi.org/10.1016/b0-12-386860-2/00196-9>.
- Hill, Archibald Vivian. 1938. “The Heat of Shortening and the Dynamic Constants of Muscle.” *Proceedings of the Royal Society of London. Series B - Biological Sciences* 126 (843): 136–95. <https://doi.org/10.1098/rspb.1938.0050>.
- Hoeg, H. D., A. B. Slatkin, J. W. Burdick, and Warren S. Grundfest. 2000. “Biomechanical Modeling of the Small Intestine as Required for the Design and Operation of a Robotic Endoscopic.” *Proceedings - IEEE International Conference on Robotics and Automation 2* (April): 1599–1606. <https://doi.org/10.1109/robot.2000.844825>.
- Holzapfel, Gerhard A. 2000. *Nonlinear Solid Mechanics: A Continuum Approach for Engineering Science*. Chichester: Wiley. <https://doi.org/10.1023/A:1020843529530>.
- Holzapfel, Gerhard A., Thomas C. Gasser, and Ray W. Ogden. 2000. “A New Constitutive Framework for Arterial Wall Mechanics and a Comparative Study of Material Models.” *Journal of Elasticity* 61 (1–3): 1–48. <https://doi.org/10.1023/A:1010835316564>.
- Humphrey, J. D., and F. C. P. Yin. 1987. “On Constitutive Relations and Finite Deformations of Passive Cardiac Tissue: I. A Pseudostrain-Energy Function.” *Journal of Biomechanical Engineering* 109 (4): 298–304. <https://doi.org/10.1115/1.3138684>.
- Kim, Nam Ho. 2015. *Introduction to Nonlinear Finite Element Analysis. Introduction to Nonlinear Finite Element Analysis*. New York: Springer. <https://doi.org/10.1007/978-1-4419-1746-1>.
- Koeppen, Bruce, and Bruce Stanton. 2018. *Berne & Levy Physiology*. 7th ed. Elsevier.
- Korelc, Jože, and Peter Wriggers. 2016. *Automation of Finite Element Methods*. 1st ed. Switzerland: Springer. <https://doi.org/10.1007/978-3-319-39005-5>.
- Kottogoda, S. R. 1969. “An Analysis of Possible Nervous Mechanisms Involved in the Peristaltic Reflex.” *The Journal of Physiology* 200 (3): 687–712. <https://doi.org/10.1113/jphysiol.1969.sp008717>.
- Kroon, Martin. 2009. “A Constitutive Model for Smooth Muscle Including Active Tone and Passive Viscoelastic Behaviour.” *Mathematical Medicine and Biology* 27 (2): 129–55. <https://doi.org/10.1093/imammb/dqp017>.
- Lai, W. Michael, David Rubin, and Erhard Kreml. 1996. *Introduction to Continuum Mechanics*. 3rd ed. Butterworth-Heinemann.
- Laine, Loren, Huiying Yang, Shih-Chen Chang, and Catherine Datto. 2012. “Trends for Incidence of

- Hospitalization and Death Due to GI Complications in the United States From 2001 to 2009.” *Official Journal of the American College of Gastroenterology | ACG* 107 (8). https://journals.lww.com/ajg/Fulltext/2012/08000/Trends_for_Incidence_of_Hospitalization_and_Death.12.aspx.
- Lentle, R. G., Patrick W. M. Janssen, Patchana Asvarujanon, Paul Chambers, Kevin J. Stafford, and Yacine Hemar. 2007. “High Definition Mapping of Circular and Longitudinal Motility in the Terminal Ileum of the Brushtail Possum *Trichosurus Vulpecula* with Watery and Viscous Perfusates.” *Journal of Comparative Physiology B: Biochemical, Systemic, and Environmental Physiology* 177 (5): 543–56. <https://doi.org/10.1007/s00360-007-0153-8>.
- Lentle, R. G., and C. de Loubens. 2015. “A Review of Mixing and Propulsion of Chyme in the Small Intestine: Fresh Insights from New Methods.” *Journal of Comparative Physiology B: Biochemical, Systemic, and Environmental Physiology* 185 (4): 369–87. <https://doi.org/10.1007/s00360-015-0889-5>.
- Malfertheiner, Peter, Francis K. L. Chan, and Kenneth E. L. McColl. 2009. “Peptic Ulcer Disease.” *The Lancet* 374 (9699): 1449–61. [https://doi.org/10.1016/S0140-6736\(09\)60938-7](https://doi.org/10.1016/S0140-6736(09)60938-7).
- Martins, J. A. C., M. P. M. Pato, and E. B. Pires. 2006. “A Finite Element Model of Skeletal Muscles.” *Virtual and Physical Prototyping* 1 (3): 159–70. <https://doi.org/10.1080/17452750601040626>.
- Martins, J. A. C., E. B. Pires, R. Salvado, and P. B. Dinis. 1998. “A Numerical Model of Passive and Active Behavior of Skeletal Muscles.” *Computer Methods in Applied Mechanics and Engineering* 151 (3–4): 419–33. [https://doi.org/10.1016/S0045-7825\(97\)00162-X](https://doi.org/10.1016/S0045-7825(97)00162-X).
- Masri, Salah Al, Hana Hünigen, Ahmad Al Aiyan, Juliane Rieger, Jürgen Zentek, Ken Richardson, and Johanna Plendl. 2015. “Influence of Age at Weaning and Feeding Regimes on the Postnatal Morphology of the Porcine Small Intestine.” *Journal of Swine Health and Production* 23 (4): 186–203.
- McFarlane, Isabel M., Manjeet S. Bhamra, Alexandra Kreps, Sadat Iqbal, Firas Al-Ani, Carla Saladini-Aponte, Christon Grant, et al. 2018. “Gastrointestinal Manifestations of Systemic Sclerosis.” <https://doi.org/10.4172/2161-1149.1000235>.
- Monteiro, Carina, Cláudia Miranda, Filipa Brito, Cecília Fonseca, and André R. T. S. Araujo. 2017. “Consumption Patterns of NSAIDs in Central Portugal and the Role of Pharmacy Professionals in Promoting Their Rational Use.” *Drugs and Therapy Perspectives* 33 (1): 32–40. <https://doi.org/10.1007/s40267-016-0352-z>.
- Nylund, K., T. Hausken, S. Ødegaard, G. E. Eide, and O. H. Gilja. 2012. “Gastrointestinal Wall Thickness Measured with Transabdominal Ultrasonography and Its Relationship to Demographic Factors in Healthy Subjects TT - Die Wanddicke des Magen-Darm-Traktes und seine Beziehung zu demografischen Faktoren bei gesunden Probanden,.” *Ultraschall Med* 33 (07): E225–32.
- Oliver, Javier, and C. Agelet de Saracibar. 2017. *Continuum Mechanics for Engineers: Theory and Problems*. 2nd ed. agelet.rmee.upc.edu/books/CM-english.pdf.

- Parente, M. P. L., R. M. Natal Jorge, T. Mascarenhas, A. A. Fernandes, and J. A. C. Martins. 2009. "The Influence of the Material Properties on the Biomechanical Behavior of the Pelvic Floor Muscles during Vaginal Delivery." *Journal of Biomechanics* 42 (9): 1301–6. <https://doi.org/10.1016/j.jbiomech.2009.03.011>.
- Pedersen, Jan, Chunwen Gao, Henrik Egekvist, Peter Bjerring, Lars Arendt-Nielsen, Hans Gregersen, and Asbjørn Mohr Drewes. 2003. "Pain and Biomechanical Responses to Distention of the Duodenum in Patients with Systemic Sclerosis." *Gastroenterology* 124 (5): 1230–39. [https://doi.org/10.1016/S0016-5085\(03\)00265-8](https://doi.org/10.1016/S0016-5085(03)00265-8).
- Reddy, J. N. 2006. *An Introduction to the Finite-Element Method*. 3rd ed. McGraw-Hill Education. <https://doi.org/10.1002/0471777447.ch16>.
- Schulze-Delrieu, Konrad. 1999. "Visual Parameters Define the Phase and the Load of Contractions in Isolated Guinea Pig Ileum." *American Journal of Physiology - Gastrointestinal and Liver Physiology* 276 (6 39-6): 1417–24. <https://doi.org/10.1152/ajpgi.1999.276.6.g1417>.
- Seeley, Rod R., Philip Tate, and Trent D. Stephens. 2007. "Aparelho Digestivo." In *Anatomia & Fisiologia*, 8th ed. Lusociência.
- Shreiner, Andrew B., Charles Murray, Christopher Denton, and Dinesh Khanna. 2016. "Gastrointestinal Manifestations of Systemic Sclerosis." *Journal of Scleroderma and Related Disorders* 1 (3): 247–56. <https://doi.org/10.5301/jsrd.5000214>.
- Sinnott, Matthew D., Paul W. Cleary, and Simon M. Harrison. 2017. "Peristaltic Transport of a Particulate Suspension in the Small Intestine." *Applied Mathematical Modelling* 44: 143–59. <https://doi.org/10.1016/j.apm.2017.01.034>.
- Smith, Michael. 2009. *ABAQUS/Standard User's Manual, Version 6.9*. Dassault Systèmes Simulia Corp.
- Sokolis, Dimitrios P. 2017. "Experimental Study and Biomechanical Characterization for the Passive Small Intestine: Identification of Regional Differences." *Journal of the Mechanical Behavior of Biomedical Materials* 74: 93–105. <https://doi.org/10.1016/j.jmbbm.2017.05.026>.
- Sperber, Ami D., Shrikant I. Bangdiwala, Douglas A. Drossman, Uday C. Ghoshal, Magnus Simren, Jan Tack, William E. Whitehead, et al. 2021. "Worldwide Prevalence and Burden of Functional Gastrointestinal Disorders, Results of Rome Foundation Global Study." *Gastroenterology* 160 (1): 99-114.e3. <https://doi.org/10.1053/j.gastro.2020.04.014>.
- Stein, Erwin, and Gautam Sagar. 2008. "Convergence Behavior of 3D Finite Elements for Neo-Hookean Material." *Engineering Computations: Int J for Computer-Aided Engineering* 25: 220–32. <https://doi.org/10.1108/02644400810857065>.
- Sung, J. J.Y., E. J. Kuipers, and H. B. El-Serag. 2009. "Systematic Review: The Global Incidence and Prevalence of Peptic Ulcer Disease." *Alimentary Pharmacology and Therapeutics* 29 (9): 938–46. <https://doi.org/10.1111/j.1365-2036.2009.03960.x>.
- Tobergte, David R., and Shirley Curtis. 2013. *The Physical Process of Digestion*. *Journal of Chemical*

Information and Modeling. Vol. 53.

- Wang, Andrew Y., and David A. Peura. 2011. "The Prevalence and Incidence of Helicobacter Pylori-Associated Peptic Ulcer Disease and Upper Gastrointestinal Bleeding Throughout the World." *Gastrointestinal Endoscopy Clinics of North America* 21 (4): 613–35. <https://doi.org/10.1016/j.giec.2011.07.011>.
- Wood, J. D. 2004a. "Peristalsis." In *Encyclopedia of Gastroenterology*, edited by L. R. Johnson, 164–65. Elsevier.
- Wood, J. D. 2004b. "Postprandial Motility." In *Encyclopedia of Gastroenterology*, 222–23.
- Wood, J. D. 2004c. "Small Intestinal Motility." In *Encyclopedia of Gastroenterology*, 397–98. Elsevier. <https://doi.org/10.1016/B0-12-386860-2/00653-5>.
- Wood, J. D., and W. E. Perkins. 1970. "Mechanical Interaction between Longitudinal and Circular Axes of the Small Intestine." *American Journal of Physiology-Legacy Content* 218 (3): 762–68. <https://doi.org/10.1152/ajplegacy.1970.218.3.762>.
- Yoshida, H., Y. Morita, and K. Ikeuchi. 2003. "Biological Lubrication of Hydrated Surface Layer in Small Intestine." *Tribology Series* 41 (mm): 425–28. [https://doi.org/10.1016/s0167-8922\(03\)80156-6](https://doi.org/10.1016/s0167-8922(03)80156-6).

APPENDIX A

DEFINITION OF THE ELASTICITY TENSOR FOR THE MARTINS MODEL

The material elasticity tensor \mathbb{C} is given by:

$$\mathbb{C} = \frac{\partial}{\partial \mathbf{E}} \left[\frac{\partial \Psi_{\text{vol}}}{\partial J} \frac{\partial J}{\partial \mathbf{E}} + \frac{\partial \Psi_{\text{mat}}}{\partial \bar{I}_1} \frac{\partial \bar{I}_1}{\partial \mathbf{E}} + \frac{\partial \Psi_{\text{fib}}}{\partial \bar{\lambda}_f} \frac{\partial \bar{\lambda}_f}{\partial \mathbf{E}} \right] \quad (\text{A.1})$$

The detailed development of each of the components of the Equation (A.1) is presented in the Equations (A.2), (A.3) and (A.4).

$$\frac{\partial}{\partial \mathbf{E}} \left[\frac{\partial \Psi_{\text{vol}}}{\partial J} \frac{\partial J}{\partial \mathbf{E}} \right] = J \left(\frac{\partial \Psi_{\text{vol}}}{\partial J} + J \frac{\partial^2 \Psi_{\text{vol}}}{\partial J^2} \right) (\mathbf{C}^{-1} \otimes \mathbf{C}^{-1}) + J \frac{\partial \Psi_{\text{vol}}}{\partial J} \frac{\partial \mathbf{C}^{-1}}{\partial \mathbf{E}} \quad (\text{A.2})$$

$$\begin{aligned} \frac{\partial}{\partial \mathbf{E}} \left[\frac{\partial \Psi_{\text{mat}}}{\partial \bar{I}_1} \frac{\partial \bar{I}_1}{\partial \mathbf{E}} \right] &= \frac{\partial^2 \Psi_{\text{mat}}}{\partial \bar{I}_1^2} \left[4J^{-\frac{4}{3}} \mathbf{I} \otimes \mathbf{I} - \frac{4}{3} J^{-\frac{2}{3}} \bar{I}_1 (\mathbf{I} \otimes \mathbf{C}^{-1} + \mathbf{C}^{-1} \otimes \mathbf{I}) + \frac{4}{9} \bar{I}_1^2 \mathbf{C}^{-1} \otimes \mathbf{C}^{-1} \right] \\ &\quad - \frac{\partial \Psi_{\text{mat}}}{\partial \bar{I}_1} \left[4J^{-\frac{2}{3}} (\mathbf{I} \otimes \mathbf{C}^{-1} + \mathbf{C}^{-1} \otimes \mathbf{I}) + \frac{2}{3} \bar{I}_1 \frac{\partial \mathbf{C}^{-1}}{\partial \mathbf{E}} - \frac{4}{9} \bar{I}_1 \mathbf{C}^{-1} \otimes \mathbf{C}^{-1} \right] \end{aligned} \quad (\text{A.3})$$

$$\begin{aligned} \frac{\partial}{\partial \mathbf{E}} \left[\frac{\partial \Psi_{\text{fib}}}{\partial \bar{\lambda}_f} \frac{\partial \bar{\lambda}_f}{\partial \mathbf{E}} \right] &= \frac{\partial^2 \Psi_{\text{fib}}}{\partial \bar{\lambda}_f^2} \left[J^{-\frac{4}{3}} \frac{1}{\bar{\lambda}_f^2} \underline{\mathbf{N}} \otimes \underline{\mathbf{N}} \otimes \underline{\mathbf{N}} \otimes \underline{\mathbf{N}} \right. \\ &\quad \left. - \frac{1}{3} J^{-\frac{2}{3}} (\underline{\mathbf{N}} \otimes \underline{\mathbf{N}} \otimes \mathbf{C}^{-1} + \mathbf{C}^{-1} \otimes \underline{\mathbf{N}} \otimes \underline{\mathbf{N}}) + \frac{1}{9} \bar{\lambda}_f^2 \mathbf{C}^{-1} \otimes \mathbf{C}^{-1} \right] \\ &\quad - \frac{\partial \Psi_{\text{fib}}}{\partial \bar{\lambda}_f} \left[J^{-\frac{4}{3}} \frac{1}{\bar{\lambda}_f^3} \underline{\mathbf{N}} \otimes \underline{\mathbf{N}} \otimes \underline{\mathbf{N}} \otimes \underline{\mathbf{N}} \right. \\ &\quad \left. + \frac{1}{3} J^{-\frac{2}{3}} \frac{1}{\bar{\lambda}_f} (\underline{\mathbf{N}} \otimes \underline{\mathbf{N}} \otimes \mathbf{C}^{-1} + \mathbf{C}^{-1} \otimes \underline{\mathbf{N}} \otimes \underline{\mathbf{N}}) - \frac{1}{9} \bar{\lambda}_f \mathbf{C}^{-1} \otimes \mathbf{C}^{-1} \right. \\ &\quad \left. + \frac{1}{3} \bar{\lambda}_f \frac{\partial \mathbf{C}^{-1}}{\partial \mathbf{E}} \right] \end{aligned} \quad (\text{A.4})$$

The second derivatives of J , \bar{I}_1 and $\bar{\lambda}_f$ to \mathbf{E} are obtained in the Equations (A.5), (A.6) and (A.7).

$$\frac{\partial^2 \Psi_{\text{vol}}}{\partial J^2} = \frac{2}{D_1} \quad (\text{A.5})$$

$$\frac{\partial^2 \Psi_{\text{mat}}}{\partial \bar{I}_1^2} = b^2 c \left[e^{b(\bar{I}_1 - 3)} \right] \quad (\text{A.6})$$

$$\frac{\partial^2 \Psi_{\text{fib}}}{\partial \bar{\lambda}_f^2} = 2aA \left[e^{a(\bar{\lambda}_f - 1)^2} \right] \left[1 + 2a(\bar{\lambda}_f - 1)^2 \right] + T_0^M f'_{\text{SE}}(\bar{\lambda}_f, \alpha) \quad (\text{A.7})$$

Finally, the derivative $f'_{\text{SE}}(\bar{\lambda}_f, \alpha)$ can be defined by (Martins et al. 1998):

$$f'_{\text{SE}}(\bar{\lambda}_f, \alpha) = \alpha \begin{cases} -8(\bar{\lambda}_f - 1) & \text{for } 0.5 < \bar{\lambda}_f < 1.5 \\ 0 & \text{otherwise} \end{cases} \quad (\text{A.8})$$